Composition and Interface Engineering of Efficient and Stable Perovskite Solar Cells

高効率かつ安定なペロブスカイト太陽電池の組成制御及び界面エンジニアリング

Graduate School of Life Science

and System Engineering

Kyushu Institute of Technology

Dissertation for the Degree of Doctor of Philosophy

Author: GUO ZHANGLIN

Supervisor: Professor Ma Tingli

Aug. 2019

Abstract

Perovskite solar cells (PSCs) is a hot research topic in recent years due to its high-speed development in device performance. However, the power conversion efficiency (PCE) is still lower than the theoretical limitation, and the stability is not satisfactory. These two issues are crucial for the commercialization of this photovoltaic technology. This thesis is mainly focusing on composition and interface engineering for achieving efficient and stable PSCs. Firstly, for improving the device performance, $Ti_3C_2T_x$, a kind of MXene, was introduced into the $CH_3NH_3PbI_3$ perovskite film. The interaction between the additive and the perovskite precursor retards the perovskite crystal growth and results in larger crystals. The high conductivity of the $Ti_3C_2T_x$ accelerates the charge transfer through the perovskite grain boundaries. The larger crystals and the better charge transfer process lead to a higher performance of the PSCs. Secondly, a simple surface passivation method using $SnCl_2$ solution for SnO_2 electron selective layer (ESL) was developed. This method can effectively reduce the charge recombination at the interface of all-inorganic $CsPbIBr_2$ PSCs. The suppressed interfacial recombination leads to improved open-circuit voltage (V_{oc}) and enhanced device performance. Thirdly, for improving the stability of the photoactive phase of all-inorganic $CsPbI_2Br$, Nb^{5+} ions were incorporated into the perovskite materials. The Nb^{5+} doping not only stabilizes the perovskite materials but also reduces the charge recombination in the perovskite film, which enhances the device performance and results in hysteresis-free properties.

In Chapter 1, the background of photovoltaic technologies and the current development, composition modification, device structure and film preparation methods of PSCs were introduced. Moreover, the challenges of the research in PSCs and the purposes of this thesis were presented.

In Chapter 2, the reagents and apparatus for the PSCs fabrication were listed. The basic principle of the characterization techniques, such as XRD, SEM, UV-vis, PL, TRPL, and EIS, and the related instruments were introduced. Furthermore, the method of photovoltaic performance measurements for the PSCs were depicted.

In Chapter 3, for enhancing the efficiency of the solar cells, the high conductivity two-dimensional $Ti_3C_2T_x$ MXene was incorporated into the perovskite absorber layer. Results showed that the termination groups of the $Ti_3C_2T_x$ can retard the nucleation rate of the perovskite, thereby increasing the crystal size of $CH_3NH_3PbI_3$. The high electrical conductivity and mobility of MXene

can accelerate the charge transfer through the perovskite grain boundaries. After optimizing the key parameters including $Ti_3C_2T_x$ adding amount and the solvents for $Ti_3C_2T_x$, the champion PCE of the device was improved from 15.54% to 17.41% and the average PCE was increased from 15.18% to 16.80% with 0.03 wt% amount of $Ti_3C_2T_x$ additive.

In Chapter 4, for reducing the energy loss at the interface, a surface passivation process for SnO_2 ESL employing $SnCl_2$ solution was introduced. This passivation process successfully reduced the energy loss for high V_{oc} output and consequently improved the performance of the all-inorganic $CsPbIBr_2$ PSCs. With the surface passivation, the PCE was enhanced from 4.73% to 7.00% and a high V_{oc} of 1.31 V was achieved, which is one of the highest V_{oc} reported for the inorganic Cs-based PSCs. The main reason is that the surface passivation caused higher recombination resistance, resulting in suppressed recombination process at the interface between the perovskite and the SnO_2.

In Chapter 5, with the aim of stabilizing the photoactive phase of all-inorganic perovskite in ambient conditions, we incorporated the niobium (Nb^{5+}) ions into the $CsPbI_2Br$ perovskite. Results indicate that Nb^{5+} incorporation effectively stabilized the photoactive α-$CsPbI_2Br$ phase by slight substitution of Pb^{2+}. With carbon electrode, the all-inorganic perovskite solar cells achieved a record-high PCE of 10.42% with 0.5% Nb doping, 15% higher than that of the control device. The Nb^{5+} incorporation reduces the charge recombination in the perovskite, leading to a champion V_{oc} of 1.27 V and negligible hysteresis effect.

Finally, the general conclusions of this thesis were summarized and future prospects were proposed. The main issues for the PSCs still lie in the performance and stability. Some strategies such as controlling the perovskite film growth for generating large crystals, optimizing the interface for reducing the recombination and energy loss might be helpful to further improve the device performance. As for the phase stability of all-inorganic PSCs, the effective methods can be constructing a protection layer to prevent the humidity and metal doping to improve the tolerance factor of the structure. The PSCs are very promising for commercialization or using as part of tandem solar cells in practical application.

Contents

Chapter 1 Introduction 1
1.1 Development of photovoltaic technology 1
1.1.1 History and classification of solar cells 1
1.1.2 Working mechanism of solar cells 2
1.2 Halide perovskite materials 3
1.3 Perovskite composition modification 5
1.3.1 A-site cation modification 5
1.3.2 B-site cation modification 6
1.3.3 X-site anion modification 7
1.4 Perovskite solar cells device structure 8
1.5 Perovskite film preparation method 10
1.5.1 One-step preparation method 10
1.5.2 Two-step preparation method 11
1.6 Challenges and Research topics 13
References 15
Chapter 2. Experimental section of the general methods and characterization techniques 22
2.1 Reagents and apparatus 22
2.1.1 Reagents 22
2.1.2 Apparatus 23
2.2 Characterization methods 25
2.2.1 X-ray diffraction crystallography (XRD) 25
2.2.2 Field emission scanning electron microscopy (FE-SEM) 25
2.2.3 Ultraviolet-visible spectroscopy (UV-Vis) 26
2.2.4 Photoluminescence (PL) and Time-Resolved Photoluminescence (TRPL) 26
2.2.5 Electrochemical impedance spectrum (EIS) 27
2.2.6 Photovoltaic performance measurement 27
References 28
Chapter 3. Enhancing the performance by MXene additive 29
3.1 Introduction 29
3.2 Experimental Section 30

3.2.1 Preparation of $Ti_3C_2T_x$ 30
3.2.2 Precursor Preparation and Device Fabrication 31
3.2.3 Characterizations 31
3.3 Results and Discussion 31
3.4 Conclusions 46
References 46
Chapter 4. Reducing the energy loss by interface passivation 52
4.1 Introduction 52
4.2 Experimental Section 53
4.2.1 Device Fabrication 53
4.2.2 Characterizations 54
4.3 Results and discussion 54
4.4 Conclusions 67
References 67
Chapter 5. Improving phase stability by metal doping 72
5.1 Introduction 72
5.2 Experimental Section 73
5.2.1 Device Fabrication 73
5.2.2 DFT Calculations 74
5.2.3 Characterizations 74
5.3 Results and discussion 74
5.4 Conclusions 90
References 90
6. General conclusions and future prospects 96
Achievements 99
Acknowledgements 102

Chapter 1 Introduction

1.1 Development of photovoltaic technology

1.1.1 History and classification of solar cells

Energy is a marking of the origin of human civilization and has always been an important driving force for human progress. With the development of human society, energy is also constantly being developed and utilized. At the end of the 19th century, the use of coal greatly promoted the development of the industrial economy and promoted the pace of social modernization of human beings. At the 1960s, the extraction of oil and gas gradually replaced the coal and finally acted as the main energy type, which brought us to the age of oil. However, the fixed reserves of the fossil energies, including coal, oil and gas and the environment pollution coming with using these energies aroused the attention of the society. It is significantly imperative to exploit recyclable and environment-friendly new energies. Hence, the new energies including water energy, wind energy, solar energy, biology energy, geothermal energy, tidal energy are being developed and commercialized. Among these types, the solar energy is inexhaustible and the total energy amount from the sun to the surface of the earth is equivalent to that of 130 trillion coal burning. More importantly, solar energy environment-friendly and convenient to get, which is very significant to the sustainable development of human society. Therefore, solar energy is very promising energy for us and developing highly efficient solar cells with low cost is a hot topic in energy research area.

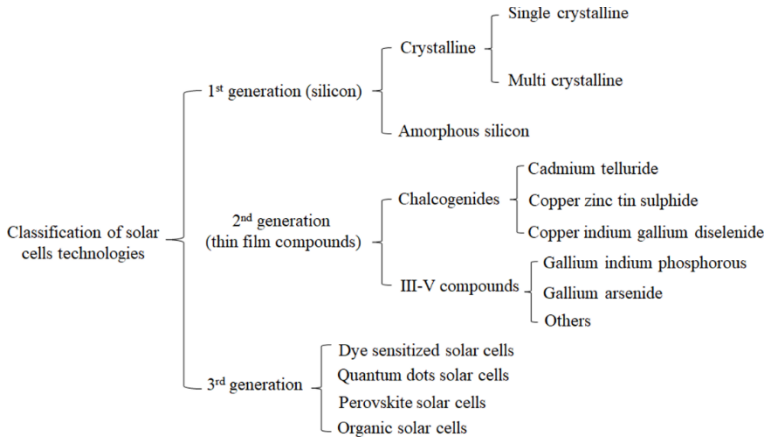

Figure 1 Classification of solar cell technologies by generations.

The solar cells are based on the photovoltaic effect of semiconductors, which can convert the solar light energy to electric energy. According to the light absorption materials, the solar cells can be divided into three generations, as shown in Figure 1:

(1) The first-generation is the silicon solar cells, which are mainly based on the monocrystalline silicon, polysilicon and their composites solar cells.[1] The silicon solar cells, with high photoelectric conversion efficiency (PCE), have been commercialized in human life for many years. After the optimization of the fabrication technologies, the record PCE in the laboratory has been improved to higher than 25% and the cost is also greatly reduced.[2]

(2) The second-generation are the multi-component thin film solar cells, including GaAs,[3] InP,[4] copper indium gallium selenide (CIGS),[5] CdTe solar cells.[6] These solar cells have high PCEs and high device stabilities, at the same time thin absorber layer, which can reduce the raw materials cost-effectively. While the solar cells contain rare elements or the toxic elements, which partly restricts their mass production.

(3) The newly third-generation are the dye-sensitized solar cells,[7] organic solar cells,[8] quantum dots solar cells[9] and PSCs.[10] This newly developed solar cell are still in their infancy stage and most research is in the lab exploration, thus, there is a long way to go for the practical application. The PSC is firstly reported in 2009 and are attracting tremendous attention worldwide, with the PCE dramatically increased from 3.8% to over 23% in several years, which is amazing-fast among the developments of solar cells.[11] Together with their advantages of the simple fabrication process and low cost, the PSCs are expected to be a game changer in the near future of solar cells.

1.1.2 Working mechanism of solar cells

The typical structure of solar cells is a silicon based p-n junction. Specifically, the solar cells are constructed of an n-type silicon contact with a p-type silicon, forming a p-n junction solar cells.[12] When a photon hits the silicon, there are three possible situations: one is that the low energy photons will pass through the silicon; second is that the photons reflect off the surface of the silicon; the third situation is that the photons are absorbed by the silicon. The last situation happens when the photon energy is higher than the silicon band gap and its energy will give to an electron in the silicon lattice. Then the electron is excited by the photon to move from the valence band to the conduction band. A network of covalent bonds to which electrons are already bound. When a

missing covalent bond is present, the bonding electrons of adjacent atoms move into holes, leaving other holes behind, thereby propagating holes throughout the lattice. Thus, photons absorbed by the semiconductor produce electron-hole pairs. Then the generated electron-hole peers separate under two forces. One is the drift of the electric field, which pushes electrons in one direction. Another is carrier spread in the region of higher carrier concentration into the region of lower carrier concentration.[12]

1.2 Halide perovskite materials

The history of the applications of perovskite materials in photovoltaics can be traced to 1956 when the photocurrent was first detected in the $BaTiO_3$ perovskite material.[13] Then the photoelectric effect was also found in some other perovskites such as $LiNbO_3$.[14] The photovoltaics is related to the built-in electric field on the crystal surface formed by the space charge, meaning ferroelectricity. But these perovskite oxides possessed low efficiency below 1%.

In 1978, methylamine cation ($CH_3NH_3^+$, MA^+) was firstly introduced into the perovskite crystals by Weber, forming three-dimensional organic-inorganic perovskite materials.[15] In the typical ABX_3 organic-inorganic perovskite materials, the A site is commonly the organic amine ions (MA, formamidinium ($HC(NH_2)_2^+$, FA^+)), existing at the corners of a cubic unit cell. The B site is the metal ions (Pb^{2+}, Sn^{2+}, etc.), at the body-centered position of the cell. The X represents the halide ions such as I^-, Br^-, Cl^-, or the mixing of them and they occupy the face centers of the cell. Due to their proper ion sizes, the eight BX_6 octahedrons form cubooctahedral voids, with which the A site ions can match well and the nearly cubic crystallographic form can be obtained. Different from the conventional hybrid materials, this kind of material is the composite in the molecular scale and still keep the homogeneous property in macroscopic scale, which can combine the advantages of organic and inorganic material perfectly.

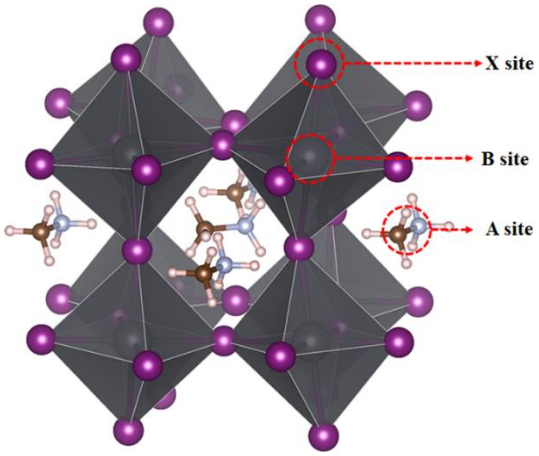

Figure 2 Crystal structure of $MAPbI_3$ organic-inorganic halide perovskite.

The most widely studied organic-inorganic halide perovskite is $MAPbI_3$ material with the band gap of which is 1.5 eV. It can absorb the light with the wavelength smaller than 800 nm, a whole range of visible light spectra. Moreover, the series of perovskite materials have very high light absorption coefficient, thus very suitable for the light absorption. The organic group in the materials makes the precursors have a solubility in organic solvents for film preparation. At the same time, the properties of the perovskite materials can be easily modified via changing the size or the composition of the organic groups.[16] Therefore, the organic-inorganic perovskite materials are very suitable for use as light absorption materials in photovoltaics. Under the effect ofthe electric field, temperature and stress, the perovskite crystal structures can transform between the tetragonal, cubic and orthorhombic crystal system.[17] For example, $MAPbI_3$ is tetragonal at the room temperature and will transit to orthorhombic crystal structure at the higher temperature and become cubic structure at the temperature around 100 ºC.

In 2009, the $MAPbI_3$ and $MAPbBr_3$ were firstly used at the sensitizer in the dye-sensitized solar cells (DSSC), achieving a PCE of around 4%.[10] Then this kind of materials are prepared into quantum dots and applied for DSSC with a higher PCE of 6%.[18] While the perovskite in the liquid DSSC is easily solute in the electrolyte, which resulting short lifetime of the solar cells.

In 2012, the perovskite solar cells based on the light absorber of $MAPbI_3$ and $MAPbI_{3-x}Cl_x$ achieved high PCE of 9.7% and 10.9%,[19] respectively, which aroused wide readership of researchers and was regarded as the milestone of research in PSCs. Only after one year, the PCE

of PSCs had reached to over 15%. Now the record high PCE has been promoted to over 23% after only seven years from the first report of solid state PSC.

1.3 Perovskite composition modification

The perovskite materials are acting as the light absorber in the solar cells, therefore, their optical-electrical characteristics are crucial for the performances of the device. The low band gap with the absorption range from visible to the near-infrared region is necessary for the high current and the high performance of the solar cells. While too low band gap will also result in small voltage values. As a result, a proper band gap (around 1.4 eV) is very important for the perovskite light absorbers. In the perovskite materials, the band gap of the materials can be modified by changing the elements or the compositions.

1.3.1 A-site cation modification

In the Organic-inorganic PSCs, the A site is the organic ions, B site is the metal ions and the X is the halide ions. The A site organic ions are mainly playing the role of charge compensation and have a very small impact on the band structure of the perovskite materials. While the size of A site ions will lead the expanding or shrinking of the crystal lattice, which will affect the length of metal-halide and therefore exert an effect on the band gap of the materials.

The commonly used A site ions are the methylamine cation (MA^+), formamidine cation (MA^+) and cesium (Cs^+).[20-21] MA^+ is the most widely used A site ion, which will results into perovskite materials $MAPbI_3$ with a proper band gap of 1.55 eV and high light absorption coefficient, promising for excellent absorption in the visible region by a thin film. Moreover, because of the small exciton binding energy of $MAPbI_3$ (2-56 meV), the exciton generated by the light are easily split into electrons and holes.[22] The bipolar charge transition properties of $MAPbI_3$ are very helpful for the efficient charge transporting in the film. All of the above advantages are the intrinsic reasons for the high performance of $MAPbI_3$ solar cells.

While the $MAPbI_3$ materials have some disadvantages, such as thermal stability and humidity stability, which means that it is easy to decompose into PbI_2 and CH_3NH_3I materials. For solving these problems, the FA^+ ions with larger size were used to replace the MA^+ ions to form a perovskite materials of $FAPbI_3$, which has a better thermal stability than that of $MAPbI_3$.[23] The $FAPbI_3$ possesses a band gap of 1.43 eV, almost the same with the ideal band gap of 1.44 eV and

it can broaden the absorption spectra to 850 nm.[24] Then the solar cells with the $FAPbI_3$ light absorber layer have higher J_{sc} than that of $MAPbI_3$ solar cells. But due to the smaller band gap, the V_{oc} of the devices becomes lower, leading comparable performance with that of $MAPbI_3$. Gratzel et al. prepared the mixed A site perovskite of $MA_{0.6}FA_{0.4}PbI_3$,[25] which combined the advantages of two type perovskite materials and promised the high J_{sc} and appreciable V_{oc} and finally improved the PCE of the devices. Snaith et al replaced the organic cations with smaller Cs^+ cation and prepared the all-inorganic $CsPbI_3$ perovskite materials.[26] Due to all-inorganic cations, this kind of materials have amazing high thermal stability. While the bandgap of $CsPbI_3$ is 1.73 eV, which means that it could not wholly absorb the light in the visible region. Therefore its performance is not comparable to those of the PSCs with organic cations, at the same time, the device has severe hysteresis. Up to now, the most promising perovskite light absorber layer is the cesium-containing triple cation perovskites, such as $FA_{0.7}MA_{0.2}Cs_{0.1}Pb(I_{5/6}Br_{1/6})_3$ because they can combine the high performance and high device stability.[20, 27]

1.3.2 B-site cation modification

In the most researches on PSCs, the Pb-contained perovskite materials are widely studied. While the Pb element is toxic and not friendly to the environment, so it is very meaningful to replace the Pb with some toxic-free elements. Actually, various kinds of metal elements have been studied as a substitution of Pb elements, such as Ge, Sn, Cu, Sb, Bi, Cu, Zn, etc,[28] among which the Sn is the most promising and most widely studied.

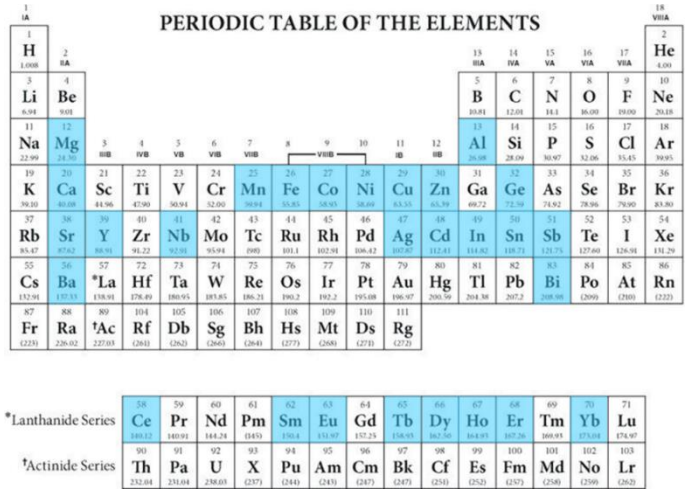

Figure 3 Metal elements (blue marked) used for B site modifications for perovskite materials.

Hayase group firstly reported the substitution of Pb with Sn and prepared the film with 25%, 50% and 75% amount of Sn in the $MAPb_{1-x}Sn_xI_3$ perovskite.[29] The structure of the devices is FTO/c-TiO_2/m-TiO_2/perovskite/P3HT/Au, based on which, the champion PCE of 4.18% was achieved when the Sn amount is 50%. This is because that when the 50% amount of Sn was added into the perovskite, a balance between the series and shunt resistance was achieved. Moreover, the Sn substitution will have an impact on the bond angle between the metal and halide because large bong angle means a lower band gap. Thus partly replace the Pb with Sn will reduce the band gap and broaden the light absorption region to near-infrared. In their research, they found that with 50% Sn, the IPCE absorption edge reached to 1060 nm, which was the main reason for the improved J_{sc} of the device.

Snaith et al. firstly used the Sn for totally replacing the Pb in the perovskite and a higher PCE of 6.4% was achieved with a device configuration of FTO/c-TiO_2/m-TiO_2/perovskite/P3HT/Au.[30] It should be noted that the high V_{oc} of 0.88 V was achieved. The main reasons for the low performance of Sn containing PSCs can be attributed to two aspects. The first one is that the Sn^{2+} ions are easy to be oxidized to Sn^{4+}, forming the self-doping effect, which will generate more amount of p-type charges and restrict the diffusion length of chargers. The second one is because of the quick reaction between the SnI_2 and the MAI, the crystallization process is very difficult to control, resulting in the film with low coverage and non-uniform.

The crystal lattice of Sn contained perovskite is not very stable because the smaller size of Sn than Pb, therefore, the crystal structure stability is a crucial issue. On the other hand, the commonly used Sn^{2+} is very easy to be oxidized to Sn^{4+}, as a result, the device is very sensitive to air. In most research on Sn-based solar cells, the fabrication and testing process is always conducted in the N_2 or Ar glove box. Thus there are more and more research is carrying out on replacing Pb with other kinds of metal ions for achieving highly stable, efficient and environment-friendly PSCs.

1.3.3 X-site anion modification

Increasing the size of X elements can improve the crystal constants of the perovskite materials because the larger ion size can reduce the acting force with Pb ions. In addition, by adjusting the ratio between the I-Br and Cl-Br, the light absorption edge can be continuously modified. The $MAPbI_3$ perovskite has a band gap of 1.55 eV and can absorb the light with the

wavelength smaller than 800 nm. The diffusion length of 100 nm for $MAPbI_3$ can be largely improved to 1 um when Cl^- was introduced to the materials.[31] But the Cl^- has little effect on the absorption ability of the materials, which means that the main role of Cl^- is to control the crystallization process, affect the film morphology and reduce the defects in the film, rather than occupying the I^- sites because Cl^- easily escape the crystal lattice during the heating process.

By adjusting the ratio of halide element in the perovskite, we can get a series of materials with different band gaps.[32] Usually, the band gap increases with increasing the amount of Br^- or Cl^- for replacing I^-, which is not good for the light absorption.[33] On the other hand, increasing the amount of Br^- is helpful to enhance the phase stability of the materials. Recently, the modification of the halide elements in the all-inorganic perovskite has been widely studied. When introducing the Br^- into the $CsPbI_3$, the band gap will be enlarged: 1.73 eV for $CsPbI_3$, 1.92 eV for $CsPbI_2Br$ and 2.05 eV for $CsPbIBr_2$.[33-34] Though the enlarged band gap is not favorable for the light absorption, the phase stability is greatly enhanced. This is because that Br^- replacing I^- will greatly increase the tolerance factor the perovskite materials and partly prevent the room temperature phase transition from photoactive black phase to photo non-active yellow phase.[35] A trade-off should be achieved between the stability and light absorption ability for perovskite materials.

1.4 Perovskite solar cells device structure

The PSCs device contains five parts, as shown in Figure 5, the FTO/glass substrate, ESL, light absorber, hole transporting material (HTM) and Au.[36-37] The ESL is for collecting electrons and blocking holes, while the HTM has the role of transporting holes and blocking electrons from the perovskite. The perovskite light absorber, with the formula of ABX_3 (A=CH_3NH_3 (abbreviated as MA), $HC(NH_2)_2$ (abbreviated as FA), Cs; B=Pb, Sn; X=Cl, Br, I), is the core of the PSCs.[38] The most widely used HTM is the organic p-type semiconductor of 2,2',7,7'-tetrakis[N,N-di(4-methoxyphenyl)amino]-9,9'-spirobifluorene (Spiro-MeOTAD). In addition, some other p-type materials, such as Poly(3-hexylthiophene-2,5-diyl) (P3HT), NiO, CuSCN, and $CuGaO_2$, have also been utilized as efficient HTLs.[39]

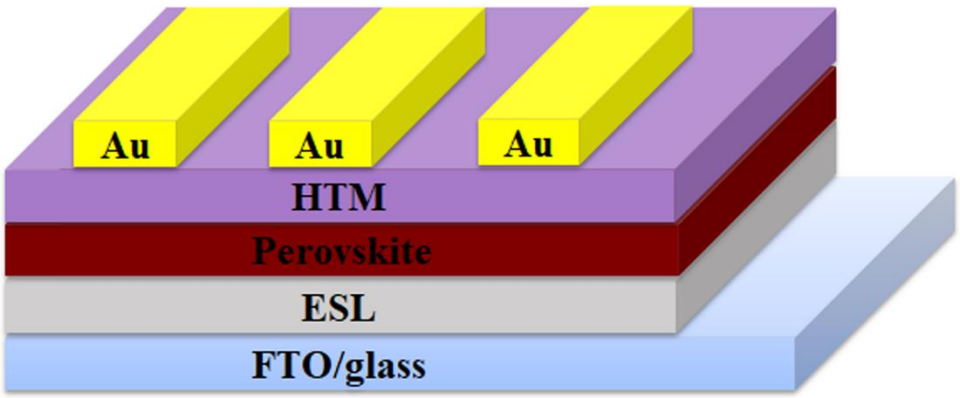

Figure 4 Device structure of perovskite solar cells.

In the structure of the PSCs, the perovskite material can absorb the light and convert the light into carriers.[40] The photogenerated electrons and holes coexist in the perovskite layer due to its unique ambipolar property.[41-42] Then the electrons can be injected into the n-type ESL (with subsequent electron transport to the FTO electrode) and holes can be transferred to the p-type HTM (with subsequent transport to the Au electrode. Additionally, the ESL performs as an electron blocking layer to prevent the holes from the perovskite and HTM from reaching the FTO electrode due to its valance band position is lower than that of the perovskite materials. Meanwhile, the HTM blocks the electrons from the perovskite and ESL due to its higher conduction band position than that of the perovskite materials. Therefore, the effective charge transportation and blocking mechanism can avoid the short circuit in the device. The uniform films including the ESL, the perovskite layer and the HTM, and the optimized interfaces are important to the PSCs performance.

TiO_2 is a typical ESL for the PSCs. Despite the excellent PCEs, high temperature (around 500 ºC) post-treatment of the TiO_2 layer is needed for receiving high film quality.[43] The high temperature hinders the simple and low-cost mass production of PSCs due to the complex and energy intensive annealing step. Moreover, PSCs based on TiO_2 are suffering from UV-light instability due to the high photocatalytic activity of the TiO_2, which can damage the perovskite materials and impede the reproducibility of the devices.[44-45] Another drawback of the TiO_2 is that the electron mobility (1 $cm^2V^{-1}s^{-1}$) is much lower than that of the perovskite layer (24.8 1 $cm^2V^{-1}s^{-1}$), resulting in a mode of unbalanced charge transport.[46] The imperfect alignment between the conduction bands of TiO_2 and the perovskite layer, resulting in hysteresis of the J-V characteristic, might be another disadvantage. Therefore, considerable attention has been devoted to modifying the conventional TiO_2 ESL in order to overcome the aforementioned disadvantages. The general

strategies are preparing low-temperature processable amorphous TiO_x film,[47] constructing TiO_2 composite film with other compounds,[48-49] morphology controlling of the TiO_2 film,[50] and metals doping within the TiO_2 film.[51-53] For instance, Ta-doped TiO_2 ESL based PSCs exhibited a remarkable improvement in PCE, as compared to those with un-doped TiO_2 .[52-53]

Flexible PSCs are fabricated on flexible substrates.[54-57] These flexible PSCs have great potential of being used in wearable electrical devices because they can maintain a high performance even after being bent for thousands of times during use.[55] Meanwhile, these flexible substrates are low-cost and lightweight, benefiting for the commercialization of wearable electronics. However, different from the rigid substrates including glass/FTO and glass/ITO, these flexible substrates are not able to withstand high temperatures. Therefore, low-temperature processable ESLs are urgently required for manufacturing high-performance flexible PSCs, which will promote the industrial printing processes with roll-to-roll technology and reducing the production costs of wearable electronics.

Inspired by the low-temperature fabrication of the perovskite layer and the HTM, it is crucial to develop efficient and low-temperature processable ESLs to reduce the production costs, simplify the process, meet the requirement for flexible PSCs fabrication, and realize the all-low-temperature mass manufacturing of the PSCs. In our experiments, we use the low-temperature SnO_2 as the ESL, which needs only a simple preparation process, low-temperature annealing, and low cost but promises for high performance.

1.5 Perovskite film preparation method

There are several methods for perovskite preparation. The methods can be divided mainly two types: solution process and vapor deposition process. The solution process contains one-step, two-step spin-coating process and immersing process, which has a low request for the devices. While the vapor deposition process is always conducted in the vacuum environment, which has a high demand for the equipment but promises high film quality. Here we mainly introduce the solution processes (one-step and two-step process) that are used in our experiments.

1.5.1 One-step preparation method

The widely used fabrication methods of the PSCs are a one-step method and two-step method, etc., among which the one-step process is the simplest one.[58] In this process, firstly the raw

materials of lead halide and organic halide are dissolved in the organic solvents such as Dimethylformamide (DMF), Dimethyl sulfoxide (DMSO), N-Methyl-2-pyrrolidone (NMP) and gamma-Butyrolactone (GBL) to form the perovskite precursor solution.[59-60] Then the precursor is deposited on the substrate and spun coated for obtaining a thin precursor film. During the heating process, the solvents evaporate and the perovskite crystal film forms. In many types of research, the anti-solvent of chlorobenzene (CB) and ethyl acetate (EA) is used to form a uniform and high-quality film. This is because of the mutual solubility between the solvent and anti-solvent while low solubility of perovskite precursor in the anti-solvent. When the anti-solvent is dripped on the rotating film, it will bring the solvent of the perovskite away and the crystal nuclei will generate due to the low solubility of perovskite in the anti-solvent. The one-step fabrication process is highly affected by the annealing temperature, concentration of the precursor, ratio of raw materials and the type of solvents, which determine the film morphology and quality.[61]

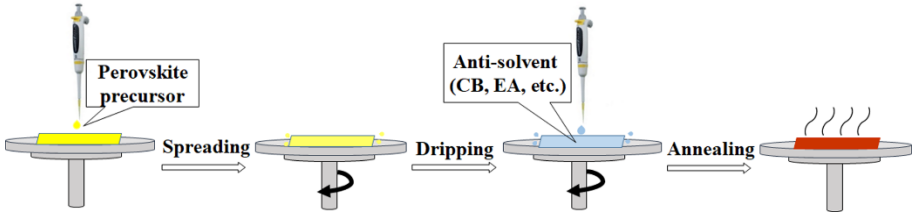

Figure 5 One-step anti-solvent perovskite film preparation process.

1.5.2 Two-step preparation method

The two-step spin-coating process contains two steps: firstly spin-coating the PbI_2 layer and low-temperature heating for solvent evaporation, and the second step is to spin-coating the organic halide MAI.[62] Through the annealing process, the two kinds material will mutual diffuse and react, generating the perovskite phase. It can precisely control the compositions of the perovskite compositions. The PbI_2 is usually dissolved in the DMF solvent by forming the weak coordination within the two molecules. When the MAI is spin-coated on the PbI_2 film, the PbI_2 reacts with the iodide ions to form the PbI_3^- ions. Then the MA^+ replace the DMF solvent to form the intermediate phase.[63-64] During the annealing process, the DMF evaporates and the intermediate phase transforms to the perovskite phase. This method also has some disadvantages. The first one is that this method is easier to form the PbI_2 residuals under the perovskite layer, especially in the planar structural device, because of the incomplete reaction between the MAI and the underlying PbI_2

materials.[65] The second one that this process needs longer time and higher temperature than that for the one-step process because of the relatively slow reaction between the two raw materials.

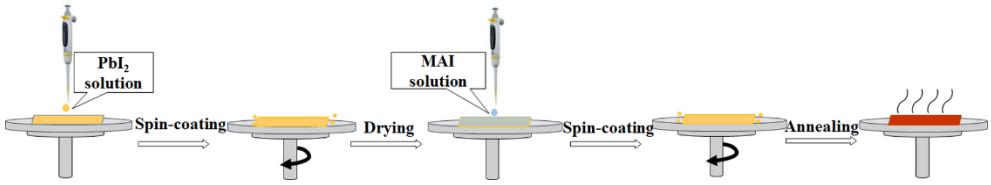

Figure 6 Two-step perovskite film preparation process.

Park group compared the morphologies of the films fabricated by the two-step and one-step spin-coating process using the mesoporous device structure.[58] They found that the one-step process easily results in aggregation and non-uniformity of the crystals, moreover, the film has low coverage on the TiO_2 film. While the two-step can obtain a uniform film with high reproducibility. They also found that changing the concentration of MAI can effectively control the crystal size of the perovskite film.

Similar to the two-step process, the sequential dipping method is also commonly used for film preparation because of its high controllability and reproducibility. The first step is to spin-coat the PbI_2 film on the mesoporous TiO_2 film makes form nanocrystals in the framework of TiO_2. Then immerse the dried PbI_2 film into the MAI solution for one minute, during with the PbI_2 will react with MAI to form the perovskite materials. The excessive MAI can be washed out by IPA solvent.[66] This method can well control the film morphology and the uniformity, which is promising for the high-performance devices. While the biggest negative is that this method is only suitable for the mesoporous device rather than a planar device. Research has proved that in the planar device, the thickness of the prepared film can only reach to 200 nm. When increasing the thickness of PbI_2, it will be difficult for the MAI to diffuse through the PbI_2 and PbI_2 will not wholely react with the MAI, resulting into PbI_2 residue, similar with the two-step method.

Another method is the vapor deposition process, which was firstly proposed by Snaith.[67] In their experiment, they mixing evaporated the $PbCl_2$ and the MAI in the vacuum conditions and obtained a very uniform perovskite film and achieved a high PCE of 15.4%. While this method must be operated in the vacuum conditions and only suitable for the planar devices, which is hardly be used for large-scale device fabrication.

With the development of the fabrication methods, the unsatisfactory morphology of perovskite film obtained by the one-step process has been overcome by precisely controlling the dripping process of anti-solvent and proper annealing optimization. Therefore, together with their advantages including simple operations, the one-step process is becoming widely used in fabricating high-quality perovskite films.

1.6 Challenges and Research topics

The PSC is a very promising photovoltaic technology due to the advantages including simple fabrication process, high efficiency, low-cost, etc. While there are still several challenges lie in the way towards commercialization process. The first one is the further enhancement in PCE. It has been predicted that the limitation in PCE is 30~33 %[68] and the record PCE now is lower than 24%, thus there still a space for the efficiency improvement. The PCE can be further improved in several ways. The essential one is to control the perovskite crystal growth for obtaining large crystals with fewer amount of grain boundaries, where the charge will recombine.[69] Improve the conductivity and charge mobility of the perovskite film can accelerate the charge transformation and enhance the efficiency. The interface modification is also efficient because this is helpful for reducing the charge recombination during transformation through the interface.[70]

The second challenge is energy loss, especially in the all-inorganic PSCs. The energy loss is defined as the difference between the band gap of the light absorber and the eV_{oc}.[71] The energy loss for all-inorganic PSCs is usually large than 0.8 eV, meaning unsatisfied V_{oc}, which will result in not very high performance. There are two resolutions for these problems. The first one is to reduce the trap states in the perovskite layer because these trap states are responsible for the radiative recombination of the photo-generated charges.[71] The other one is to reduce the interface recombination by interface passivation, which will obviously increase the V_{oc} for the device.[72]

The third problem is the phase stability of the photoactive perovskite phase. It is well known that the organic-inorganic hybrid PSCs are very sensitive to the humidity and heat. Researchers try to solve the thermal stability issue by replacing the MA with Cs at the A site of perovskite. While the phase stability of the Cs based perovskite is very poor because it trends to transform to photo non-active phase at room temperature.[73] The strategies such as constructing a protection layer for preventing humidity and metal doping for higher structural stability are promising

solutions for the phase stability of the perovskite materials.[74-75] Inspired by these challenges in the research of PSCs, several works were carried out to trying to solve the issues.

Firstly, for further enhancing device performance, the two-dimensional high-conductivity $Ti_3C_2T_x$ MXene was combined with $CH_3NH_3PbI_3$ perovskite film for the first time. The $Ti_3C_2T_x$ nanosheets were dispersed in different solvents and then were added into the perovskite precursor. By characterizing the resultant film, it was found that this additive retards the nucleation process of the perovskite, resulting in larger grain size because of the interaction between the MXene and the elements in perovskite. Moreover, the additive with high conductivity and mobility is highly beneficial to accelerate the electron transfer through the grain boundary. After optimizing key parameters, we found that 0.03 wt% is the optimal amount and DMF is the most proper solvent for MXene additive. Accordingly, the highest PCE is improved from 15.54% to 17.41% and the average PCE is increased from 15.18% to 16.80%.

Secondly, in order to reduce the energy loss of the all-inorganic PSCs, a simple interface engineering process for SnO_2 ESL surface passivation employing $SnCl_2$ was developed. This interface engineering successfully reduced the energy loss for high V_{oc} output and consequently improved the performance of the all-inorganic $CsPbIBr_2$ PSCs. It was found that the surface passivation can effectively suppress the recombination process at the interface between the perovskite and the SnO_2 due to higher recombination resistance. The shorter PL decay time indicates more efficient electron extraction process from the perovskite film. After optimizing the surface passivation, the PCE was enhanced from 4.73% to 7.00% and a high V_{oc} of 1.31 V was achieved, which is one of the highest V_{oc} reported for the inorganic Cs-based PSCs. More importantly, the passivated SnO_2 based device retains 95.5% of its initial performance at 90 ºC in the air without encapsulation for 80 h.

In the third part, with the aim of stabilizing the photoactive phase of all-inorganic perovskite materials, for the first time, we report the incorporation of niobium (Nb^{5+}) ions into the $CsPbI_2Br$ perovskite. Results indicate that Nb^{5+} incorporation effectively stabilizes the photoactive α-$CsPbI_2Br$ phase by slight substitution of Pb^{2+}. With carbon electrode, the all-inorganic perovskite solar cells achieved a record-high PCE of 10.42% with 0.5% Nb^{5+} doping, 15% higher than that of the control device. The Nb^{5+} incorporation has reduced the charge recombination in the perovskite, leading to a champion Voc of 1.27 V with negligible hysteresis effect.

References

1. Bergmann, R., Crystalline Si thin-film solar cells: a review. *Appl. Phys. A* **1999,** *69* (2), 187-194.

2. Bermel, P.; Luo, C.; Zeng, L.; Kimerling, L. C.; Joannopoulos, J. D., Improving thin-film crystalline silicon solar cell efficiencies with photonic crystals. *Opt. Express* **2007,** *15* (25), 16986-17000.

3. Ohno, H.; Shen, A.; Matsukura, F.; Oiwa, A.; Endo, A.; Katsumoto, S.; Iye, Y., (Ga, Mn) As: a new diluted magnetic semiconductor based on GaAs. *Appl. Phys. Lett.* **1996,** *69* (3), 363-365.

4. Wallentin, J.; Anttu, N.; Asoli, D.; Huffman, M.; Åberg, I.; Magnusson, M. H.; Siefer, G.; Fuss-Kailuweit, P.; Dimroth, F.; Witzigmann, B., InP nanowire array solar cells achieving 13.8% efficiency by exceeding the ray optics limit. *Science* **2013,** *339* (6123), 1057-1060.

5. Jackson, P.; Hariskos, D.; Lotter, E.; Paetel, S.; Wuerz, R.; Menner, R.; Wischmann, W.; Powalla, M., New world record efficiency for Cu (In, Ga) Se_2 thin-film solar cells beyond 20%. *Prog. Photovoltaics* **2011,** *19* (7), 894-897.

6. Britt, J.; Ferekides, C., Thin-film CdS/CdTe solar cell with 15.8% efficiency. *Appl. Phys. Lett.* **1993,** *62* (22), 2851-2852.

7. Hagfeldt, A.; Boschloo, G.; Sun, L.; Kloo, L.; Pettersson, H., Dye-sensitized solar cells. *Chem. Rev.* **2010,** *110* (11), 6595-6663.

8. Wöhrle, D.; Meissner, D., Organic solar cells. *Adv. Mater.* **1991,** *3* (3), 129-138.

9. Nozik, A. J.; Beard, M. C.; Luther, J. M.; Law, M.; Ellingson, R. J.; Johnson, J. C., Semiconductor quantum dots and quantum dot arrays and applications of multiple exciton generation to third-generation photovoltaic solar cells. *Chem. Rev.* **2010,** *110* (11), 6873-6890.

10. Kojima, A.; Teshima, K.; Shirai, Y.; Miyasaka, T., Organometal halide perovskites as visible-light sensitizers for photovoltaic cells. *J. Am. Chem. Soc.* **2009,** *131* (17), 6050-6051.

11. https://www.nrel.gov/pv/assets/pdfs/pv-efficiency-chart.20190103.pdf.

12. https://en.wikipedia.org/wiki/Theory_of_solar_cells.

13. Xiong, B.; Hao, H.; Zhang, S.; Liu, H.; Cao, M., Structure, dielectric properties and temperature stability of $BaTiO_3$-$Bi(Mg_{1/2}Ti_{1/2})O_3$ perovskite solid solutions. *J. Am. Ceram. Soc.* **2011,** *94* (10), 3412-3417.

14. Dunn, S.; Tiwari, D., Influence of ferroelectricity on the photoelectric effect of $LiNbO_3$. *Appl. Phys. Lett.* **2008,** *93* (9), 092905.

15. Noh, J. H.; Im, S. H.; Heo, J. H.; Mandal, T. N.; Seok, S. I., Chemical management for colorful, efficient, and stable inorganic-organic hybrid nanostructured solar cells. *Nano Lett.* **2013,** *13* (4), 1764-1769.

16. Saparov, B.; Mitzi, D. B., Organic-inorganic perovskites: structural versatility for functional materials design. *Chem. Rev.* **2016,** *116* (7), 4558-4596.

17. Quarti, C.; Mosconi, E.; Ball, J. M.; D'Innocenzo, V.; Tao, C.; Pathak, S.; Snaith, H. J.; Petrozza, A.; De Angelis, F., Structural and optical properties of methylammonium lead iodide across the tetragonal to cubic phase transition: implications for perovskite solar cells. *Energy Environ. Sci.* **2016,** *9* (1), 155-163.

18. Kim, H.-S.; Lee, J.-W.; Yantara, N.; Boix, P. P.; Kulkarni, S. A.; Mhaisalkar, S.; Grätzel, M.; Park, N.-G., High efficiency solid-state sensitized solar cell-based on submicrometer rutile TiO_2 nanorod and $CH_3NH_3PbI_3$ perovskite sensitizer. *Nano Lett.* **2013,** *13* (6), 2412-2417.

19. Kim, H.-S.; Lee, C.-R.; Im, J.-H.; Lee, K.-B.; Moehl, T.; Marchioro, A.; Moon, S.-J.; Humphry-Baker, R.; Yum, J.-H.; Moser, J. E., Lead iodide perovskite sensitized all-solid-state submicron thin film mesoscopic solar cell with efficiency exceeding 9%. *Sci. Rep.* **2012,** *2*, 591.

20. Jeon, N. J.; Noh, J. H.; Yang, W. S.; Kim, Y. C.; Ryu, S.; Seo, J.; Seok, S. I., Compositional engineering of perovskite materials for high-performance solar cells. *Nature* **2015,** *517*, 476.

21. Huang, J.; Shao, Y.; Dong, Q., Organometal trihalide perovskite single crystals: a next wave of materials for 25% efficiency photovoltaics and applications beyond? *J. Phys. Chem. Lett.* **2015,** *6* (16), 3218-3227.

22. Leguy, A. M.; Azarhoosh, P.; Alonso, M. I.; Campoy-Quiles, M.; Weber, O. J.; Yao, J.; Bryant, D.; Weller, M. T.; Nelson, J.; Walsh, A., Experimental and theoretical optical properties of methylammonium lead halide perovskites. *Nanoscale* **2016,** *8* (12), 6317-6327.

23. Smecca, E.; Numata, Y.; Deretzis, I.; Pellegrino, G.; Boninelli, S.; Miyasaka, T.; La Magna, A.; Alberti, A., Stability of solution-processed $MAPbI_3$ and $FAPbI_3$ layers. *Phys. Chem. Chem. Phys.* **2016,** *18* (19), 13413-13422.

24. Han, Q.; Bae, S. H.; Sun, P.; Hsieh, Y. T.; Yang, Y.; Rim, Y. S.; Zhao, H.; Chen, Q.; Shi, W.; Li, G., Single crystal formamidinium lead iodide ($FAPbI_3$): insight into the structural, optical, and electrical properties. *Adv. Mater.* **2016,** *28* (11), 2253-2258.

25. Pellet, N.; Gao, P.; Gregori, G.; Yang, T. Y.; Nazeeruddin, M. K.; Maier, J.; Grätzel, M., Mixed - organic - cation Perovskite photovoltaics for enhanced solar - light harvesting. *Angew. Chem.* **2014,** *126* (12), 3215-3221.

26. Eperon, G. E.; Paterno, G. M.; Sutton, R. J.; Zampetti, A.; Haghighirad, A. A.; Cacialli, F.; Snaith, H. J., Inorganic caesium lead iodide perovskite solar cells. *J. Mater. Chem. A* **2015,** *3* (39), 19688-19695.

27. Saliba, M.; Matsui, T.; Seo, J.-Y.; Domanski, K.; Correa-Baena, J.-P.; Nazeeruddin, M. K.; Zakeeruddin, S. M.; Tress, W.; Abate, A.; Hagfeldt, A.; Grätzel, M., Cesium-containing triple cation perovskite solar cells: improved stability, reproducibility and high efficiency. *Energy Environ. Sci.* **2016,** *9* (6), 1989-1997.

28. Zhou, Y.; Chen, J.; Bakr, O. M.; Sun, H.-T., Metal-Doped Lead Halide Perovskites: Synthesis, Properties, and Optoelectronic Applications. *Chem. Mater.* **2018,** *30* (19), 6589-6613.

29. Ogomi, Y.; Morita, A.; Tsukamoto, S.; Saitho, T.; Fujikawa, N.; Shen, Q.; Toyoda, T.; Yoshino, K.; Pandey, S. S.; Ma, T.; Hayase, S., $CH_3NH_3Sn_xPb_{(1-x)}I_3$ Perovskite Solar Cells Covering up to 1060 nm. *J. Phys. Chem. Lett.* **2014,** *5* (6), 1004-1011.

30. Noel, N. K.; Stranks, S. D.; Abate, A.; Wehrenfennig, C.; Guarnera, S.; Haghighirad, A.-A.; Sadhanala, A.; Eperon, G. E.; Pathak, S. K.; Johnston, M. B.; Petrozza, A.; Herz, L. M.; Snaith, H. J., Lead-free organic-inorganic tin halide perovskites for photovoltaic applications. *Energy Environ. Sci.* **2014,** *7* (9), 3061-3068.

31. Zhang, H.; Liao, Q.; Wang, X.; Hu, K.; Yao, J.; Fu, H., Controlled Substitution of Chlorine for Iodine in Single - Crystal Nanofibers of Mixed Perovskite $MAPbI_{3-x}Cl_x$. *Small* **2016,** *12* (28), 3780-3787.

32. Akkerman, Q. A.; D'Innocenzo, V.; Accornero, S.; Scarpellini, A.; Petrozza, A.; Prato, M.; Manna, L., Tuning the Optical Properties of Cesium Lead Halide Perovskite Nanocrystals by Anion Exchange Reactions. *J. Am. Chem. Soc.* **2015,** *137* (32), 10276-10281.

33. Nam, J. K.; Chun, D. H.; Rhee, R. J. K.; Lee, J. H.; Park, J. H., Methodologies toward Efficient and Stable Cesium Lead Halide Perovskite - Based Solar Cells. *Adv. Sci.* **2018**, 1800509.

34. Liu, C.; Li, W.; Zhang, C.; Ma, Y.; Fan, J.; Mai, Y., All-inorganic $CsPbI_2Br$ perovskite solar cells with high efficiency exceeding 13%. *J. Am. Chem. Soc.* **2018,** *140* (11), 3825-3828.

35. Swarnkar, A.; Mir, W. J.; Nag, A., Can B-site doping or alloying improve thermal-and phase-stability of all-inorganic $CsPbX_3$ (X=Cl, Br, I) perovskites? *ACS Energy Lett.* **2018,** *3* (2), 286-289.

36. Jung, H. S.; Park, N. G., Perovskite solar cells: from materials to devices. *Small* **2015,** *11* (1), 10-25.

37. Green, M. A.; Ho-Baillie, A.; Snaith, H. J., The emergence of perovskite solar cells. *Nat. Photonics* **2014,** *8* (7), 506-514.

38. Seo, J.; Noh, J. H.; Seok, S. I., Rational strategies for efficient perovskite solar cells. *Acc. Chem. Res.* **2016,** *49* (3), 562-572.

39. Yu, Z.; Sun, L., Recent Progress on Hole-Transporting Materials for Emerging Organometal Halide Perovskite Solar Cells. *Adv. Energy Mater.* **2015,** *5* (12), 1500213.

40. Lee, M. M.; Teuscher, J.; Miyasaka, T.; Murakami, T. N.; Snaith, H. J., Efficient hybrid solar cells based on meso-superstructured organometal halide perovskites. *Science* **2012,** *338* (6107), 643-647.

41. Tyson, T.; Gao, W.; Chen, Y.-S.; Ghose, S.; Yan, Y., Large Thermal Motion in Halide Perovskites. *Sci. Rep.* **2017,** *7* (1), 9401.

42. Yang, Y.; Yang, M.; Moore, D. T.; Yan, Y.; Miller, E. M.; Zhu, K.; Beard, M. C., Top and bottom surfaces limit carrier lifetime in lead iodide perovskite films. *Nature Energy* **2017,** *2*, 16207.

43. Chen, B.; Zheng, X.; Yang, M.; Zhou, Y.; Kundu, S.; Shi, J.; Zhu, K.; Priya, S., Interface band structure engineering by ferroelectric polarization in perovskite solar cells. *Nano Energy* **2015,** *13*, 582-591.

44. Leijtens, T.; Eperon, G. E.; Pathak, S.; Abate, A.; Lee, M. M.; Snaith, H. J., Overcoming ultraviolet light instability of sensitized TiO2 with meso-superstructured organometal tri-halide perovskite solar cells. *Nat. Commun.* **2013,** *4*, 2885.

45. Guo, Y.; Liu, C.; Tanaka, H.; Nakamura, E., Air-stable and solution-processable perovskite photodetectors for solar-blind UV and visible light. *J. Phys. Chem. Lett.* **2015,** *6* (3), 535-539.

46. Ponseca Jr, C. S.; Savenije, T. J.; Abdellah, M.; Zheng, K.; Yartsev, A.; Pascher, T. r.; Harlang, T.; Chabera, P.; Pullerits, T.; Stepanov, A., Organometal halide perovskite solar cell materials rationalized: ultrafast charge generation, high and microsecond-long balanced mobilities, and slow recombination. *J. Am. Chem. Soc.* **2014,** *136* (14), 5189-5192.

47. Deng, X.; Wilkes, G. C.; Chen, A. Z.; Prasad, N. S.; Gupta, M. C.; Choi, J. J., Room-Temperature Processing of TiO x Electron Transporting Layer for Perovskite Solar Cells. *J. Phys. Chem. Lett.* **2017,** *8* (14), 3206-3210.

48. Wang, J. T.-W.; Ball, J. M.; Barea, E. M.; Abate, A.; Alexander-Webber, J. A.; Huang, J.; Saliba, M.; Mora-Sero, I.; Bisquert, J.; Snaith, H. J., Low-temperature processed electron collection layers of graphene/TiO2 nanocomposites in thin film perovskite solar cells. *Nano Lett.* **2013,** *14* (2), 724-730.

49. Li, H.; Shi, W.; Huang, W.; Yao, E.-P.; Han, J.; Chen, Z.; Liu, S.; Shen, Y.; Wang, M.; Yang, Y., Carbon Quantum Dots/TiO x Electron Transport Layer Boosts Efficiency of Planar Heterojunction Perovskite Solar Cells to 19%. *Nano Lett.* **2017,** *17* (4), 2328-2335.

50. Thakur, U. K.; Askar, A. M.; Kisslinger, R.; Wiltshire, B. D.; Kar, P.; Shankar, K., Halide perovskite solar cells using monocrystalline TiO2 nanorod arrays as electron transport layers: Impact of nanorod morphology. *Nanotechnology* **2017,** *28* (274001), 274001.

51. Yin, G.; Ma, J.; Jiang, H.; Li, J.; Yang, D.; Gao, F.; Zeng, J.; Liu, Z.; Liu, S. F., Enhancing Efficiency and Stability of Perovskite Solar Cells through Nb-Doping of TiO2 at Low Temperature. *ACS Appl. Mater. Interfaces* **2017,** *9* (12), 10752-10758.

52. Cui, Q.; Zhao, X.; Lin, H.; Yang, L.; Chen, H.; Zhang, Y.; Li, X., Improved efficient perovskite solar cells based on Ta-doped TiO 2 nanorod arrays. *Nanoscale* **2017,** *9* (47), 18897-18907.

53. Ranjan, R.; Prakash, A.; Singh, A.; Singh, A.; Garg, A.; Gupta, R. K., Effect of tantalum doping in TiO2 compact layer on the performance of planar Spiro-OMeTAD free perovskite solar cells. *J. Mater. Chem. A* **2017**, 10.1039/C7TA09193A.

54. Yang, D.; Yang, R.; Zhang, J.; Yang, Z.; Liu, S. F.; Li, C., High efficiency flexible perovskite solar cells using superior low temperature TiO 2. *Energy Environ. Sci.* **2015,** *8* (11), 3208-3214.

55. Kim, B. J.; Kim, D. H.; Lee, Y.-Y.; Shin, H.-W.; Han, G. S.; Hong, J. S.; Mahmood, K.; Ahn, T. K.; Joo, Y.-C.; Hong, K. S., Highly efficient and bending durable perovskite solar cells: toward a wearable power source. *Energy Environ. Sci.* **2015,** *8* (3), 916-921.

56. Chiang, Y.-F.; Jeng, J.-Y.; Lee, M.-H.; Peng, S.-R.; Chen, P.; Guo, T.-F.; Wen, T.-C.; Hsu, Y.-J.; Hsu, C.-M., High voltage and efficient bilayer heterojunction solar cells based on an

organic–inorganic hybrid perovskite absorber with a low-cost flexible substrate. *Phys. Chem. Phys. Chem.* **2014,** *16* (13), 6033-6040.

57. Docampo, P.; Ball, J. M.; Darwich, M.; Eperon, G. E.; Snaith, H. J., Efficient organometal trihalide perovskite planar-heterojunction solar cells on flexible polymer substrates. *Nat. Commn.* **2013,** *4*, 2761.

58. Im, J.-H.; Kim, H.-S.; Park, N.-G., Morphology-photovoltaic property correlation in perovskite solar cells: One-step versus two-step deposition of $CH_3NH_3PbI_3$. *APL Mater.* **2014,** *2* (8), 081510.

59. Xiao, M.; Huang, F.; Huang, W.; Dkhissi, Y.; Zhu, Y.; Etheridge, J.; Gray-Weale, A.; Bach, U.; Cheng, Y. B.; Spiccia, L., A fast deposition-crystallization procedure for highly efficient lead iodide perovskite thin-film solar cells. *Angew. Chem.* **2014,** *126*, 10056-10061.

60. Jeon, N. J.; Noh, J. H.; Kim, Y. C.; Yang, W. S.; Ryu, S.; Seok, S. I., Solvent engineering for high-performance inorganic-organic hybrid perovskite solar cells. *Nat. Mater.* **2014,** *13* (9), 897.

61. Song, T.-B.; Chen, Q.; Zhou, H.; Jiang, C.; Wang, H.-H.; Yang, Y. M.; Liu, Y.; You, J.; Yang, Y., Perovskite solar cells: film formation and properties. *J. Mater. Chem. A* **2015,** *3* (17), 9032-9050.

62. Ko, H.-S.; Lee, J.-W.; Park, N.-G., 15.76% efficiency perovskite solar cells prepared under high relative humidity: importance of PbI_2 morphology in two-step deposition of $CH_3NH_3PbI_3$. *J. Mater. Chem. A* **2015,** *3* (16), 8808-8815.

63. Jung, H. S.; Park, N. G., Perovskite solar cells: from materials to devices. *Small* **2015,** *11*, 10-25.

64. Brenner, T. M.; Rakita, Y.; Orr, Y.; Klein, E.; Feldman, I.; Elbaum, M.; Cahen, D.; Hodes, G., Conversion of single crystalline PbI_2 to $CH_3NH_3PbI_3$: Structural relations and transformation dynamics. *Chem. Mater.* **2016,** *28* (18), 6501-6510.

65. Cao, J.; Jing, X.; Yan, J.; Hu, C.; Chen, R.; Yin, J.; Li, J.; Zheng, N., Identifying the molecular structures of intermediates for optimizing the fabrication of high-quality perovskite films. *J. Am. Ceram. Soc.* **2016,** *138* (31), 9919-9926.

66. Chen, Y.; Chen, T.; Dai, L., Layer-by-layer growth of $CH_3NH_3PbI_{3-x}Cl_x$ for highly efficient planar heterojunction perovskite solar cells. *Adv. Mater.* **2015,** *27* (6), 1053-1059.

67. Liu, M.; Johnston, M. B.; Snaith, H. J., Efficient planar heterojunction perovskite solar cells by vapour deposition. *Nature* **2013,** *501* (7467), 395.

68. Baloch, A. A.; Hossain, M.; Tabet, N.; Alharbi, F., Practical Efficiency Limit of Methylammonium Lead Iodide Perovskite ($CH_3NH_3PbI_3$) Solar Cells. J. Phys. Chem. Lett.: **2018**; Vol. 9, p 426.

69. Bi, D.; Yi, C.; Luo, J.; Décoppet, J.-D.; Zhang, F.; Zakeeruddin, S. M.; Li, X.; Hagfeldt, A.; Grätzel, M., Polymer-templated nucleation and crystal growth of perovskite films for solar cells with efficiency greater than 21%. *Nature Energy* **2016,** *1*, 16142.

70. Shi, J.; Xu, X.; Li, D.; Meng, Q., Interfaces in perovskite solar cells. *Small* **2015,** *11* (21), 2472-2486.

71. Yan, L.; Xue, Q.; Liu, M.; Zhu, Z.; Tian, J.; Li, Z.; Chen, Z.; Chen, Z.; Yan, H.; Yip, H. L., Interface Engineering for All‐Inorganic CsPbI2Br Perovskite Solar Cells with Efficiency over 14%. *Adv. Mater.* **2018,** *30* (33), 1802509.

72. Li, N.; Zhu, Z.; Li, J.; Jen, A. K. Y.; Wang, L., Inorganic $CsPb_{1-x}Sn_xIBr_2$ for Efficient Wide‐Bandgap Perovskite Solar Cells. *Adv. Energy Mater.* **2018**, 1800525.

73. Liang, J.; Wang, C.; Wang, Y.; Xu, Z.; Lu, Z.; Ma, Y.; Zhu, H.; Hu, Y.; Xiao, C.; Yi, X., All-inorganic perovskite solar cells. *J. Am. Ceram. Soc.* **2016,** *138* (49), 15829-15832.

74. Wang, Y.; Zhang, T.; Kan, M.; Zhao, Y., Bifunctional Stabilization of All-Inorganic α-CsPbI3 Perovskite for 17% Efficiency Photovoltaics. *J. Am. Chem. Soc.* **2018,** *140* (39), 12345-12348.

75. Liang, J.; Zhao, P.; Wang, C.; Wang, Y.; Hu, Y.; Zhu, G.; Ma, L.; Liu, J.; Jin, Z., $CsPb_{0.9}Sn_{0.1}IBr_2$ based all-inorganic perovskite solar cells with exceptional efficiency and stability. *J. Am. Ceram. Soc.* **2017,** *139* (40), 14009-14012.

Chapter 2. Experimental section of the general methods and characterization techniques

In our research, during the preparation of the materials, device fabrication and characterization, the raw materials were used and the several characterization techniques were involved. Here the related materials, instruments and methodologies were introduced.

2.1 Reagents and apparatus

2.1.1 Reagents

The reagents used in our experiments are listed in the following table. In our experiments, all the reagents including solvents and powders were utilized directly without any purification.

Table 1. Chemical reagents employed in this thesis.

	Reagent	Purity	Company
1	Ti_3AlC_2	90%	Beijing Lianli Co.
2	Tetrabutyl titanate	AR	Sigma-Aldrich
3	Meso-TiO_2 paste	18NRD paste	Great Cell Solar (Dyesol) LTD.
4	ITO glass	glass	OPV Tech.
5	PbI_2	98%	Tokyo Chemical Industry Co., LTD.
6	CH_3NH_3I	99%	Wako Pure Chemical Industries
7	Li-TFSI	99.99%	Macklin Co., LTD.
8	Co-TFSI	99.99%	Macklin Co., LTD.
9	Spiro-MeOTAD	99.5%	Macklin Co., LTD.
10	$PbBr_2$	98%	Tokyo Chemical Industry Co., LTD.
11	SnCl2	100%	Wako Pure Chemical Industries

12	CsBr	99.9%	Xi'an Polymer Light Technology Corp.
13	$NbCl_5$	99%	Wako Pure Chemical Industries
14	Conductive carbon paste	N/A	Ningbo Borun Co., Ltd.
15	Ethanol	99.90%	Wako Pure Chemical Industries
16	Chlorobenzene	99.9%	Sigma-Aldrich
17	N, N-dimethylformamide	99.9%	Sigma-Aldrich
18	Dimethyl sulfoxide	99.9%	Sigma-Aldrich
19	4-tert-butylpyridine	99.9%	OPV Tech.
20	2-Propanol	99.90%	Wako Pure Chemical Industries
21	Acetonitrile	99.99%	Wako Pure Chemical Industries
22	Hydrofluoric Acid	50%	Wako Pure Chemical Industries
23	ethyl acetate	99.8%	Sigma-Aldrich
24	SnO_2 colloid	15% in H2O	Alfa Aesar,

2.1.2 Apparatus

During the preparation of the materials, fabrication of the photovoltaic devices and device performance testing, many apparatus and instruments were utilized. The following table is the apparatus and testing instruments employed in this thesis.

Table 2. Laboratory apparatus employed in this thesis.

	Apparatus	MODEL	Company
1	Electronic Balance	XFR-205DR	Shinko Denshi Co., Ltd.
2	Muffle Furnace	FO300	Yamato Scientific Co., Ltd., Japan
3	Oven	SDN/W-27	Sansyo Co., Ltd., Japan
4	Spin coater	SC-150	Oshigane Co., Ltd., Japan
5	Hot plate	C-MAG HS7	IKA Co., Ltd., Germany
6	Vacuum oven	SVD-30	Sansyo Co., Ltd., Japan
7	ASU cleaner	ASU-6	As one Co., Ltd., Japan
8	Tabletop centrifuge	EX0800-A000	Kubota Co., Ltd., Japan
9	Glove box	Super(1220/750/900)	MIKROUNA Co., Ltd., China
10	Digital meter	Keithley 2450	Teltronix, INC. Co., Ltd., USA
11	Solar simulator	CEP-2000	Bunkou Keiki Co., Ltd., Japan
12	Standard solar cell	BS-520BK	Bunkou Keiki Co., Ltd., Japan
13	Monochromatic illumination	G250 monochromator	Nikon
14	X-ray diffractometer	Rigaku	Rigaku Co., Ltd, Japan
15	Electrochemical impedance spectroscopy	1255B	Solartron Analytical
16	UV-visible spectrometer	V-670	JASSCO Co. Ltd., USA
17	Ionization energy measuring device	KV205-HK	Bunkoukeiki Co., Ltd, Japan
18	X-ray photoelectron spectroscopy	AXIS-HS	KRATOS Co., Ltd., Japan

19	Field emission-scanning electron microscope	JSM-6701F	JEOL Co., Ltd, Japan

2.2 Characterization methods

2.2.1 X-ray diffraction crystallography (XRD)

In our experiments, we use the XRD to identify the crystal structure of the perovskite materials and confirm if there are impurities. In the XRD measurements, the X-rays incidence can lead the atoms scatter the X-ray waves through the electrons of the atoms. During the scattering process, some waves cancel one another out in some directions via destructive interference process, while in some specific directions the waves are constructively added. These processes are determined by Bragg's law:

$$2\mathrm{d}\sin\theta = \mathrm{n}\lambda \tag{2-1}$$

In the equation, the d represents the space between the crystal plane of the certain crystal facet group, θ is the incident angle, n is an integer, and λ is the wavelength of the measuring beam. Through this characterization method, we can confirm if the prepared perovskite film is the expected phase and if there are some impurities such as unreacted PbI_2. Moreover, from the relative intensities of the peaks, we can know the crystal orientation of materials. In the researches of metal doping of perovskite materials, the variation of the irradiation peak positions is evidence for the lattice expansion or shrinking. In our measurements, the Rigaku Corp. device with Cu Kα irradiation (λ = 1.54056 Å) was used and the scanning rate is 5°/min.

2.2.2 Field emission scanning electron microscopy (FE-SEM)

FE-SEM is a type of electron microscopy technique can characterize the surfaces properties with a focused beam of electrons. The electron beam reaching to the surface can interact with atoms of different depth, generating various signals providing morphology information. We use the FE-SEM to characterized the morphologies of the perovskite films and confirm if there are pin-holes on the film surface. Specifically, the crystal size is the main character of the morphologies, which is significant to the light absorption ability and charge transfer properties. The pin-holes in the perovskite film is another main character of the morphologies and film quality, which determines the charge transfer through the layers and the recombination process due to the

contact of ESL and HTM. In our experiments, the FE-SEM characterizations were carried out on the JEOL JSM-6701F device with the working voltage of 5 -10 kV and working current of 15 μA.

2.2.3 Ultraviolet-visible spectroscopy (UV-Vis)

UV-Vis is absorption or reflection spectroscopy of a sample (in powder, liquid and film form) in the UV-visible spectral range. The color of the involved chemicals highly affect the absorption or reflectance spectra. When measuring the absorption properties of perovskite films, we use a UV-is spectrophotometer. The measured intensity (I) of the light through the sample is compared with the intensity (I_0) of that before passing the sample. The ratio of I/I_0 is defined as transmittance, which is expressed as a type of percentage (%T). In our research of the perovskite materials, we would like to evaluate the light absorbing ability of the material from the absorbance profile, moreover from which we can evaluate the bandgap of the material by constructing a Tauc plot. In our research, the UV-VIS-NIR spectrophotometer (V-670, JASSCO Co. Ltd., USA) was applied to characterize the optical properties of the samples by the absorption spectra.

2.2.4 Photoluminescence (PL) and Time-Resolved Photoluminescence (TRPL)

Photoluminescence (PL) is a light emitted when photoexcitation media decrease from one energy level to another. The energy of a specific luminescence transition depends on the initial states of the energy states. These states are bound to localized impurity or defect states, continuum levels in the conduction or valence band, exciton states (electron-hole pairs bound together by Coulomb attraction) and impurities or defects It can be in the excited exciton state.[1]

The structure and function of a device highly determines the dynamics of semiconductor charge carriers. Thus an accurate measurement of charge carrier lifetime is available only when characterize the device systems. For certain types of semiconductors, the lifetime of the carrier is determined by the properties of the materials involved and the interface. In addition, the surface effects of the sensitizer, passivation effect, the energy transfer property, and the presence impurities and defects can lead to significant fluctuations in the measured results. The general methodology and peripheral techniques of time-resolved photoluminescence (TRPL) via time-correlated single photon counting are highly relevant to the analysis of that phenomenon. Suitable for Determine the dynamics of fast charge carriers in semiconductors.

2.2.5 Electrochemical impedance spectrum (EIS)

EIS is a stechnique to analyze the impedance, resistance and charge transfer processes in PSC. Generally, in the high frequency range, the EIS spectrum is adapted to the parallel resistor and the capacitor circuit. This is related to the space charge layer of the light absorber film. At low frequency, the Nyquist plot always transits into a linear region, showing additional diffuse component to the total capacitance being recorded.[2] Generally, the high-frequency arc represents the charge transport process including the resistance and chemical capacitance of charge transport process, which are relating to the charge transporting from the conductive substrate to back electrode. While the arc at the low-frequency region represents the recombination resistance (R_{rec}) and the chemical capacitance (C_{rec}) belonging to the interface of perovskite/ESL and perovskite/HTM. In our research, the EIS was measured by the Solartron Analytical 1255B.

2.2.6 Photovoltaic performance measurement

The main feature of solar cells is the ability to convert light into electricity, which can be expressed as PCE, the ratio of output power to incident power. For determining the PCE, current-voltage (*J-V*) measurements are performed on the solar cell device. During the measurement, a series of voltages are applied to the solar cell under the illumination. The output voltage is measured at each voltage step, and as shown in Figure 1, a characteristic *J-V* curve can be obtained that can determine some important characteristics from the *J-V* curve. In general, current density (*J*) is used instead of current because the area of the cell affects the magnitude of the output current.

The PCE can be calculated by the following equation:

$$PCE = \frac{P_{out}}{P_{in}} = \frac{J_{sc} * V_{oc} * FF}{P_{in}} \quad (2\text{-}2)$$

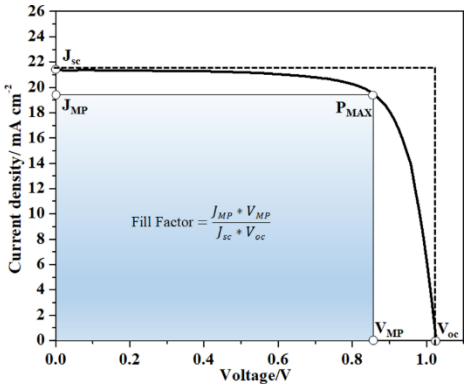

Figure 1 A typical J-V curve of PSCs.

J_{sc} is the photogenerated current density of the cell without applied bias. The J_{sc} value is affected by the light absorption, charge generation and extraction efficiencies of the light absoprtion layer. V_{oc} is the voltage at which the electric field is used. The V_{oc} is determined by the energy level of the photoactive material, the working function of the electrode material, and the charge carrier recombination rate at the photoactive layer or interface. FF is the ratio of the cell's actual power to the actual power without the series and shunt resistance.[3] The FF value can be calculated via the equation:

$$FF = \frac{P_{max}}{J_{sc} * V_{oc}} \quad (2\text{-}3)$$

The device performance of the PSCs were measured using Keithley 2450 and a xenon lamp at 100 mW cm^{-2} under AM 1.5G conditions. The cell area was fixed to be 0.08 cm^2 with a black mask.

References

1. https://www.picoquant.com/applications/category/materials-science/time-resolved-photoluminescence.
2. Li, Z.; Mercado, C. C.; Yang, M.; Palay, E.; Zhu, K., Electrochemical impedance analysis of perovskite-electrolyte interfaces. *Chem. Commun.* **2017,** *53* (16), 2467-2470.
3. https://www.ossila.com/pages/solar-cells-theory.

Chapter 3. Enhancing the performance by MXene additive

3.1 Introduction

The perovskite solar cells (PSCs) have attracted large attention because of its high-speed development in photoconversion efficiency (PCE) in the past years.[1-3] Though the highest certified PCE of 23.2% have been achieved,[4] there is still a long journey to go to achieve its theoretical efficiency limit of 30~33%.[5] Among the components of the PSCs device, the perovskite layer for light absorption and carrier transfer is always the central part that determines the device performance.[6-8] While the crystal size is the most important parameter for perovskite film. The larger crystal size promises higher charge carrier transformation efficiency and better performance because of less amount of grain boundaries.[9-10]

With the aim of enlarging the particle size of perovskite crystals, researchers have proposed various kinds of strategies, such as antisolvent optimizing,[11] post-treatment[12] and additive engineering.[13-14] Among which additive engineering is very promising and easy to operate. For instance, Wang et al. added water into the perovskite precursor and they found that the water additive can enhance the crystallization and surface coverage.[15] Gratzel group applied poly(methyl methacrylate) to control the crystal growth process, consequently, a high PCE of over 21% was achieved.[16] Han and co-workers used methylammonium acetate and thio-semicarbazide as additives have resulted in high crystalline quality of the perovskite, leading to enhanced PCE and durability of PSCs.[13] Moreover, except for the aforementioned soluble additive, some 2D nanomaterials with unique properties have also been used as additives in recent years. For example, Hagfeldt et al. introduced nitrogen-doped graphene into the perovskite layer and all the photovoltaic parameters were improved.[17] The graphene not only enlarged the grain size but also passivated the perovskite surface and reduced the charge recombination. More recently, another 2D compound, g-C_3N_4, was doped into the perovskite layer.[18] The g-C_3N_4 dopant improved grain size, reduced the intrinsic defect and more importantly, it increased the film conductivity of the perovskite layer. In addition, other 2D materials such as WS_2,[19] MoS_2[20] and black phosphorus[21] have also been used as an additive or buffer layer to enhance the device performance. Therefore,

the 2D layered nanomaterials, featuring unique morphology and excellent properties, are very promising additives for PSCs efficiency improvement.

MXene, a newly emerging class of 2D materials with the general formula of $M_{n+1}X_nT_x$, is obtainedd by selectively etching the A (Al, Sn, etc.) layer of MAX phase by hydrofluoric acid (HF) or in-situ generated HF. $Ti_3C_2T_x$ (T_x represents the termination group), a typical MXene, has many outstanding properties including high electronic conductivity (2.0×10^4 S cm^{-1}), high mobility (1 $cm^2V^{-1}S^{-1}$) and charge carrier density (3.8×10^{22} cm^{-3}).[22] More importantly, $Ti_3C_2T_x$ can be tuned by suitable modification of their surface chemistry, which substantially render controllable and extraordinary properties.[23-25] The aforementioned excellent properties ensure the wide applications of MXenes in supercapacitors, transparent electrodes, and ion batteries.[22, 26-27]

Herein, we used a typical MXene material, $Ti_3C_2T_x$, as an additive into the perovskite absorber layer. We found that the $Ti_3C_2T_x$ termination groups will retard the crystallization rate, increase the grain size of the perovskite layer, and its excellent electrical properties of MXene favor the charge transfer of PSCs. After optimization, a 12% PCE enhancement of PSCs can be obtained with 0.03 wt% amount of MXene additive.

3.2 Experimental Section

3.2.1 Preparation of $Ti_3C_2T_x$

The Ti_3AlC_2 was purchased from Beijing Lianli New Materials Corporation. Firstly, the purchased sample was screened with 325 mesh sifter and manual grinding for 30 min. Then 1 g Ti_3AlC_2 was slowly mixed with 15 ml, hydrochloric acid (HF) and then stirred at 300 rpm for 24 h, during which the temperature was kept around 35 ^oC. After 24 h, the residue was washed water under the centrifugation at 3500 rpm for 5 min and this was repeated for several times until the pH reached to 6. The remaining sediment was collected and dried in the vacuum oven for one night and $Ti_3C_2T_x$ sample was obtained. The etched powder was mixed with DMSO and stirred for 24 h. Then the obtained solution was centrifuged to separate the solid from the excess DMSO. Then the sample was mixed with 30 mL water and ice-bath sonicated for 3 h with argon bubbling. In order to obtain small particles, the dispersion was centrifuged for 1 h at 6000 rpm. The dark supernatant was obtained and it can be used directly when the $Ti_3C_2T_x$-water acted as the additive for perovskite precursor. For redispersing in other organic solvents, the dark supernatant was

filtered using a polypropylene membrane, and then dried in a vacuum oven. Finally, the dried $Ti_3C_2T_x$ sample with a form of film was dispersed into the organic solvents, followed by sonication for fully dispersing. The concentration of $Ti_3C_2T_x$ was kept at 0.5 mg ml^{-1}.

3.2.2 Precursor Preparation and Device Fabrication

1.38 M perovskite solution was prepared using MAI and PbI_2 (Tokyo Chemical Industry) with the solvents of DMF and DMSO (volume ratio of 4:1). The $Ti_3C_2T_x$ was dispersed in different solvent with the concentration of 0.5 mg ml^{-1}. Different amount of $Ti_3C_2T_x$ solution was added into the perovskite precursor, always keeping the original concentration of the perovskite and solvent ratio by reducing the original volume of DMF or DMSO. The SnO_2 colloid precursor (Alfa Aesar) was diluted to 2.67% and was spin coated on ITO substrate at 2000 rpm for 30 s, and then baked 150 ºC for 0.5 h. Subsequently, in the argon-filled glove box, the perovskite precursor solution was deposited on the SnO_2 layer via the spin-coating program at 4000 rpm for 30 s. At the 5th second, 150 µl ethyl acetate (EA) was dropped onto the substrate and finally, a transparent perovskite film was obtained. A dark perovskite film was generated after annealed at 100 ºC for 10 min. Then, 75 µl Spiro-OMeTAD (Sigma) solution was deposited on the perovskite layer at 4000 rpm for 30 s. Finally, an Au electrode was formed by evaporation at a pressure of 4×10^{-3} torr.

3.2.3 Characterizations

The characterization methods including XRD, SEM, UV-Vis spectra, EIS and J-V curve were introduced in Chapter 2. In addition, EDX was conducted by the Hitachi S-3400N. The IPCE was measured by monochromatic illumination (A 300 W Xenon arc lamp through Nikon G250 monochromator equipped).

3.3 Results and Discussion

As a very typical MAX phase, M (Ti element) layers of Ti_3AlC_2 are interleaved with the A (Al element) layers, with the X (C element) atoms filling the octahedral sites between the former.[28] When Ti_3AlC_2 materials are treated in HF solution, the Al layers can be selectively removed from the interlayers by disconnecting the metallic bonds between Al and Ti, resulting into 2D MXene, as schematically depicted in Figure 1a. From the SEM images, it can be found that the Ti_3AlC_2 displays an irregular morphology, with the size of several micrometers as shown in Figure 1b. Upon HF etching, the morphology altered drastically and very uniform micron-sized multilayers

were obtained (Figure 1c). The multilayers present loosely packed accordion-like morphology, and the layers were obviously separated from each other, which is similar to the lamellar graphite.

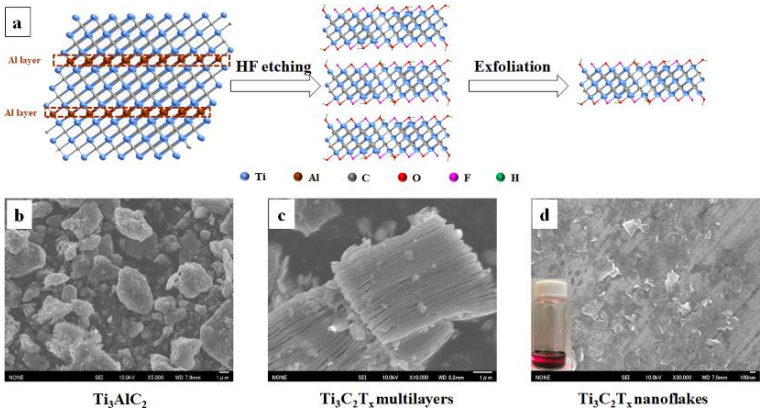

Figure 1 (a) Schematic illustration of Ti_3AlC_2 etching and $Ti_3C_2T_x$ exfoliation and SEM images of (b) Ti_3AlC_2 raw materials, (c) $Ti_3C_2T_x$ multilayers sample after HF etching, (d) $Ti_3C_2T_x$ nanoflakes dispersing in DMF (the inset is the solution under the laser radiation)

In order to confirm the phase variation brought by HF etching, the samples were tested by X-ray diffraction (XRD) and the patterns are shown in Figure 3. It can be found that the peaks of Ti_3AlC_2 phase disappear after HF etching. The presence of $Ti_3C_2T_x$ main phase indicates the successful etching of the Al layer.[28] The peaks at 36.0° and 41.6° are attributed to the impurity of TiC, which is used as raw materials for Ti_3AlC_2 synthesis and is difficult to be removed during HF etching. The irradiation peaks at 8.9°, 18.3° and 27.7° correspond to the (002), (006), (008) facet of $Ti_3C_2T_x$, respectively.[29-30] In order to further confirm the element distribution, X-ray photoelectron spectroscopy (XPS) was conducted for the $Ti_3C_2T_x$ multilayers. From the survey region (Figure 3b), the signals belonging to the element of C, Ti, O, F were clearly detected without signals for Al, which indicates fully etching of Al layer in MAX phase, in accordance with the XRD results. In the high-resolution XPS spectrum of the Ti 2p (Figure 3c), the components centered at 455.0, 455.7, 457.1 and 460.7 eV are assigned as Ti, Ti^{2+}, Ti^{3+} and $TiO_{2-x}F_x$, respectively. For the C 1s spectrum, the curve can be fitted by four components centered at 282.1, 282.0, 284.6, and 285.6 eV, which are attributed to C-Ti-O, C-Ti, C-C, and C-O, respectively. We also analyzed the O 1s spectrum and results displayed that the peaks can be fitted by two peaks at 530.0 and 531.7 eV for Ti-O and O-H, respectively. The existence of Ti-O, O-H, and Ti-F indicates the termination group, T_x, are O, OH, and F, which is in agreement with the previous reports.[31-34] Therefore, the $Ti_3C_2T_x$ multilayers were successfully obtained by HF etching.

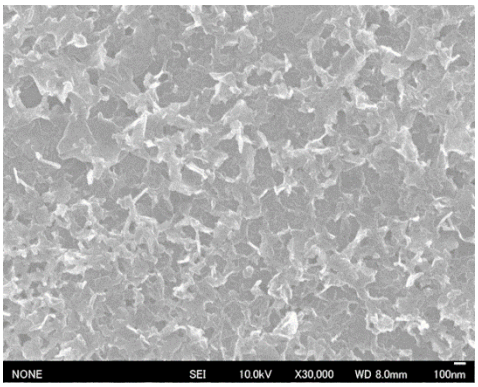

Figure 2 SEM image $Ti_3C_2T_x$ after exfoliation in water.

The $Ti_3C_2T_x$ multilayers, similar to other 2D materials, can be exfoliated easily due to weak interlayer van der Waals force.[35-36] Aiming at getting the smaller size and fewer layers, the $Ti_3C_2T_x$ multilayers were exfoliated in water under the sonication with Ar bubbling to avoid oxidation. Then the sample was centrifuged at the speed of 6000 rpm to remove the un-exfoliated multilayers and the impurity of TiC. SEM image of supernatants is shown in Figure 2 and comparing with the $Ti_3C_2T_x$ multilayers, the size and the number of layers are greatly reduced after sonication. The nanoflakes with the size of ~200 nm are interconnecting with each other, which is due to the incompletely split of large $Ti_3C_2T_x$ layers during the sonication process. Subsequently, the $Ti_3C_2T_x$ nanoflakes were dispersed in DMF.[37] As shown in Figure 1d, $Ti_3C_2T_x$ was separated from each other and the size was also further reduced. This can be attributed to the further sonication in a proper solvent, which promotes the splitting of interconnected nanoflakes into independent nanoflakes. At the same time, the dispersing solution displays the Tyndall effect under the irradiation of the laser, implying well-dispersion of $Ti_3C_2T_x$ nanoflakes in DMF solvent.

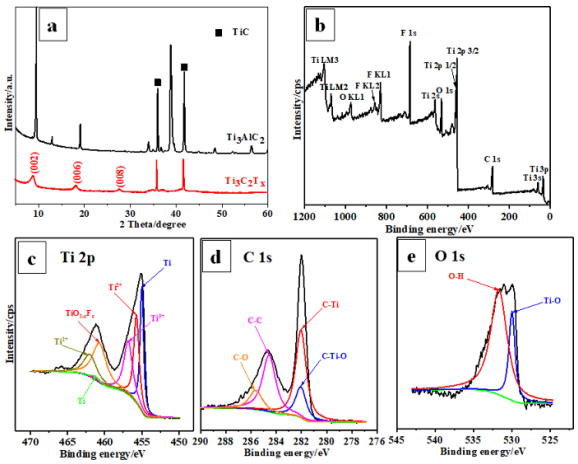

Figure 3 (a) XRD patterns of Ti_3AlC_2 raw materials (black line) and sample after HF etching (red line), (b) XPS spectra of $Ti_3C_2Ti_x$ sample and the high-resolution spectra of (c) Ti 2p, (d) C 1s and (e) O 1s.

To apply in PSCs, the $Ti_3C_2T_x$ nanoflakes dispersing in DMF solvent were introduced as the additive into the perovskite layer. Figure 4 shows the photograph of the perovskite precursor, where the solvent is DMF/DMSO mixed solvents. After introducing the $Ti_3C_2T_x$ into the precursor solution, it can be seen that the color changed from luminous yellow to dark yellow since the $Ti_3C_2T_x$ dispersing in solvents display as a black solution. The n-i-p planar structure of PSCs was fabricated to investigate the effect of $Ti_3C_2T_x$ additive on the device performance. The configuration of the devices is ITO/SnO_2/perovskite: $Ti_3C_2T_x$/Spiro-OMeTAD/Au, as shown in Figure 4.

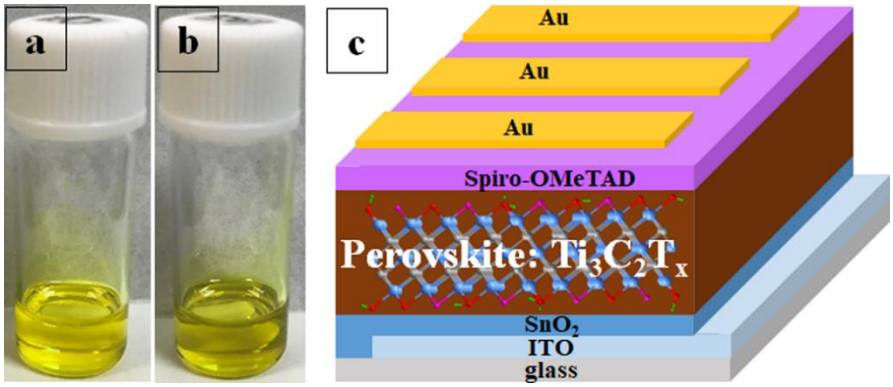

Figure 4 Photographs of (a) perovskite precursor and (b) perovskite precursor with $Ti_3C_2T_x$ additive, (c) the device configuration of $CH_3NH_3PbI_3$: $Ti_3C_2T_x$ based planar PSCs with n-i-p structure.

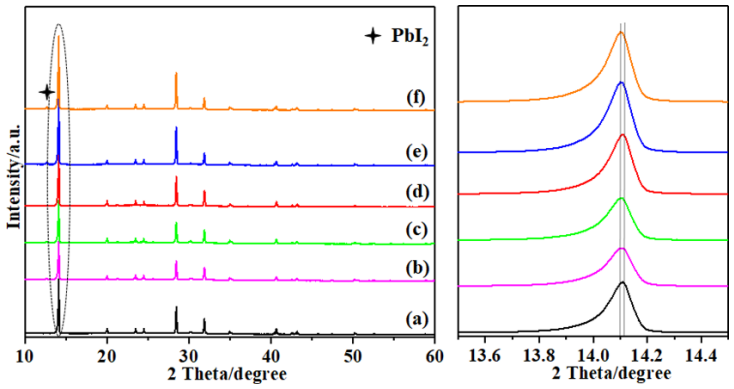

Figure 5 XRD patterns of the perovskite film with different amount of $Ti_3C_2T_x$ additive: (a) 0 wt%, (b) 0.01 wt%, (c) 0.02 wt%, (d) 0.03 wt%, (e) 0.05 wt%, (f) 0.1 wt% and the enlarged XRD patterns in the range from 13.5° to 14.5°.

Figure 5 displays the XRD patterns of samples with a different amount of $Ti_3C_2T_x$ additive relative to the weight of the perovskite precursor, from 0 to 0.1 wt%. All the samples present a cubic perovskite phase with a very weak peak belonging to the PbI_2 phase and the main peak at around 14.1° corresponds to (110) crystal plane of $CH_3NH_3PbI_3$ phase. We enlarged the main peak at around 14.1° and it can be found that the peak was slightly shifted towards lower angle while keeping the positions of the other peaks the same. Therefore, the peak shift is attributed to the stress brought by $Ti_3C_2T_x$ additive, suggesting the perovskite crystals experienced homogenous strain during the growing process.[38] We further improved the amount of additive to 0.25 wt% and the obtained sample (Figure 6) displays a similar XRD profile while the main peak at around 14.1° was shifted to a lower angle, as compared to other samples.

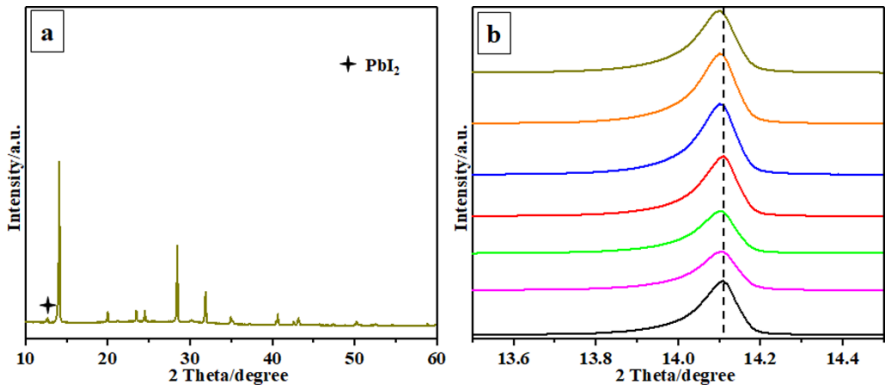

Figure 6 (a) XRD pattern of the perovskite film with 0.25 wt% $Ti_3C_2T_x$-DMF additive and (b) the enlarged XRD patterns of different perovskite films in the range from 13.5° to 14.5°. (from the bottom up: 0 to 0.25 wt%)

In order to further examine the perovskite film quality either with or without additive, the films were characterized by SEM, as shown in Figure 7. All the samples are in uniform morphology with no obvious pin-holes, which promises for high device performance. Comparing with the pristine film, the films with MXene additive show larger crystal size, especially 0.03 wt% $Ti_3C_2T_x$.

To accurately measure the crystal size of the perovskite films, the specific crystal size distributions were plotted and the results were shown in Figure 8. Clearly, the average grain size

of the perovskite was increased from 150 to 358 nm after the introduction of 0.03 wt% amount of additive, comparing with that of the sample without an additive. Moreover, all the perovskite films with $Ti_3C_2T_x$ additive possess a larger grain size than that of the perovskite layer without the additive. Generally, the larger grain size of perovskite means less amount of grain boundaries, thereby favoring the carrier transformation through the boundaries. This suggests that the addition of $Ti_3C_2T_x$ additive enable the growth of larger perovskite grain size.

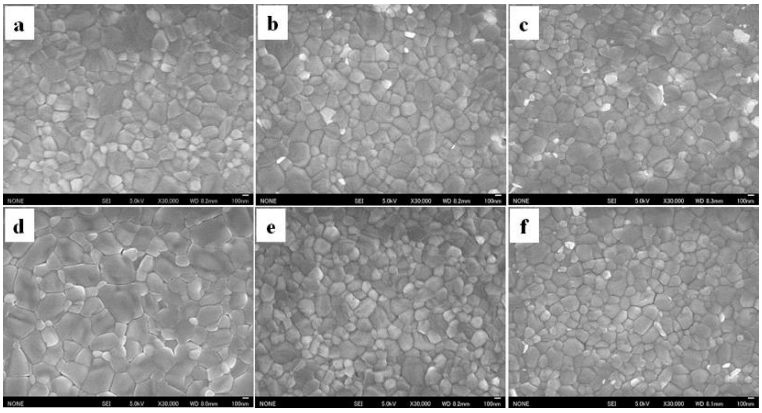

Figure 7 SEM images of the perovskite film with different amount of $Ti_3C_2T_x$-DMF additive: (a) 0 wt%, (b) 0.01 wt%, (c) 0.02 wt%, (d) 0.03 wt%, (e) 0.05 wt% and (f) 0.1 wt%.

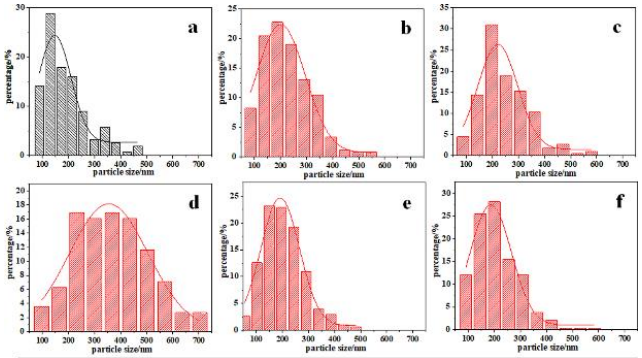

	a	b	c	d	e	f
PSCs	0 wt%	0.01 wt%	0.02 wt%	0.03 wt%	0.05 wt%	0.10 wt%
Average size (nm)	150	203	222	358	193	187

Figure 8 Statistical distributions of the perovskite film with different amount of $Ti_3C_2T_x$-DMF additive: (a) 0 wt%, (b) 0.01 wt%, (c) 0.02 wt%, (d) 0.03 wt%, (e) 0.05 wt% and (f) 0.1 wt% and the average size of different samples.

SEM images reveal that $Ti_3C_2T_x$ is non-detectable from the perovskite films at low weight ratio (0.01-0.1 wt%) loading. In order to investigate the location of $Ti_3C_2T_x$ additive, we then

increased the amount of the additive to 0.25 wt%, as shown in Figure 9. Sheet-like particles were on the surface and the boundary of the perovskite film, respectively. To further confirm their composition, we carried out the EDX measurement for the samples, as shown in Figure 10. Several peaks attributed to titanium element are observed through EDX spectrum, which indicates the existence of the titanium element.[39] Through the element mapping analysis, it shows that the titanium element is homogeneously distributed. The slightly low signal of the titanium element is due to the usage of very low concentration. Therefore, when a small amount of $Ti_3C_2T_x$ additive was introduced into the perovskite film, the sheet particles only existed in the grain boundary. This may then induce mechanical stress to the perovskite crystals and result in the shift of the main irradiation peak, which is consistent with the XRD results. Whereas, when a larger amount of $Ti_3C_2T_x$ additive was introduced into the film, the excess additive would be extruded to the surface of the film (Figure 9). In our previous research using Spiro-OMeTAD as the additive to modify the perovskite film, the excess additive was also extruded to the surface from the grain boundary.[40]

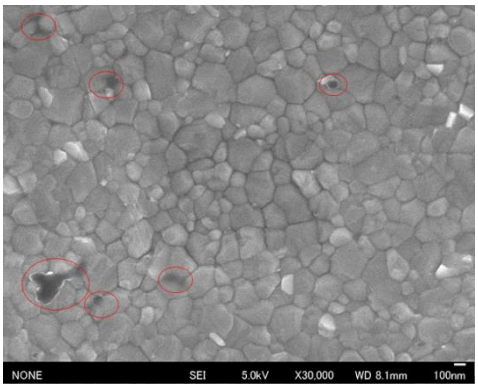

Figure 9 SEM image of the perovskite film with 0.25 wt% $Ti_3C_2T_x$-DMF additive.

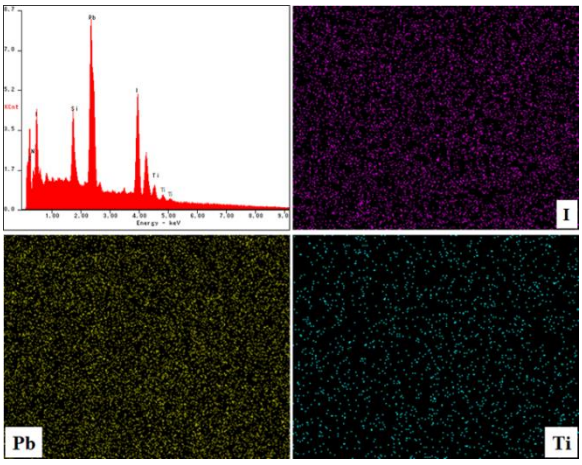

Figure 10 EDX spectrum of the perovskite film with 0.25 wt% $Ti_3C_2T_x$-DMF additive and element mapping of I, Pb and Ti.

On the basis of the discussion above, we propose a nucleation and growth route of perovskite film with the $Ti_3C_2T_x$ additive, as shown in Figure 11. Firstly, the perovskite precursor with or without additive was spin coated on the SnO_2 surface and ethyl acetate was used as anti-solvent. As depicted in the Figure, the $Ti_3C_2T_x$ possesses abundant termination groups of O, OH, and F on its surface. In the research of Hagfeldt et al, they used N-doped graphene as an additive. The basic sites on N-doped graphene could interact with the hydrogen atoms of the $[HC(NH_2)_2]$ (FA), which retards the crystallization process and leads to large perovskite grains.[17] The similar situation was also been reported by Liao et al when they used g-C_3N_4 as an additive because protonation occurs at the most basic centers.[18] In our case, the basic fluorine on the surface of $Ti_3C_2T_x$ can make the protonation occur with hydrogen atoms of the MA, thus forming the interaction between fluorine and CH_3NH_3 (MA). Moreover, Wang et al[41] found that when N, N′-bis-[2-(ethanoic acid sodium)]-1,4,5,8-naphthalene diimide modified graphene was used as the interface layer between electron selective layer, N-H$^{\cdots}$I$^-$ van der Waals interaction formed between the modified graphene and MAI. Therefore, in our case, the OH groups are hypothesized to have interaction with MAI, forming O-H$^{\cdots}$I$^-$ van der Waals interaction. Due to the interaction between the additive and MAI, during the anti-solvent dripping, the nucleus generates around the additive and the number of the nucleus is suppressed, implies retardation in the nucleation process.[42] While without additive, more nucleus will be generated uniformly on the SnO_2 layer. The additive disperses well in the DMF solvent, then the perovskite precursor may experience a homogeneous nucleation process. Finally, the perovskite film was annealed on the hot plate, during which the film was transformed into a dense perovskite phase. Since the film with additive generates lesser nuclei, the crystal growth is slower than that of the pristine film. After the transformation process, larger perovskite crystals could be obtained in the presence of $Ti_3C_2T_x$ as an additive. Therefore, using $Ti_3C_2T_x$ as an additive can effectively increase the grain size of the perovskite film.

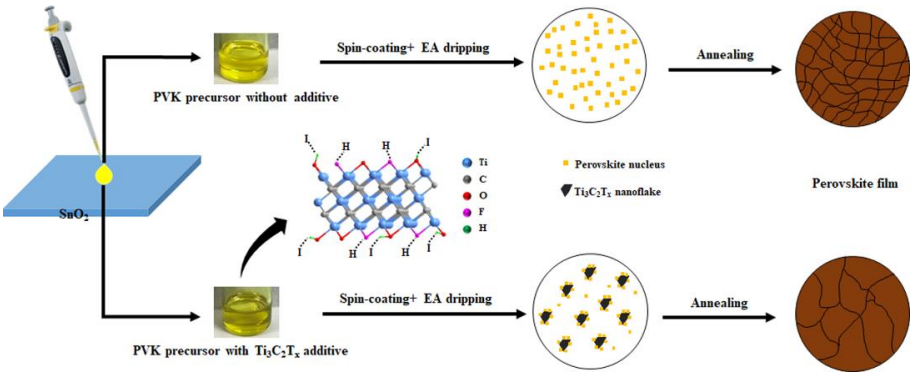

Figure 11 Proposed nucleation and growth route of perovskite film with and without $Ti_3C_2T_x$ additive

The light absorption ability of different perovskite films deposited on SnO_2/ITO substrates was investigated by UV-vis spectra and the results are presented in Figure 12a. All the perovskite films show an absorption onset lying at 800 nm together with a spectrally broad absorption feature in the region. By comparing the absorption curves, the perovskite films with $Ti_3C_2T_x$ additive display an enhancement of light absorption abilities. This phenomenon was attributed to the role of the $Ti_3C_2T_x$ present in the perovskite grain crystals. The particle size of the grains deeply influence the scattering behavior of the incident light and the larger grain size can enhance the light scattering.[43-44] Therefore, the perovskite film with 0.03 wt% additive incorporation rendered the largest crystal size, hence displayed the highest light absorption ability.

Figure 12b and Table 1 display the performance of the devices with and without additive modification. The devices with 0.01, 0.02 and 0.03 wt% of additives show better PCE than the pristine device. The highest PCE of 17.41% for the 0.03 wt% additive based device was achieved with J_{sc}, V_{oc}, and FF of 22.26 mA/cm^2, 1.03 V, and 0.76, respectively in the reverse scan, while 15.54%, 20.67 mA/cm^2, 1.00 V, and 0.75 for the pristine device.

The enhancement of J_{sc} in 0.03 wt% additive incorporated device is in agreement with the IPCE in Figure 13a. A photocurrent of 21.60 mA/cm^2 is slightly lower (with the difference of 2.96%) when compared to the Jsc of 22.26 mA/cm^2 obtained from *J-V* curves. This should be attributed to the lower illumination intensity in the IPCE measurement, in which the recombination process is more prominent since the existance of trap states and space charge effects.[45] In order to check the stability of the additive incorporated device, the steady-state photocurrent and efficiency were measured at the maximum power point of 0.848 V (Figure 13b). After continuous irradiation

for 180 s, the current density and PCE are stabilized at 20.08 mA/cm^2 and 17.03%, respectively, which is well agreed with PCE obtained from the *J-V* curve. The improvement in Jsc for the 0.03 wt% additive based device should be attributed to the large average crystal size and the reduction of small grains (Figure 8a and d) between larger grains. While further increasing the amount of the additive leads to decrement in PCE of the devices. The striking reduction lies in FF and V_{oc}, which should be attributed to the perovskite-Spiro interface variation with the increasing amount of the additive. This is because when excess $Ti_3C_2T_x$ additive was added to the perovskite film, they would aggregate on the surface of the film, which might act as the carrier recombination centers.[46]

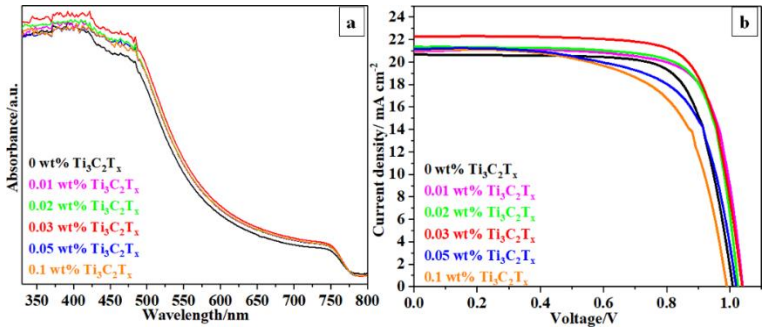

Figure 12 (a) UV-Vis spectra of the perovskite film and (b) *J-V* curves of PSCs with different amount of $Ti_3C_2T_x$.

Table 1 Performance of PSCs with different amount of $Ti_3C_2T_x$-DMF additive.

Amount/Parameter	V_{oc}/V	J_{sc}/mA cm^{-2}	FF	PCE/%
0 wt%	1.00	20.67	0.75	15.54
0.01 wt%	1.03	20.96	0.76	16.54
0.02 wt%	1.02	21.36	0.76	16.68
0.03 wt%	1.03	22.26	0.76	17.41
0.05 wt%	1.01	21.17	0.68	14.49
0.1 wt%	0.98	21.07	0.65	13.49

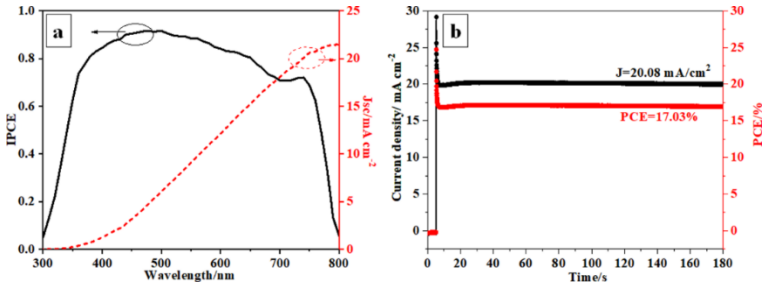

Figure 13 (a) Incident photon-to-electron conversion efficiency (IPCE) curve (black line) of the 0.03 wt% $Ti_3C_2T_x$ additive based device and the integrated photocurrent (red line) calculated from the overlap integral of the IPCE spectrum. (b) Maximal steady-state photocurrent output at the maximum power point of 0.848 V for 0.03 wt% additive based device and their corresponding power output.

In order to verify the reproducibility of the high efficiencies for the additive incorporated device, we fabricated more cells and the detailed statistics of the photovoltaic parameters for the devices were presented in Figure 14 and Table 2. The results clearly show that all the parameters were enhanced when the optimum amount of additive was added into the perovskite film. The improvement in FF is ascribed to the larger grains because less amount of total grain boundaries will promote the charge transporting.[44] Besides the larger crystal size, the increase in V_{oc} can be ascribed to the perovskite surface-passivation by $Ti_3C_2T_x$ nanoflakes, which is helpful for improving the hole selectivity and reducing the hole recombination at interface.[47]

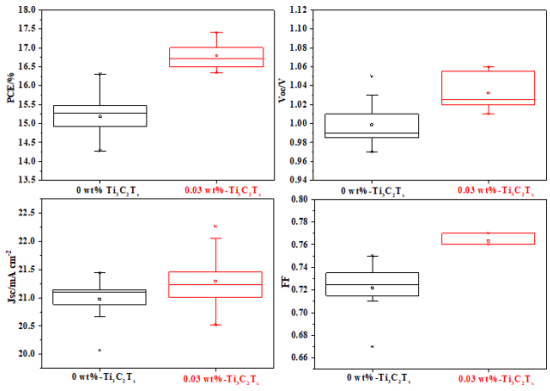

Figure 14 Photovoltaic statistics for 0 wt% and 0.03 wt% $Ti_3C_2T_x$ additive based device (18 cells for either type): (a) PCE, (b) V_{oc}, (c) J_{sc} and (d) FF.

Table 2 Photovoltaic parameters for 0 wt% and 0.03 wt% $Ti_3C_2T_x$ additive based device (18 cells for either type)

Amount/Parameter	V_{oc} /V	J_{sc}/mA cm^{-2}	FF	PCE/%
0 wt% $Ti_3C_2T_x$	1.00±0.02	20.98±0.37	0.72±0.02	15.18±0.50
0.03 wt% $Ti_3C_2T_x$	1.03±0.02	21.31±0.51	0.76±0.01	16.80±0.35

It has been reported that by reducing the internal resistance of the device, the J_{sc} will be increased because higher conductivity can promote the electron transfer process.[48] Therefore, we

used the EIS to characterize the device conductivity, as shown in Figure 15. The series resistance (R_s) and the charge transfer resistance (R_{CT}) can be depicted using the equivalent circuit consisting of R_s, R_{CT} and a parallel capacitor C.[18] As a result, it is obvious that the R_{CT} is also reduced from 7000 to 1800 Ω, which means that the conductivity of the perovskite film is increased. Therefore, the high electrical conductivity and mobility of $Ti_3C_2T_x$ additive are beneficial to reduce the R_{CT} and promote the charge transfer process, consequently enhance the J_{sc}.

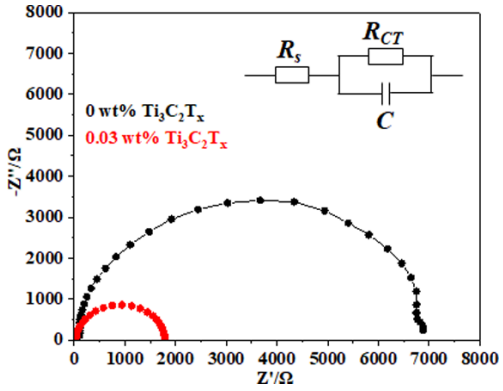

Figure 15 (a) Nyquist plots of 0 wt% and 0.03 wt% $Ti_3C_2T_x$ additive based device measured in the dark with a bias of 0.7 V.

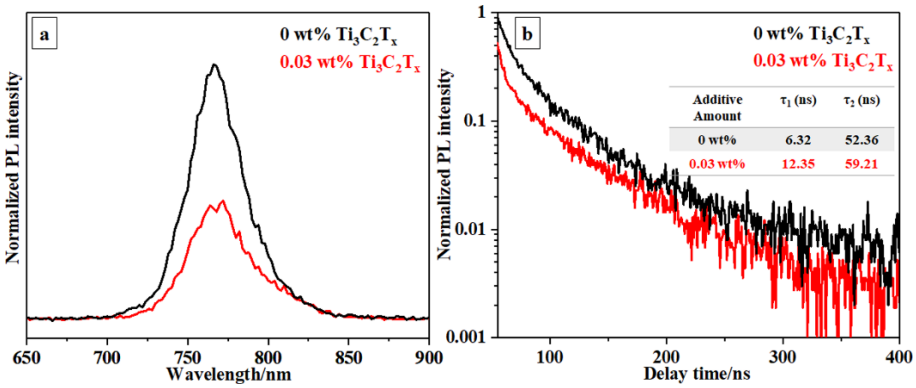

Figure 16 (a) Steady-state PL spectra and (b) time-resolved PL spectra of the perovskite film with and without $Ti_3C_2T_x$ additive.

Figure 16a gives the PL spectra of perovskite film with and without $Ti_3C_2T_x$ additive on bare glass substrates. The PL intensity of the sample with the additive is obviously weaker than that of the pristine perovskite film, meaning enhanced charge extraction process and the suppressed charge recombination process.[18, 49] This might be attributed to the better conductivity after introducing high conductivity additive, which is in accordance with the EIS results. Moreover, we

measured the time-resolved PL (TRPL) spectra of the film with and without the additive, as shown in Figure 16b. PL lifetime parameters obtained from a biexponential fitting are listed in the Table inserted in Figure 16b. We can find that the PL decay is nearly two times slower for perovskite film containing additive (τ_1=12.35 ns) when comparing with the pristine film (τ_1=6.32 ns). The longer lifetimes can be attributed to the reduced non-radiative recombination due to the presence of the additive.[17, 50] The TRPL is in consistance with that of the PL intensity. Therefore, introducing the high conductivity $Ti_3C_2T_x$ additive can result in superior carrier transport behavior of the perovskite film and better device performance.

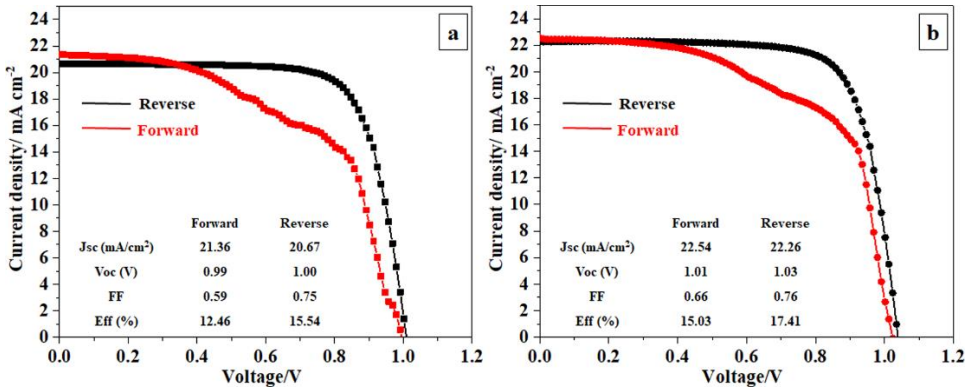

Figure 17 *J-V* curves of (a) 0 wt% and (b) 0.03 wt% $Ti_3C_2T_x$ additive based device by forward and reverse scan.

We also studied the effect of the additive on the device hysteresis, as shown in Figure 17. The pristine device displays PCE of 12.46 % (forward scan) and 15.54 % (reverse scan) with a difference of 19.8 %. According to the literature, when the mesoporous structure was employed, the device possesses greatly reduced hysteresis, therefore, the difference between the performance of forward and reverse scans should be attributed to the planar PSCs configuration in our research.[51-52] When the additive was incorporated within the perovskite film, the hysteresis, to some extent, was reduced to PCE of 15.03 % (forward scan) and 17.41 % (reverse san) with the difference of 13.7 %. The main reason here is that the enlarged grains reduce the presence of trap states at the grain boundary, resulting in suppressed carrier recombination.[53] Therefore, $Ti_3C_2T_x$ dispersing in DMF is an effective additive to enhance the performance of the PSCs. Besides the DMF, we also used water and DMSO as the solvent for $Ti_3C_2T_x$ additive and the results are shown and discussed in the supporting information.

Besides DMF, we also used water and DMSO as the solvent for $Ti_3C_2T_x$ additive. As for water, we fabricated the PSCs with the additive amount of 0.01, 0.03 and 0.05 wt%. However, the PCEs are lower than that of the pristine device, especially in the J_{sc}, as shown in Figure 18 and Table 3. The SEM image of the perovskite film with 0.03 wt% amount of $Ti_3C_2T_x$ additive was shown in Figure 19. We observe that there are many pin-holes in the film, which may lead to direct contact of Spiro and SnO_2 layer, resulting in reduced J_{sc}. There are two reasons for this phenomena. The first one is that a little more water was added into the precursor comparing to the optimized volume ratio when water was added as an additive, which gives rise to a negative effect on the film quality. The second one should be the dispersing quality of $Ti_3C_2T_x$ in water. As shown in Figure 2, the interconnected $Ti_3C_2T_x$ nanoflakes dispersed in water are larger in size than that of the sample in DMF, thus the additive cannot play adequate roles in enhancing the performance.

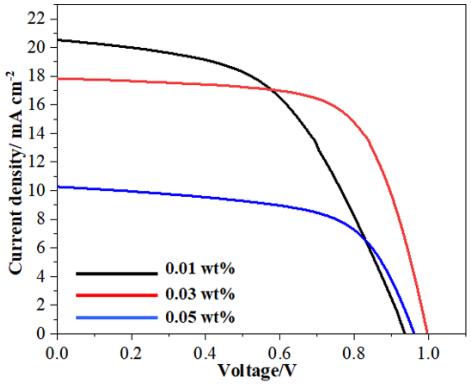

Figure 18 J-V curves of PSCs with $Ti_3C_2T_x$-water additive.

Table 3 Performance of PSCs with $Ti_3C_2T_x$-water additive.

Amount/parameter	V_{oc}/V	J_{sc}/mA cm^{-2}	FF	PCE/%
0.01 wt%	0.92	20.52	0.52	9.90
0.03 wt%	0.99	17.83	0.67	11.91
0.05 wt%	0.96	10.27	0.61	6.01

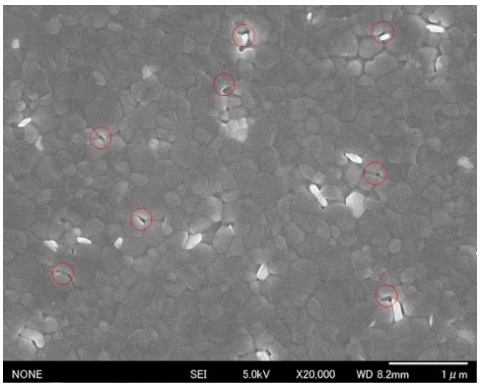

Figure 19 SEM image of the perovskite film with 0.03 wt% amount of $Ti_3C_2T_x$-water additive.

The results for DMSO were shown in Figure 20 and Table 4. The PCEs of the devices are almost the same as that of the pristine device. Figure 21 shows the SEM image of the $Ti_3C_2T_x$ dispersing in DMSO, in which we can find that the exfoliated nanoflakes are aggregated. We suppose that the aggregation of the additive will be avoided during the spin-coating process. Therefore, the additive seems to have no effect on device performance. Therefore, selecting a proper solvent is significantly important to improve the dispersing quality of $Ti_3C_2T_x$ nanoflakes and their applications. It has been reported that when the polarity of the solvent is somewhat similar to the polar termination groups presenting on the surface of $Ti_3C_2T_x$ nanoflakes, it will be able to disperse $Ti_3C_2T_x$ well. The polarity sequence of solvents is water > DMSO > DMF. Thus DMF with the smallest polarity, similar to that of the termination groups, is favorable for $Ti_3C_2T_x$ dispersion.

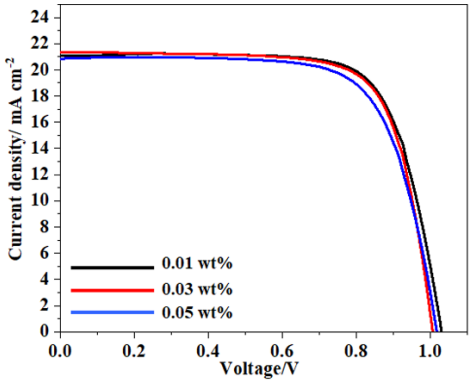

Figure 20 *J-V* curves of PSCs with $Ti_3C_2T_x$-DMSO additive.

Table 4 Performance of PSCs with $Ti_3C_2T_x$-DMSO additive.

Amount/parameter	V_{oc}/V	J_{sc}/mA cm^{-2}	FF	PCE/%
0.01 wt%	1.02	21.09	0.74	15.98
0.03 wt%	1.00	21.37	0.74	15.80
0.05 wt%	1.01	20.86	0.72	15.12

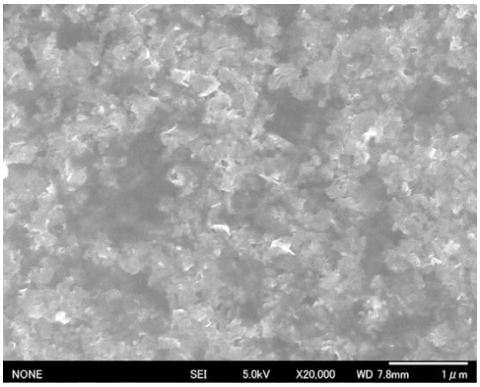

Figure 21 SEM image of $Ti_3C_2T_x$ nanoflakes dispersing in DMSO.

3.4 Conclusions

In summary, we have demonstrated a novel strategy to modify the perovskite layer by introducing a 2D layered $Ti_3C_2T_x$ MXene into the perovskite precursor. The additive can retard the nucleation process of the perovskite, resulting in larger grain size. Moreover, the additive with high conductivity and mobility is highly beneficial to accelerate the electron transfer through the grain boundary. After optimizing key parameters, we found that 0.03 wt% is the optimal amount and DMF is the most proper solvent for MXene additive. Accordingly, the highest PCE is improved from 15.54% to 17.41% and the average PCE is increased from 15.18% to 16.80%. This finding opens a new pathway to other kinds of MXene materials that are viable for PSCs application, typically for film modification and interface passivation between the perovskite layer and hole transfer layer.

References

1. Saliba, M., Perovskite solar cells must come of age. *Science* **2018,** *359*, 388-389.

2. Saliba, M.; Correa‐Baena, J. P.; Grätzel, M.; Hagfeldt, A.; Abate, A., Perovskite solar cells: From the atomic level to film quality and device performance. *Angew. Chem. Int. Ed.* **2018,** *57*, 2554-2569.

3. Guo, Z.; Gao, L.; Zhang, C.; Xu, Z.; Ma, T., Low-temperature processed non-TiO_2 electron selective layers for perovskite solar cells. *J. Mater. Chem. A* **2018,** *6*, 4572-4589.

4. Jeon, N. J.; Na, H.; Jung, E. H.; Yang, T.-Y.; Lee, Y. G.; Kim, G.; Shin, H.-W.; Il Seok, S.; Lee, J.; Seo, J., A fluorene-terminated hole-transporting material for highly efficient and stable perovskite solar cells. *Nat. Energy* **2018,** *3*, 682-689.

5. Baloch, A. A.; Hossain, M.; Tabet, N.; Alharbi, F., Practical Efficiency Limit of Methylammonium Lead Iodide Perovskite ($CH_3NH_3PbI_3$) Solar Cells. J. Phys. Chem. Lett.: **2018**; Vol. 9, p 426.

6. Jeon, N. J.; Noh, J. H.; Yang, W. S.; Kim, Y. C.; Ryu, S.; Seo, J.; Seok, S. I., Compositional engineering of perovskite materials for high-performance solar cells. *Nature* **2015,** *517*, 476.

7. Correa-Baena, J.-P.; Saliba, M.; Buonassisi, T.; Grätzel, M.; Abate, A.; Tress, W.; Hagfeldt, A., Promises and challenges of perovskite solar cells. *Science* **2017,** *358*, 739-744.

8. Montcada, N. F.; Méndez, M.; Cho, K. T.; Nazeeruddin, M. K.; Palomares, E., Photo-induced dynamic processes in perovskite solar cells: the influence of perovskite composition in the charge extraction and the carrier recombination. *Nanoscale* **2018,** *10*, 6155-6158.

9. Listorti, A.; Juarez-Perez, E. J.; Frontera, C.; Roiati, V.; Garcia-Andrade, L.; Colella, S.; Rizzo, A.; Ortiz, P.; Mora-Sero, I., Effect of mesostructured layer upon crystalline properties and device performance on perovskite solar cells. *J. Phys. Chem. Lett.* **2015,** *6*, 1628-1637.

10. Jung, H. S.; Park, N. G., Perovskite solar cells: from materials to devices. *Small* **2015,** *11*, 10-25.

11. Xiao, M.; Huang, F.; Huang, W.; Dkhissi, Y.; Zhu, Y.; Etheridge, J.; Gray-Weale, A.; Bach, U.; Cheng, Y. B.; Spiccia, L., A fast deposition-crystallization procedure for highly efficient lead iodide perovskite thin-film solar cells. *Angew. Chem.* **2014,** *126*, 10056-10061.

12. Hong, L.; Hu, Y.; Mei, A.; Sheng, Y.; Jiang, P.; Tian, C.; Rong, Y.; Han, H., Improvement and Regeneration of Perovskite Solar Cells via Methylamine Gas Post-Treatment. *Adv. Funct. Mater.* **2017,** *27*, 1703060.

13. Wu, Y.; Xie, F.; Chen, H.; Yang, X.; Su, H.; Cai, M.; Zhou, Z.; Noda, T.; Han, L., Thermally stable $MAPbI_3$ perovskite solar cells with efficiency of 19.19% and area over 1 cm^2 achieved by additive engineering. *Adv. Mater.* **2017,** *29*, 1701073.

14. Zheng, H.; Zhu, L.; Hu, L.; Yang, S.; Chen, S.; Alsaedi, A.; Hayat, T.; Huang, Y.; Pan, X.; Dai, S., Promoting perovskite crystal growth to achieve highly efficient and stable solar cells by introducing acetamide as an additive. *J. Mater. Chem. A* **2018**.

15. Gong, X.; Li, M.; Shi, X. B.; Ma, H.; Wang, Z. K.; Liao, L. S., Controllable Perovskite Crystallization by Water Additive for High-Performance Solar Cells. *Adv. Funct. Mater.* **2015,** *25*, 6671-6678.

16. Bi, D.; Yi, C.; Luo, J.; Décoppet, J.-D.; Zhang, F.; Zakeeruddin, S. M.; Li, X.; Hagfeldt, A.; Grätzel, M., Polymer-templated nucleation and crystal growth of perovskite films for solar cells with efficiency greater than 21%. *Nature Energy* **2016,** *1*, 16142.

17. Hadadian, M.; Correa-Baena, J. P.; Goharshadi, E. K.; Ummadisingu, A.; Seo, J. Y.; Luo, J.; Gholipour, S.; Zakeeruddin, S. M.; Saliba, M.; Abate, A., Enhancing Efficiency of Perovskite Solar Cells via N-doped Graphene: Crystal Modification and Surface Passivation. *Adv. Mater.* **2016,** *28*, 8681-8686.

18. Jiang, L. L.; Wang, Z. K.; Li, M.; Zhang, C. C.; Ye, Q. Q.; Hu, K. H.; Lu, D. Z.; Fang, P. F.; Liao, L. S., Passivated Perovskite Crystallization via g-C3N4 for High-Performance Solar Cells. *Adv. Funct. Mater.* **2018,** *28*, 1705875.

19. Ma, C.; Shi, Y.; Hu, W.; Chiu, M. H.; Liu, Z.; Bera, A.; Li, F.; Wang, H.; Li, L. J.; Wu, T., Heterostructured $WS_2/CH_3NH_3PbI_3$ photoconductors with suppressed dark current and enhanced photodetectivity. *Adv. Mater.* **2016,** *28*, 3683-3689.

20. Capasso, A.; Matteocci, F.; Najafi, L.; Prato, M.; Buha, J.; Cinà, L.; Pellegrini, V.; Carlo, A. D.; Bonaccorso, F., Few-Layer MoS_2 Flakes as Active Buffer Layer for Stable Perovskite Solar Cells. *Adv. Energy Mater.* **2016,** *6*, 1600920.

21. Chen, W.; Li, K.; Wang, Y.; Feng, X.; Liao, Z.; Su, Q.; Lin, X.; He, Z., Black Phosphorus Quantum Dots for Hole Extraction of Typical Planar Hybrid Perovskite Solar Cells. *J. Phys. Chem. Lett.* **2017,** *8*, 591-598.

22. Dillon, A. D.; Ghidiu, M. J.; Krick, A. L.; Griggs, J.; May, S. J.; Gogotsi, Y.; Barsoum, M. W.; Fafarman, A. T., Highly Conductive Optical Quality Solution-Processed Films of 2D Titanium Carbide. *Adv. Funct. Mater.* **2016,** *26*, 4162-4168.

23. Dall'Agnese, Y.; Lukatskaya, M. R.; Cook, K. M.; Taberna, P.-L.; Gogotsi, Y.; Simon, P., High capacitance of surface-modified 2D titanium carbide in acidic electrolyte. *Electrochem. Commun.* **2014,** *48*, 118-122.

24. Enyashin, A. N.; Ivanovskii, A. L., Structural and electronic properties and stability of MXenes Ti_2C and Ti_3C_2 functionalized by methoxy groups. *The Journal of Physical Chemistry C* **2013,** *117*, 13637-13643.

25. Peng, Q.; Guo, J.; Zhang, Q.; Xiang, J.; Liu, B.; Zhou, A.; Liu, R.; Tian, Y., Unique lead adsorption behavior of activated hydroxyl group in two-dimensional titanium carbide. *J. Am. Chem. Soc.* **2014,** *136*, 4113-4116.

26. Wang, X.; Kajiyama, S.; Iinuma, H.; Hosono, E.; Oro, S.; Moriguchi, I.; Okubo, M.; Yamada, A., Pseudocapacitance of MXene nanosheets for high-power sodium-ion hybrid capacitors. *Nat. Commun.* **2015,** *6*, 6544.

27. Naguib, M.; Halim, J.; Lu, J.; Cook, K. M.; Hultman, L.; Gogotsi, Y.; Barsoum, M. W., New two-dimensional niobium and vanadium carbides as promising materials for Li-ion batteries. *J. Am. Chem. Soc.* **2013,** *135*, 15966-15969.

28. Feng, A.; Yu, Y.; Jiang, F.; Wang, Y.; Mi, L.; Yu, Y.; Song, L., Fabrication and thermal stability of NH_4HF_2-etched Ti_3C_2 MXene. *Ceram. Int.* **2017,** *43*, 6322-6328.

29. Feng, W.; Luo, H.; Wang, Y.; Zeng, S.; Deng, L.; Zhou, X.; Zhang, H.; Peng, S., Ti_3C_2 MXene: a promising microwave absorbing material. *RSC Adv.* **2018,** *8*, 2398-2403.

30. Zhao, X.; Liu, M.; Chen, Y.; Hou, B.; Zhang, N.; Chen, B.; Yang, N.; Chen, K.; Li, J.; An, L., Fabrication of layered Ti_3C_2 with an accordion-like structure as a potential cathode material for high performance lithium–sulfur batteries. *J. Mater. Chem. A* **2015,** *3*, 7870-7876.

31. Lian, P.; Dong, Y.; Wu, Z.-S.; Zheng, S.; Wang, X.; Wang, S.; Sun, C.; Qin, J.; Shi, X.; Bao, X., Alkalized Ti_3C_2 MXene nanoribbons with expanded interlayer spacing for high-capacity sodium and potassium ion batteries. *Nano Energy* **2017,** *40*, 1-8.

32. Dai, B.; Zhao, B.; Xie, X.; Su, T.; Fan, B.; Zhang, R.; Yang, R., Novel two-dimensional $Ti_3C_2T_x$ MXenes/nano-carbon sphere hybrids for high-performance microwave absorption. *J. Mater. Chem. C* **2018,** *6*, 5690-5697.

33. Zhu, X.; Liu, B.; Hou, H.; Huang, Z.; Zeinu, K. M.; Huang, L.; Yuan, X.; Guo, D.; Hu, J.; Yang, J., Alkaline intercalation of Ti_3C_2 MXene for simultaneous electrochemical detection of Cd (II), Pb (II), Cu (II) and Hg (II). *Electrochim. Acta* **2017,** *248*, 46-57.

34. Naguib, M.; Kurtoglu, M.; Presser, V.; Lu, J.; Niu, J.; Heon, M.; Hultman, L.; Gogotsi, Y.; Barsoum, M. W., Two-dimensional nanocrystals produced by exfoliation of Ti_3AlC_2. *Adv. Mater.* **2011,** *23*, 4248-4253.

35. Er, D.; Li, J.; Naguib, M.; Gogotsi, Y.; Shenoy, V. B., Ti_3C_2 MXene as a high capacity electrode material for metal (Li, Na, K, Ca) ion batteries. *ACS Appl. Mater. Inter.* **2014,** *6*, 11173-11179.

36. Li, G.; Tan, L.; Zhang, Y.; Wu, B.; Li, L., Highly Efficiently Delaminated Single-Layered MXene Nanosheets with Large Lateral Size. *Langmuir* **2017,** *33*, 9000-9006.

37. Maleski, K.; Mochalin, V. N.; Gogotsi, Y., Dispersions of Two-Dimensional Titanium Carbide MXene in Organic Solvents. *Chem. Mater.* **2017,** *29*, 1632-1640.

38. Williamson, G.; Hall, W., X-ray line broadening from filed aluminium and wolfram. *Acta Metall.* **1953,** *1*, 22-31.

39. Jiang, Y.; Wen, X.; Benda, A.; Sheng, R.; Ho-Baillie, A. W.; Huang, S.; Huang, F.; Cheng, Y.-B.; Green, M. A., Time-resolved fluorescence anisotropy study of organic lead halide perovskite. *Sol. Energy Mater. Sol. Cells* **2016,** *151*, 102-112.

40. Gao, L.; Wang, L.; Ding, X.; Zhao, E.; Yang, S.; Zhao, Y.; Li, Y.; Wang, S.; Ma, T., Incredible PCE enhancement induced by damaged perovskite layers: deeply understanding the working principle of additives in bulk heterojunction perovskite solar cells. *J. Mater. Chem. A* **2018,** *6*, 4365-4373.

41. Zhao, X.; Tao, L.; Li, H.; Huang, W.; Sun, P.; Liu, J.; Liu, S.; Sun, Q.; Cui, Z.; Sun, L., Efficient Planar Perovskite Solar Cells with Improved Fill Factor via Interface Engineering with Graphene. *Nano Lett.* **2018,** *18*, 2442-2449.

42. Li, S.-S.; Chang, C.-H.; Wang, Y.-C.; Lin, C.-W.; Wang, D.-Y.; Lin, J.-C.; Chen, C.-C.; Sheu, H.-S.; Chia, H.-C.; Wu, W.-R., Intermixing-seeded growth for high-performance planar heterojunction perovskite solar cells assisted by precursor-capped nanoparticles. *Energy Environ. Sci.* **2016,** *9*, 1282-1289.

43. Lan, C.; Zhao, S.; Zhang, C.; Liu, W.; Hayase, S.; Ma, T., Concentration gradient-controlled growth of large-grain $CH_3NH_3PbI_3$ films and enhanced photovoltaic performance of solar cells under ambient conditions. *CrystEngComm* **2016,** *18*, 9243-9251.

44. Xiao, Z.; Dong, Q.; Bi, C.; Shao, Y.; Yuan, Y.; Huang, J., Solvent annealing of perovskite-induced crystal growth for photovoltaic-device efficiency enhancement. *Adv. Mater.* **2014,** *26*, 6503-6509.

45. Kapil, G.; Ripolles, T. S.; Hamada, K.; Ogomi, Y.; Bessho, T.; Kinoshita, T.; Chantana, J.; Yoshino, K.; Shen, Q.; Toyoda, T., Highly efficient 17.6% tin-lead mixed perovskite solar cells realized through spike structure. *Nano Lett.* **2018,** *18*, 3600.

46. Bai, Y.; Meng, X.; Yang, S., Interface Engineering for Highly Efficient and Stable Planar p-i-n Perovskite Solar Cells. *Adv. Energy Mater.* **2018,** *8*, 1701883.

47. Tripathi, N.; Shirai, Y.; Yanagida, M.; Karen, A.; Miyano, K., Novel surface passivation technique for low-temperature solution-processed perovskite PV cells. *ACS Appl. Mater. Inter.* **2016,** *8*, 4644-4650.

48. Yu, J. C.; Hong, J. A.; Jung, E. D.; Kim, D. B.; Baek, S.-M.; Lee, S.; Cho, S.; Park, S. S.; Choi, K. J.; Song, M. H., Highly efficient and stable inverted perovskite solar cell employing PEDOT: GO composite layer as a hole transport layer. *Sci. Rep.* **2018,** *8*, 1070.

49. Dong, Q.; Wang, Z.; Zhang, K.; Yu, H.; Huang, P.; Liu, X.; Zhou, Y.; Chen, N.; Song, B., Easily accessible polymer additives for tuning the crystal-growth of perovskite thin-films for highly efficient solar cells. *Nanoscale* **2016,** *8*, 5552-5558.

50. Chen, Q.; Chen, L.; Ye, F.; Zhao, T.; Tang, F.; Rajagopal, A.; Jiang, Z.; Jiang, S.; Jen, A. K.-Y.; Xie, Y., Ag-incorporated organic–inorganic perovskite films and planar heterojunction solar cells. *Nano Lett.* **2017,** *17*, 3231-3237.

51. Kim, H.-S.; Park, N.-G., Parameters affecting I–V hysteresis of $CH_3NH_3PbI_3$ perovskite solar cells: effects of perovskite crystal size and mesoporous TiO2 layer. *J. Phys. Chem. Lett.* **2014,** *5*, 2927-2934.

52. Oga, H.; Saeki, A.; Ogomi, Y.; Hayase, S.; Seki, S., Improved understanding of the electronic and energetic landscapes of perovskite solar cells: high local charge carrier mobility, reduced recombination, and extremely shallow traps. *J. Am. Chem. Soc.* **2014,** *136*, 13818-13825.

53. Son, D.-Y.; Lee, J.-W.; Choi, Y. J.; Jang, I.-H.; Lee, S.; Yoo, P. J.; Shin, H.; Ahn, N.; Choi, M.; Kim, D., Self-formed grain boundary healing layer for highly efficient $CH_3NH_3PbI_3$ perovskite solar cells. *Nat. Energy* **2016,** *1*, 16081.

Chapter 4. Reducing the energy loss by interface passivation

4.1 Introduction

Perovskite solar cells (PSCs) have been attracting large attention in the recent years, leading to an achievable high efficiency of 23.3%.[1-2] The perovskite light absorber, in most highly efficiency PSCs, is composed of the organic cations (e.g., MA and FA) hybridizing with the lead halide frameworks, which promises perfect band gap and strong light absorption ability.[3-5] However, the thermal stability of these hybrid PSCs is an important issue to be addressed owing to the irreversible decomposition of the perovskite phase to lead iodide and organic molecules when exposure to heat stress at low temperature (80 °C).[6] Mixing the inorganic Caesium (Cs) with the MA and FA can improve the composition and structural tolerability to higher temperature (100 °C).[7] While the fundamental solution for the thermal endurance is to entirely replace the organic cations with a Cs cation. The inorganic PSCs with the formula of $CsPbX_3$ (X=I, Br) are attracting great attention due to their outstanding thermal stability (stable over 400 °C) and high-speed progression in their performance.[8-11]

Among the family of $CsPbX_3$, the $CsPbBr_3$ is the most stable one, but its large band gap (2.30 eV) leads to poor light absorbing ability.[12] The narrowest band gap $CsPbI_3$ possesses good light absorbing property but easily transforms to non-photoactive orthorhombic phase (yellow phase) at room temperature in air.[10, 13-14] Therefore, for balancing the band gap and the phase stability of $CsPbX_3$ perovskite materials, mixing I and Br is one of the best choices.[11] For example, $CsPbIBr_2$ is a good light absorber with a proper band gap of 2.0 eV and better phase stability at room temperature. However, the performance of the $CsPbIBr_2$ based PSCs is still low. One crucial factor is the open-circuit voltage (V_{oc}) owing to large energy losses (E_{loss}), which is defined as the energy loss between the bandgap of the perovskite materials and the device V_{oc} ($E_{loss}= E_g-eV_{oc}$).[8] For example, Yabing Qi et al. fabricated the all-inorganic $CsPbIBr_2$ based PSCs with carbon electrode and the V_{oc} is only 0.96 V (PCE=6.14%) with the E_{loss} of larger than 1.0 eV, which is much larger than that of the organic-inorganic PSCs (less than 0.5 eV).[15] Zhong Jin and co-workers also fabricated a similar device structure with the V_{oc} of 1.08 V.[16] Higher V_{oc} for $CsPbIBr_2$ based device of 1.227 V was achieved by Yibing Cheng et al., in which they utilized Spiro-OMeTAD

hole transporting materials (HTM) and Au electrode, and achieved a PCE of 8.02%.[17] Thus the E_{loss} must be reduced in order to further improve the performance of the inorganic PSCs. It has been proven that non-radiative recombination at the interface between the perovskite film and the electron selective layer (ESL) or HTM, is one of the major factors that induce E_{loss} of the device.[8] For instance, Qifan Xue et al. constructed SnO_2/ZnO bilayered ESL for $CsPbI_2Br$, which has successfully suppressed interfacial trap-assisted recombination and contributed to a high V_{oc} of 1.23 V and PCE of 14.6%.[8] Alex K.-Y. Jen and co-workers modified the SnO_2 film by C60 and the resultant V_{oc} and PCE of $CsPbIBr_2$ are 1.18 V and 7.34%, respectively.[18] Therefore, interface engineering is a very promising method to reduce the E_{loss}, and to increase V_{oc} for further enhancement of all-inorganic PSCs's performances.

Here we propose a simple interface engineering process for SnO_2 ESL surface passivation employing $SnCl_2$ solution. It shows that surface passivation leads to faster carrier transformation through the interface and larger charge recombination resistance for the $CsPbIBr_2$ PSCs. By employing the passivated SnO_2 ESL, a high V_{oc} of 1.31 V was recorded for the $CsPbIBr_2$ PSCs using the carbon as the counter electrode. The PCE was enhanced from 4.73 to 7.00 % after the passivation process. Our results indicate that surface passivation is a very promising method to reduce the E_{loss} for the all-inorganic PSCs.

4.2 Experimental Section

4.2.1 Device Fabrication

The 1.0 M $CsPbIBr_2$ perovskite solution was fromed by dissolving the CsI and $PbBr_2$ in DMSO with the mole ratio of 1/1, then stirring at 60 ^oC until the clear solution was obtained. The washing of ITO glass and the prepration of SnO_2 film is the same with that in Chapter 3. For passivation, the $SnCl_2$ solution (the concentration varies from 0.05 M to 0.15 M) was deposited on the SnO_2 nanoparticles film (NPs) and baked at 100 ^oC for 10min and 180 ^oC for 1 hour. Subsequently, in the nitrogen-filled glove box, the perovskite precursor solution was deposited on the SnO_2 layer via a spin-coating program at 1000 rpm for 10s and then 3000 rpm for 30 s. After the spin-coating process, the obtained film was placed for 5 min and then annealed at 160 ^oC for 10 min on a hot plate in the glove box. For completing the device, the carbon electrode was deposited on the top of the $CsPbIBr_2$ film by doctor-blading technology using scotch tape to control

the electrode thickness. Then the cells were heated treated at 100 °C for 10 min in ambient conditions to promote evaporation of residual solvents.

4.2.2 Characterizations

The characterization methods including XRD, SEM, UV-Vis spectra, EIS and J-V curve were introduced in Chapter 2. In addition, the AFM images were measured by Surface Probe Microscopy (SPM, JSPM-5200, JEOL).

4.3 Results and discussion

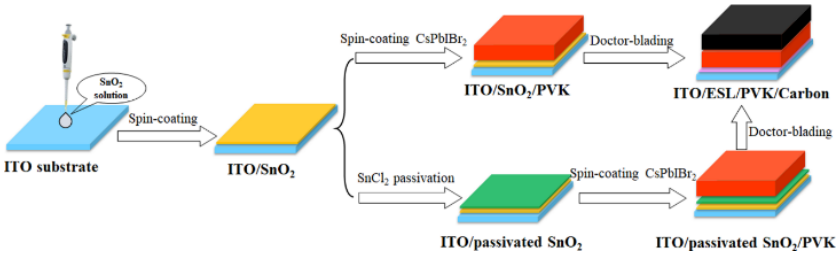

Figure 1 Fabrication process of all-inorganic PSCs with bare or passivated SnO_2 ESL.

Figure 1 shows the fabrication process of the all-inorganic PSCs where the bare and passivated SnO_2 were used as the ESL (The details are depicted in Experiment Section in supplementary information). Firstly, we spin-coated the SnO_2 colloid (tin (IV) oxide) solution to form the SnO_2 film. The ultra-thin passivation SnO_2 layer was prepared by spin-coating 0.1 M $SnCl_2$ precursor on the prepared SnO_2 at 6000 rpm followed by an annealing process at 180 ºC for 1 h.

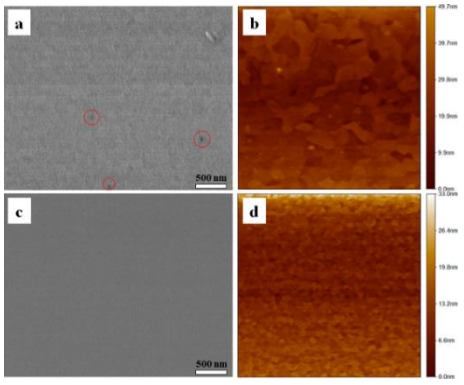

Figure 2 Top-view SEM images of (a) bare and (c) passivated SnO_2 films; AFM images of the (b) bare and (d) passivated SnO_2 films.

Figure 2 shows the SEM images and AFM images of the SnO_2 film before and after passivation. From Figure 2a and c, we can confirm that the introduction of ultra-thin passivation SnO_2 layer induces a significant difference in the film morphology. Several prominent holes are observed from the SnO_2 film (red-circled), implying an imperfect coverage property, which will lead to severe recombination during the charge extraction from the perovskite film. While, with an ultra-thin passivation SnO_2 layer, the holes are filled; this forms a hole-free ESL. We also compared them by AFM images as shown in Figure 2b and d. The SnO_2 film becomes much smoother after passivated by $SnCl_2$. Specifically, the root-square-roughness (Rq) is dramatically decreased from 7.05 nm to 4.21 nm, which implies the effect of passivation.

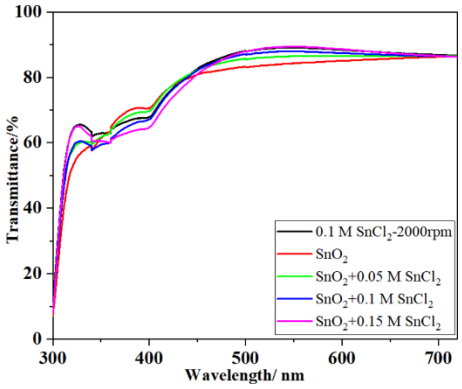

Figure 3 Transmission spectra of different SnO_2 films on ITO substrate.

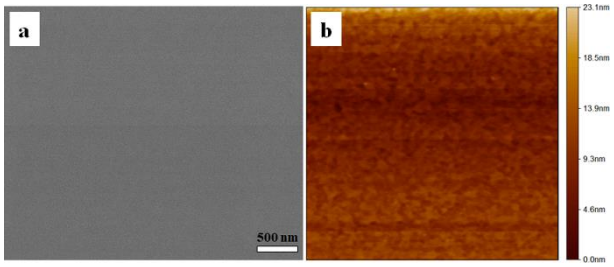

Figure 4 (a) SEM and (b) AFM image of SnO_2 film passivated with 0.15 M $SnCl_2$ solution.

The effect of passivated or non-passivated is also presented in Figure 3, as observed through their transmittance properties. Comparing with the bare SnO_2 film, the films passivated by $SnCl_2$ with different concentrations display higher transmittance properties in the visible light region. This phenomenon is attributed to the formation of the smoother surface, which leads to lower reflectivity and higher transmittance.[19] The SnO_2 film passivated with 0.15 M $SnCl_2$ has the highest transmittance because of its smoother surface and lower Rq of 2.99 nm (Figure 4). The

smoother surface is resulted from the passivation effect rather than annealing at a higher temperature of 180 ºC, as shown in Figure 5.

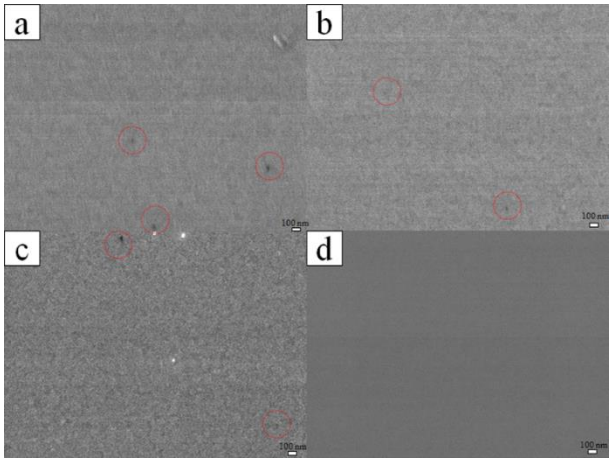

Figure 5 SEM images of SnO_2 nanocrystal films: (a) annealed at 150 ºC for 30 min, (b) annealed at 150 ºC for 30 min and then 180 ºC for 1 h, (c) annealed at 180 ºC for 1 h; and (d) $SnCl_2$ passivated film annealed at 180 ºC for 1 h.

We conducted the control experiments to confirm the effect of 180 ºC annealing on the roughness of the resultant SnO_2 nanocrystal films. The spin-coated SnO_2 nanocrystal films with different annealing processes are shown in Figure 5. We can find that there is no obvious difference for annealing at 180 ºC for 1 h after annealing at 150 ºC for 30 min. While directly annealing the spin-coated SnO_2 nanocrystal film at 180 ºC for 1 h results a rougher film, which might be attributed to that higher annealing temperature will lead to aggregation of the nanocrystals. While after passivation using $SnCl_2$-ethanol solution, a much smoother film can be obtained (Figure 5d). So the 180 ºC annealing is not the decisive factor for getting smooth SnO_2 film.

In order to investigate the effect of SnO_2 film passivation on the performance of the devices, we fabricated an inorganic $CsPbIBr_2$ perovskite film on bare and passivated SnO_2 film, respectively. The fabrication process is shown in Figure 1 and what should be noted is that the inorganic $CsPbIBr_2$ film was annealed at a relatively low temperature of 160 ºC, rather than the widely used temperature of around 300 ºC in previous publications.

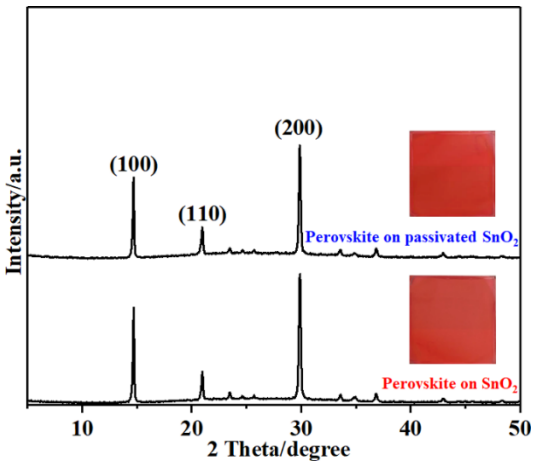

Figure 6 XRD patterns of $CsPbIBr_2$ perovskite film deposited on bare or passivated SnO_2 ESL. Inset: photographs of the respective perovskite film.

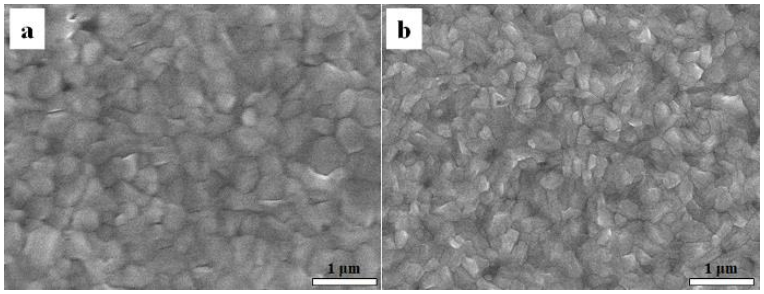

Figure 7 SEM images of $CsPbIBr_2$ film deposited on bare or passivated SnO_2 ESL.

Figure 6 shows the X-ray diffraction (XRD) patterns of the $CsPbIBr_2$ films on different ESLs and the insets illustrate the photographs of the prepared $CsPbIBr_2$ film. From the XRD patterns, we found that both the films show similar strong peaks at 14.7°, 20.9°, 29.9°, corresponding to (100), (110), and (200) crystal planes of the $CsPbIBr_2$ cubic perovskite structure, respectively.[20-22] Moreover, as shown in Figure 7, both the $CsPbIBr_2$ films display similar surface morphologies, but the film on passivated SnO_2 seems a little denser with higher coverage owing to the smoother surface of ESL, which is a beneficial criterion to form a high-quality perovskite layer.[23] The effects of SnO_2 passivation on the cell performance are further investigated by fabricating PSCs with the architecture of ITO/ESL/$CsPbIBr_2$/Carbon, as depicted in Figure 1, in which the ESL is bare SnO_2 or passivated SnO_2 film.

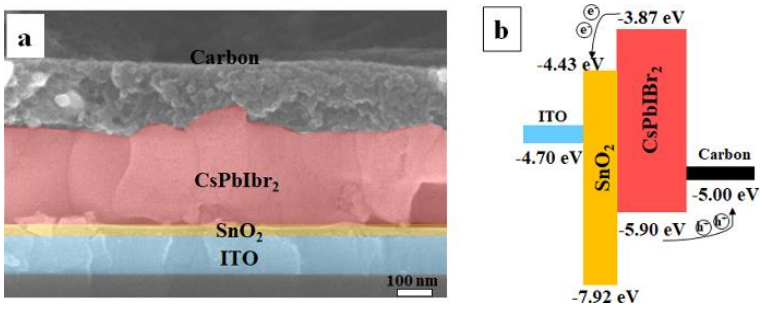

Figure 8 (a) Cross-section SEM image and (b) energy diagram of the components of the all-inorganic $CsPbIBr_2$ PSCs.

Figure 8a shows the cross-section SEM image with passivated SnO_2 ESL and the thickness of the perovskite layer is about 260 nm, which is similar to those of previous reports.[15-16, 18] Therefore, we confirm that through the processes depicted in Figure 1, the above architecture was successfully fabricated. Moreover, the band alignment diagram of the components (Figure 8b), determined from Figure 9, illustrates that the light-generated electrons and holes can be effectively transferred from the perovskite absorber to the ESL and the HTM, respectively, implying perfect matching in energy levels for this device configuration.

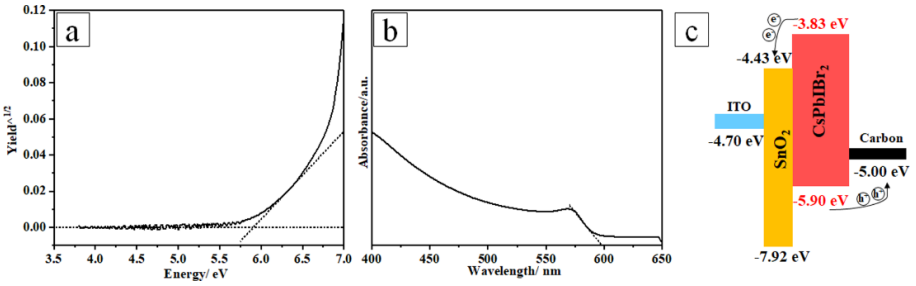

Figure 9 (a) The photoelectron yield spectroscopy, (b) UV-vis spectrum of $CsPbIBr_2$ film and (c) the energy levels of the components.

From Figure 9a, we can see that the valence band of $CsPbIBr_2$ is -5.90 eV. Figure 9b indicates that the absorption band edge is about 598 nm, thus the band gap of $CsPbIBr_2$ is 2.07 eV. From these two spectra, the energy level of the perovskite material can be depicted as Figure 9c, where the SnO_2 ESL can effectively transfer the photo-generated electrons and block the holes.

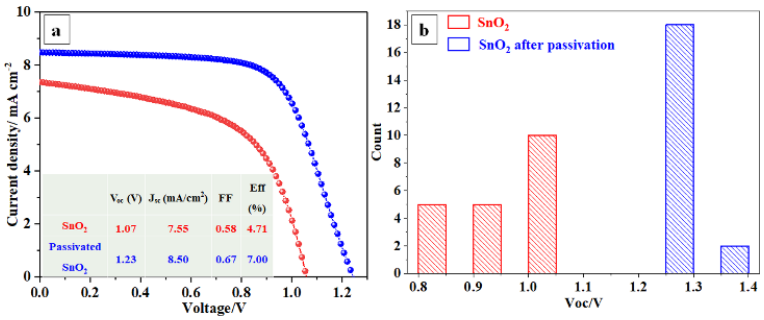

Figure 10 (a) *J-V* curves of the champion PSCs based on bare or passivated SnO_2 ESL (inset table is the photovoltaic parameters); (b) V_{oc} distributions of two type PSCs (20 cells for each).

Figure 10a displays the *J-V* curves of the champion $CsPbIBr_2$ PSCs with different ESLs and their parameters are shown as the inset in Figure 10a. Obviously, the passivated SnO_2 based device is outperforming the bare SnO_2. The V_{oc}, J_{sc} and FF of the passivated SnO_2 based device are 1.23 V, 8.50 mA cm^{-2} and 0.67, respectively, resulting a high PCE of 7.00 %, with 0.16 V and 48.6% enhancement in V_{oc} and PCE when comparing with the bare SnO_2 based device (1.07 V and 4.73 %).

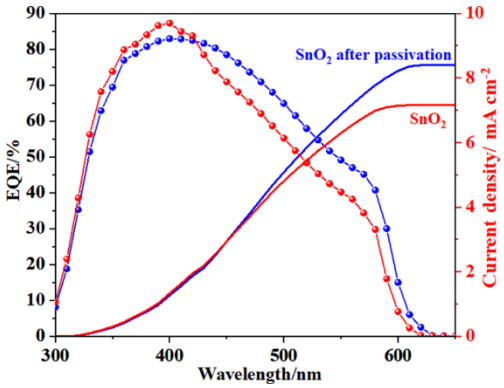

Figure 11 IPCE spectra of $CsPbIBr_2$ PSCs based on bare or passivated SnO_2 ESL.

All the measured J_{sc} in our experiments well matches the photocurrent density calculated from the IPCE spectra (Figure 11). The higher J_{sc} might be partly attributed to the denser light absorber layer because of its stronger light absorption ability. While the bare SnO_2 based PSC has a little higher EQE values than those of the passivated one in the range of 300-400 nm, which is because of the better transmittance property of the bare SnO_2 film in this range, as shown in the transmittance spectra of different SnO_2 films (Figure 3).

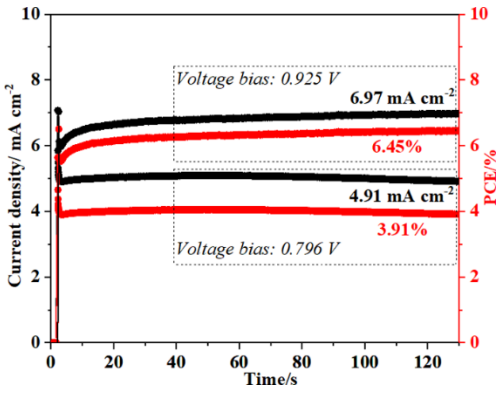

Figure 12 Stability of output of $CsPbIBr_2$ PSCs based on bare or passivated SnO_2 ESL.

The stability output of the champion cells is measured in ambient air, in which the bias voltage is set at their respective maximum power points. As displayed in Figure 12, the stabilized PCE of the passivated SnO_2 based device is estimated to be 6.45% after 130s continuous measurement, which is higher than that of the bare SnO_2 based device of 3.91%. At the same time, the passivated SnO_2 based device has a slight increase in PCE, while a slight decrease for the bare SnO_2 based device. This indicates the better output stability for the device with passivated SnO_2 as ESL. We summarized the performances of the $CsPbIBr_2$ based PSCs with carbon or Au electrode reported to date, as shown in Table 1. We found that the champion PCE (7.00 %) obtained for a passivated SnO_2 based solar cell in this work is comparable to those of the literature.

Table 1 Summary of V_{oc} and PCE values for reported $CsPbIBr_2$-based solar cells under the reverse scanning direction.

Method	Temperature/ °C	Device structure	Champion V_{oc}/V	Champion PCE/%	Ref.
One-step spin-coating	160	FTO/SnO_2/$CsPbIBr_2$/Carbon	1.31	7.00	This work
Spray-Assisted Deposition	300	FTO/c-TiO_2/m-TiO_2/$CsPbIBr_2$/Spiro-OMeTAD/Au	1.13	6.30	1
Thermal Evaporation	250	FTO/c-TiO_2/$CsPbIBr_2$/Au	0.96	4.70	2
Two-step dipping	135	FTO/NiO_x/$CsPbIBr_2$/ZnO/Al	1.01	5.57	3
Two-step dipping	350	FTO/c-TiO_2/m-TiO_2/$CsPbIBr_2$/Carbon	0.96	6.14	4
Two-step dipping	350	FTO/c-TiO_2/m-TiO_2/$CsPbIBr_2$/Carbon	1.08	8.25	5
One-step spin-coating	320	FTO/c-TiO_2/$CsPbIBr_2$/Spiro-OMeTAD/Au	1.23	8.02	6
One-step spin-coating	160	FTO/NiO_x/$CsPbIBr_2$/MoO_x/Au	0.85	5.52	7
One-step spin-coating	100	FTO/c-TiO_2/$CsPbIBr_2$/Carbon	1.14	6.55	8
One-step spin-coating	150	FTO/SnO_2/C60/$CsPbIBr_2$/Spiro-OMeTAD/Au	1.18	7.34	9
One-step spin-coating	280	FTO/c-TiO_2/$CsPbIBr_2$/Carbon	1.245	9.16	10

In order to verify the reproducibility of the high-performance passivated SnO_2 based PSCs, we fabricated 20 pieces of bare SnO_2 and passivated SnO_2 ESL-based solar cells, respectively, as

listed in Table 2. We found that the PCEs of the most passivated SnO_2 based devices are in the range of 5.27 to 7.00 %, while all the bare SnO_2 based cells show PCEs lower than 4.71 %. Whilst, all the V_{oc} of the passivated SnO_2 based cells is above 1.20 V while the V_{oc} of the bare SnO_2 based devices distributed in the range from 0.85 to 1.07 V. The V_{oc} distributions of the PSCs on bare and passivated SnO_2 are shown in Figure 10b. We can see that our passivation method is highly reproducible in achieving high V_{oc}. More importantly, the highest V_{oc} of 1.31 V was achieved after SnO_2 surface passivation, which is higher than other reported $CsPbIBr_2$ PSCs (Table 1) and is one of the highest V_{oc} obtained for inorganic $CsPbX_3$ PSCs. Therefore, we can conclude that the passivation of SnO_2 ESL with the ultra-thin SnO_2 film is a promising approach to reduce E_{loss} for $CsPbIBr_2$ PSCs.

Table 2 Performances of 20 devices based on bare or passivated SnO_2 ESL under reverse scanning direction.

SnO_2					SnO_2 after passivation				
Sample No.	V_{oc}(V)	J_{sc}(mA/cm²)	FF	Eff/%	Sample No.	V_{oc}(V)	J_{sc}(mA/cm²)	FF	Eff/%
1	1.07	7.55	0.58	4.71	21	1.23	8.50	0.67	7.00
2	1.07	7.57	0.52	4.21	22	1.22	8.61	0.66	6.95
3	1.06	7.58	0.52	4.14	23	1.22	8.66	0.65	6.87
4	1.01	8.07	0.51	4.13	24	1.22	8.64	0.65	6.87
5	1.06	7.59	0.51	4.10	25	1.21	8.80	0.63	6.72
6	1.01	7.51	0.54	4.07	26	1.21	8.60	0.64	6.62
7	1.00	8.07	0.50	4.07	27	1.22	8.62	0.63	6.61
8	0.99	8.09	0.50	4.03	28	1.22	8.39	0.65	6.61
9	1.03	7.53	0.51	3.99	29	1.21	8.49	0.63	6.46
10	1.03	7.55	0.50	3.89	30	1.22	8.70	0.62	6.58
11	1.02	7.92	0.48	3.88	31	1.22	8.36	0.61	6.24
12	0.98	7.96	0.48	3.76	32	1.20	8.18	0.63	6.21
13	0.91	7.48	0.50	3.42	33	1.22	7.51	0.62	5.68
14	0.95	7.04	0.50	3.35	34	1.25	7.43	0.60	5.59
15	0.94	7.09	0.49	3.27	35	1.23	7.44	0.61	5.55
16	0.89	7.65	0.43	2.93	36	1.22	7.45	0.58	5.27
17	0.88	7.71	0.42	2.86	37	1.27	6.87	0.44	3.87
18	0.89	7.38	0.41	2.73	38	1.26	6.29	0.38	3.01
19	0.89	7.34	0.41	2.71	39	1.31	6.86	0.33	3.00
20	0.85	7.71	0.40	2.63	40	1.31	5.70	0.28	2.06

To completely understand the passivation effect of the SnO_2 film, the various concentration of $SnCl_2$ solution were studied. It shows that too low concentration of $SnCl_2$ is ineffective in passivating the SnO_2 film as proven through its non-obvious enhancement in the performance (Figure 13 and Table 3). In contrast, a thicker SnO_2 passivation layer (high concentration) increases the series resistance of the device. We also prepared a single SnO_2 layer on ITO using 0.1 M $SnCl_2$ precursor with the spin-coating speed of 2000 rpm. We found that its performance is compromised, as compared to the bare SnO_2 ESL based device (Figure 13 and Table 3). Thus, the

reason for the reduced E_{loss} and enhanced performance of the passivated SnO_2 based solar cells lies in the interface modification, rather than the difference between the SnO_2 films prepared from SnO_2 colloid solution or $SnCl_2$ precursor.[8, 27-28]

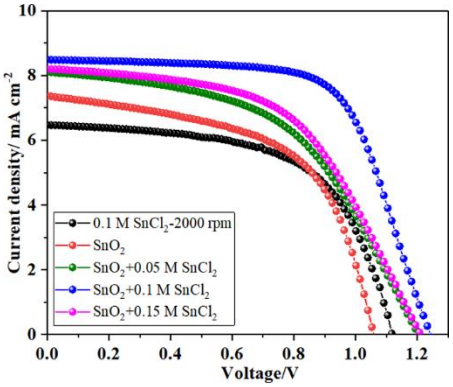

Figure 13 *J-V* curves of the PSCs based on different SnO_2 ESLs.

Table 3 Photovoltaic parameters of PSCs based on different SnO_2 ESLs.

Device	V_{oc}(V)	J_{sc}(mA/cm^2)	FF	PCE/%
0.1 M $SnCl_2$-2000 rpm	1.12	6.47	0.59	4.30
SnO_2	1.07	7.55	0.58	4.71
SnO_2+0.05 M $SnCl_2$	1.19	8.11	0.51	4.97
SnO_2+0.1 M $SnCl_2$	1.23	8.50	0.67	7.00
SnO_2+0.15 M $SnCl_2$	1.21	8.20	0.53	5.29

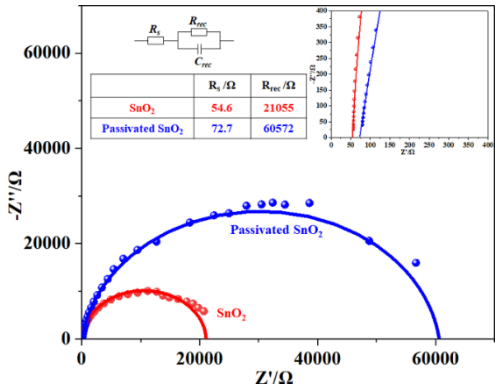

Figure 14 Nyquist plots of PSCs based on bare or passivated SnO_2 in dark condition at a voltage of V_{oc}. Inset: the equivalent circuit, the enlarged high-frequency region, and table of simulated results.

The EIS measurements were made to investigate the interfacial charge transfer properties in the PSCs with SnO_2 ESL with or without passivation, as shown in Figure 14. Generally, the high-frequency arc is related to the charge transporting and the arc at the low-frequency region represents the recombination resistance at perovskite/SnO_2 and perovskite/carbon interface.[28-29] It is clear that the device with passivated SnO_2 ESL shows larger R_{rec} (60572 Ω) than that of bare SnO_2 ESL based device (21055 Ω), which means that the recombination in the former device is highly suppressed. Simultaneously, the former has a larger series resistance (R_s) than that of the latter owing to its thicker SnO_2 film.

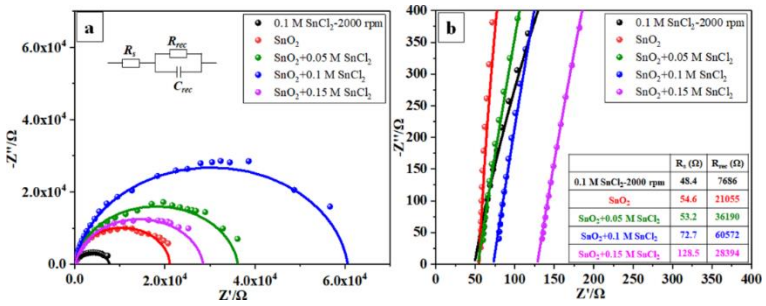

Figure 15 (a) Nyquist plots and (b) enlarged high-frequency region of PSCs different SnO_2 ESLs in dark condition at a voltage of V_{oc}. Inset: the equivalent circuit and table of simulated results.

We also measured the EIS of other devices with different ESLs, as shown in Figure S15. We found that after passivation, the devices possess larger R_{rec} than that of the bare SnO_2 based device and the 0.1 M $SnCl_2$ passivation leads to highest R_{rec} (summarized in the table inset in Figure 15), thus contributed for the best performance. While the device using SnO_2 ESL prepared by spin-coating 0.1 M $SnCl_2$ at 2000 rpm shows the smallest R_{rec}. In brief, this surface passivation decreases the recombination process at the interface between the perovskite and the ESL, which significantly improves the V_{oc} and PCE of the devices.

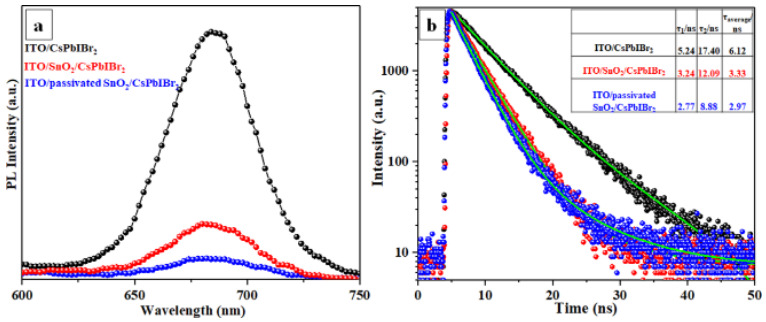

Figure 16 (a) Steady-state photoluminescence (PL) spectra and (b) normalized transient PL decay profiles for $CsPbIBr_2$, bare $SnO_2/CsPbIBr_2$, and passivated $SnO_2/CsPbIBr_2$.

Then the PL and TRPL measurements of the perovskite film on different substrates were conducted. Figure 16a shows the PL spectra of ITO/$CsPbIBr_2$, ITO/SnO_2/$CsPbIBr_2$ and ITO/passivated SnO_2/$CsPbIBr_2$ samples. The ITO/$CsPbIBr_2$ displays high PL intensity, which implies serious carrier recombination.[8] The ITO/ passivated SnO_2 /$CsPbIBr_2$ sample shows lower PL intensity than that of the ITO/SnO_2/$CsPbIBr_2$ sample, indicating stronger electron extraction ability from the perovskite film and lower recombination possibility.[30] Figure 16b shows the TRPL spectra and the corresponding decay time is calculated via the exponential fits of the spectra. The parameters are listed in the table inserted in Figure 16b. As shown in the table, when the $CsPbIBr_2$ is deposited on the bare ITO substrate, the PL decay times are 5.24 and 17.40 ns for τ_1 and τ_2, respectively. While the ITO/SnO_2/$CsPbIBr_2$ sample possesses the reduced PL decay time of 3.24 and 12.09 ns for τ_1 and τ_2, respectively. When the passivated SnO_2 ESL was used for the perovskite film deposition, both the τ_1 and τ_2 are further reduced to 2.77 and 8.88 ns, respectively. Moreover, the $CsPbIBr_2$ film on the passivated SnO_2 ESL has the smallest average decay time among the three samples. Thus the passivation of SnO_2 ESL can accelerate the electron injection process from the light absorber film and suppress the carrier recombination at the perovskite/ESL interface, leading to higher V_{oc} and better performance.

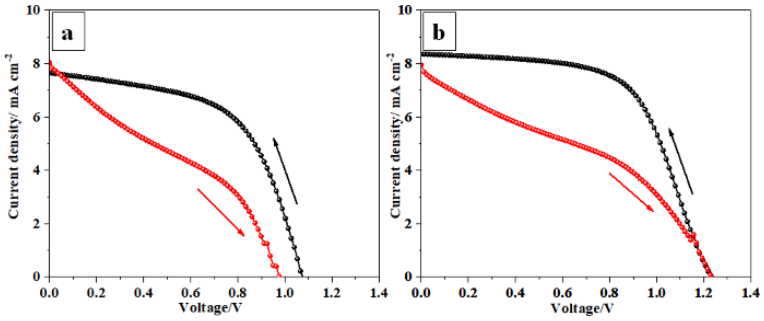

Figure 17 J-V curves with the reverse and forward scanning direction for the PSCs based on (a) bare and (b) passivated SnO_2 ESL.

Table 4 Photovoltaic parameters of J-V curves with the reverse and forward scanning direction for the PSCs based on bare and passivated SnO_2 ESL.

ESL	Scanning type	V_{oc}(V)	J_{sc}(mA/cm^2)	FF	PCE/%	Hysteresis Index
SnO_2	Forward	0.98	8.04	0.34	2.66	43.0%
	Reverse	1.07	7.65	0.57	4.67	
Passivated SnO_2	Forward	1.23	7.96	0.37	3.60	42.3%
	Reverse	1.22	8.36	0.61	6.24	

Figure 17 and Table 4 displays the hysteresis properties of both SnO_2 and passivated SnO_2 based $CsPbIBr_2$ PSCs. We found that both kinds of devices have severe hysteresis if compare with the organic-inorganic hybrid PSCs. The hysteresis index for the SnO_2 and passivated SnO_2 based device are 43% and 42.3%, respectively. Yibing Cheng and co-workers have explained this phenomenon by pointing out that there is iodide-rich phase segregation, mainly existing at the grain boundaries, forming clusters in $CsPbIBr_2$ film, which heavily affects the ion migration.[17] This phenomenon exacerbates the hysteresis in $CsPbIBr_2$ PSCs. On the other hand, the relative small grains size with a large number of grain boundaries and compositional defects accompanying with one-step solution fabrication method might be other reasons for the severe hysteresis properties.[9, 31]

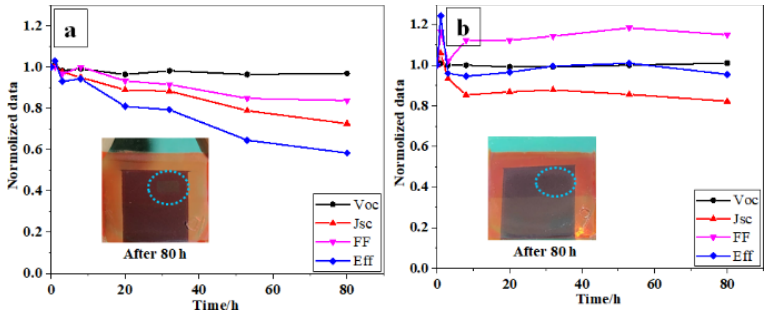

Figure 18 Normalized photovoltaic parameters of the (a) bare and (b) passivated SnO_2 ESL based unencapsulated $CsPbIBr_2$ PSCs under continuously heating at 90 °C in air with the humility of 60-70%. Inset are the photographs of the two kinds of PSCs after heating for 80 hours.

It has been widely accepted that the degradation of perovskite occurs at the interface between the ESL and the perovskite materials.[32-33] In order to investigate the effect of SnO_2 surface passivation on the device stability, we measured the thermal stability of the unencapsulated solar cells at 90 °C in the air with the relative humidity of 60-70 %. The time-dependent normalized V_{oc}, J_{sc}, FF, and PCE of the two type devices are shown in Figure 18. It shows that the passivated SnO_2 based device has better durability than that of the bare SnO_2 based device. All the parameters of

the two solar cells increase over the first one hour, which is recognized as interfacial ripening process with better charge transferability and improved crystallinity of the perovskite materials.[16, 34] During the subsequent tens of hours, the FF of the passivated SnO_2 based device kept at a higher level than the initial value, while the J_{sc} decreases obviously relative to the initial value. After 80 hours, the passivated device could still maintain 95.5% of its initial performance, which is much higher than that of the bare SnO_2 based device (58.3%). Moreover, we found that after long hours of light exposure, the appearance of the active area of the bare SnO_2 changes when viewing from the back side, as shown in Figure 18a (inset), while this phenomenon was not observable for the passivated SnO_2 based device. Thus there should be some undesired photochemical reactions at the bare SnO_2/perovskite interface, such as the light and interface defects-induced halide migration in the $CsPbIBr_2$ film, that impede the high performance.[35-36] Hence the SnO_2 surface modification can help to avoid the photochemical reactions and improve the thermal stability of inorganic PSCs.

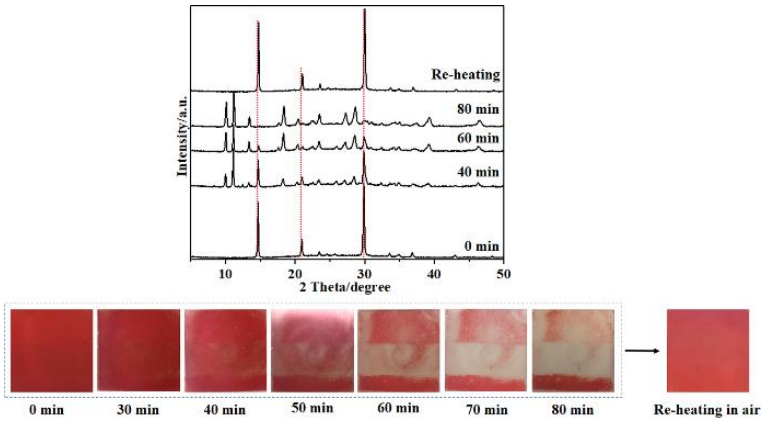

Figure 19 Time-dependent XRD patterns and photographs of the passivated SnO_2 based $CsPbIBr_2$ film when exposed to air at 25 °C with the humidity of 65%.

Moreover, we studied the room-temperature phase stability of the $CsPbIBr_2$ perovskite materials. The measurements were carried out at 25 °C in the air at a relative humidity of 65 %. The results of the $CsPbIBr_2$ deposited on the passivated SnO_2 film are shown in Figure 19. It shows that $CsPbIBr_2$ is very unstable where the film changed from red to transparent quickly within 80 min. From the time-dependent XRD patterns of the sample, we observed that the phase changes from the photo-active α phase to non-photoactive δ phase after 80 min.[10] There is no obvious difference in phase stability for the perovskite film deposited on SnO_2 ESL with or without passivation at room temperature because the phase transition is mainly caused by water. While

after the re-heating process in air, the transparent film re-transformed to red color film, meaning reversible phase transition property, which is in accordance with Peidong Yang's research.[25] Therefore, the room-temperature phase stability of $CsPbX_3$ perovskite materials, especially for the halide-rich phases, is one of the most important aspects that require prompt addresses.

4.4 Conclusions

In conclusion, our work has demonstrated an efficient interface engineering method of SnO_2 ESL passivation, which aims to reduce the energy loss of the all-inorganic Cs-based PSCs. We found that the passivation of SnO_2 not merely effectively decreases the recombination process at the interface between the $CsPbIBr_2$ perovskite and the SnO_2, but also accelerates the electron extraction efficiency from the perovskite film. After passivation, the performance was improved and a high V_{oc} of 1.31 V was obtained. The thermal stability of the passivated SnO_2 based devices highly outperformed the bare SnO_2 based solar cells. This work has proven that energy loss occurred in all-inorganic PSCs can be overcome through interface engineering. We believe that this method is highly applicable to other PSCs for decreasing the E_{loss}.

References

1. Kojima, A.; Teshima, K.; Shirai, Y.; Miyasaka, T., Organometal halide perovskites as visible-light sensitizers for photovoltaic cells. *J. Am. Chem. Soc.* **2009,** *131* (17), 6050-6051.

2. https://www.nrel.gov/pv/assets/pdfs/pv-efficiency-chart.20190103.pdf.

3. Petrus, M. L.; Schlipf, J.; Li, C.; Gujar, T. P.; Giesbrecht, N.; Müller-Buschbaum, P.; Thelakkat, M.; Bein, T.; Hüttner, S.; Docampo, P., Capturing the Sun: A Review of the Challenges and Perspectives of Perovskite Solar Cells. *Adv. Energy Mater.* **2018,** *8* (2), 1703396.

4. Jiang, Q.; Chu, Z.; Wang, P.; Yang, X.; Liu, H.; Wang, Y.; Yin, Z.; Wu, J.; Zhang, X.; You, J., Planar-Structure Perovskite Solar Cells with Efficiency beyond 21%. *Adv. Mater.* **2017,** *29* (46), 1703852.

5. Jeon, N. J.; Na, H.; Jung, E. H.; Yang, T.-Y.; Lee, Y. G.; Kim, G.; Shin, H.-W.; Seok, S. I.; Lee, J.; Seo, J., A fluorene-terminated hole-transporting material for highly efficient and stable perovskite solar cells. *Nat. Energy* **2018,** *3* (8), 682.

6. Kim, N.-K.; Min, Y. H.; Noh, S.; Cho, E.; Jeong, G.; Joo, M.; Ahn, S.-W.; Lee, J. S.; Kim, S.; Ihm, K., Investigation of Thermally Induced Degradation in $CH_3NH_3PbI_3$ Perovskite Solar Cells Using In-Situ Synchrotron Radiation Analysis. *Sci. Rep.* **2017,** *7* (1), 4645.

7. Zhou, G.; Wu, J.; Zhao, Y.; Li, Y.; Shi, J.; Li, Y.; Wu, H.; Li, D.; Luo, Y.; Meng, Q., Application of Cesium on the Restriction of Precursor Crystallization for Highly Reproducible Perovskite Solar Cells Exceeding 20% Efficiency. *ACS Appl. Mater. Inter.* **2018,** *10* (11), 9503-9513.

8. Yan, L.; Xue, Q.; Liu, M.; Zhu, Z.; Tian, J.; Li, Z.; Chen, Z.; Chen, Z.; Yan, H.; Yip, H. L., Interface Engineering for All-Inorganic CsPbI2Br Perovskite Solar Cells with Efficiency over 14%. *Adv. Mater.* **2018,** *30* (33), 1802509.

9. Zhu, W.; Zhang, Q.; Chen, D.; Zhang, Z.; Lin, Z.; Chang, J.; Zhang, J.; Zhang, C.; Hao, Y., Intermolecular Exchange Boosts Efficiency of Air-Stable, Carbon-Based All-Inorganic Planar CsPbIBr2 Perovskite Solar Cells to Over 9%. *Adv. Energy Mater.* **2018**, 1802080.

10. Wang, P.; Zhang, X.; Zhou, Y.; Jiang, Q.; Ye, Q.; Chu, Z.; Li, X.; Yang, X.; Yin, Z.; You, J., Solvent-controlled growth of inorganic perovskite films in dry environment for efficient and stable solar cells. *Nat. Commun.* **2018,** *9* (1), 2225.

11. Bian, H.; Bai, D.; Jin, Z.; Wang, K.; Liang, L.; Wang, H.; Zhang, J.; Wang, Q.; Liu, S. F., Graded Bandgap CsPbI2+ xBr1− x Perovskite Solar Cells with a Stabilized Efficiency of 14.4%. *Joule* **2018,** *2* (8), 1500-1510.

12. Duan, J.; Zhao, Y.; He, B.; Tang, Q., Simplified Perovskite Solar Cell with 4.1% Efficiency Employing Inorganic CsPbBr3 as Light Absorber. *Small* **2018,** *14* (20), 1704443.

13. Wang, Y.; Zhang, T.; Kan, M.; Zhao, Y., Bifunctional Stabilization of All-Inorganic α-CsPbI3 Perovskite for 17% Efficiency Photovoltaics. *J. Am. Chem. Soc.* **2018,** *140* (39), 12345-12348.

14. Eperon, G. E.; Paterno, G. M.; Sutton, R. J.; Zampetti, A.; Haghighirad, A. A.; Cacialli, F.; Snaith, H. J., Inorganic caesium lead iodide perovskite solar cells. *J. Mater. Chem. A* **2015,** *3* (39), 19688-19695.

15. Liang, J.; Liu, Z.; Qiu, L.; Hawash, Z.; Meng, L.; Wu, Z.; Jiang, Y.; Ono, L. K.; Qi, Y., Enhancing Optical, Electronic, Crystalline, and Morphological Properties of Cesium Lead Halide

by Mn Substitution for High-Stability All-Inorganic Perovskite Solar Cells with Carbon Electrodes. *Adv. Energy Mater.* **2018**, 1800504.

16. Liang, J.; Zhao, P.; Wang, C.; Wang, Y.; Hu, Y.; Zhu, G.; Ma, L.; Liu, J.; Jin, Z., CsPb0. 9Sn0. 1IBr2 based all-inorganic perovskite solar cells with exceptional efficiency and stability. *J. Am. Chem. Soc.* **2017,** *139* (40), 14009-14012.

17. Li, W.; Rothmann, M. U.; Liu, A.; Wang, Z.; Zhang, Y.; Pascoe, A. R.; Lu, J.; Jiang, L.; Chen, Y.; Huang, F., Phase segregation enhanced ion movement in efficient inorganic $CsPbIBr_2$ solar cells. *Adv. Energy Mater.* **2017,** *7* (20), 1700946.

18. Li, N.; Zhu, Z.; Li, J.; Jen, A. K. Y.; Wang, L., Inorganic $CsPb_{1-x}Sn_xIBr_2$ for Efficient Wide-Bandgap Perovskite Solar Cells. *Adv. Energy Mater.* **2018**, 1800525.

19. Yang, G.; Lei, H.; Tao, H.; Zheng, X.; Ma, J.; Liu, Q.; Ke, W.; Chen, Z.; Xiong, L.; Qin, P., *Small* **2017,** *13* (2), 1601769.

20. Liu, C.; Li, W.; Chen, J.; Fan, J.; Mai, Y.; Schropp, R. E., Ultra-thin MoOx as cathode buffer layer for the improvement of all-inorganic CsPbIBr2 perovskite solar cells. *Nano Energy* **2017,** *41*, 75-83.

21. Ma, Q.; Huang, S.; Wen, X.; Green, M. A.; Ho-Baillie, A. W., Hole transport layer free inorganic CsPbIBr2 perovskite solar cell by dual source thermal evaporation. *Adv. Energy Mater.* **2016,** *6* (7), 1502202.

22. Sutton, R. J.; Eperon, G. E.; Miranda, L.; Parrott, E. S.; Kamino, B. A.; Patel, J. B.; Hörantner, M. T.; Johnston, M. B.; Haghighirad, A. A.; Moore, D. T., Bandgap-tunable cesium lead halide perovskites with high thermal stability for efficient solar cells. *Adv. Energy Mater.* **2016,** *6* (8), 1502458.

23. Ren, X.; Yang, D.; Yang, Z.; Feng, J.; Zhu, X.; Niu, J.; Liu, Y.; Zhao, W.; Liu, S. F., Solution-processed Nb: SnO2 electron transport layer for efficient planar perovskite solar cells. *ACS Appl. Mater. Inter.* **2017,** *9* (3), 2421-2429.

24. Lau, C. F. J.; Deng, X.; Ma, Q.; Zheng, J.; Yun, J. S.; Green, M. A.; Huang, S.; Ho-Baillie, A. W., CsPbIBr2 perovskite solar cell by spray-assisted deposition. *ACS Energy Lett.* **2016,** *1* (3), 573-577.

25. Lin, J.; Lai, M.; Dou, L.; Kley, C. S.; Chen, H.; Peng, F.; Sun, J.; Lu, D.; Hawks, S. A.; Xie, C., Thermochromic halide perovskite solar cells. *Nat. Mater.* **2018,** *17* (3), 261.

26. Zhu, W.; Zhang, Q.; Zhang, C.; Zhang, Z.; Chen, D.; Lin, Z.; Chang, J.; Zhang, J.; Hao, Y., Aged Precursor Solution toward Low-Temperature Fabrication of Efficient Carbon-based All-Inorganic Planar CsPbIBr2 Perovskite Solar Cells. *ACS Appl. Energy Mater.* **2018**.

27. Song, J.; Zheng, E.; Wang, X.-F.; Tian, W.; Miyasaka, T., Low-temperature-processed ZnO–SnO2 nanocomposite for efficient planar perovskite solar cells. *Sol. Energy Mater. Sol. Cells* **2016,** *144*, 623-630.

28. Ma, J.; Yang, G.; Qin, M.; Zheng, X.; Lei, H.; Chen, C.; Chen, Z.; Guo, Y.; Han, H.; Zhao, X., MgO Nanoparticle Modified Anode for Highly Efficient SnO_2-Based Planar Perovskite Solar Cells. *Adv. Sci.* **2017,** *4* (9), 1700031.

29. Hou, Y.; Chen, X.; Yang, S.; Li, C.; Zhao, H.; Yang, H. G., A Band-Edge Potential Gradient Heterostructure to Enhance Electron Extraction Efficiency of the Electron Transport Layer in High-Performance Perovskite Solar Cells. *Adv. Funct. Mater.* **2017,** *27* (27), 1700878.

30. Sum, T. C.; Mathews, N., Advancements in perovskite solar cells: photophysics behind the photovoltaics. *Energy Environ. Sci.* **2014,** *7* (8), 2518-2534.

31. Huang, J.; Yuan, Y.; Shao, Y.; Yan, Y., Understanding the physical properties of hybrid perovskites for photovoltaic applications. *Nat. Rev. Mater.* **2017,** *2* (7), 17042.

32. Wong, K. K.; Fakharuddin, A.; Ehrenreich, P.; Deckert, T.; Abdi-Jalebi, M.; Friend, R. H.; Schmidt-Mende, L., Interface-Dependent Radiative and Nonradiative Recombination in Perovskite Solar Cells. *J. Phys. Chem. C* **2018,** *122* (20), 10691-10698.

33. Ito, S.; Tanaka, S.; Manabe, K.; Nishino, H., Effects of surface blocking layer of Sb2S3 on nanocrystalline TiO2 for CH3NH3PbI3 perovskite solar cells. *J. Phys. Chem. C* **2014,** *118* (30), 16995-17000.

34. Dong, Q.; Wang, M.; Zhang, Q.; Chen, F.; Zhang, S.; Bian, J.; Ma, T.; Wang, L.; Shi, Y., Discontinuous SnO2 derived blended-interfacial-layer in mesoscopic perovskite solar cells: Minimizing electron transfer resistance and improving stability. *Nano energy* **2017,** *38*, 358-367.

35. Draguta, S.; Sharia, O.; Yoon, S. J.; Brennan, M. C.; Morozov, Y. V.; Manser, J. M.; Kamat, P. V.; Schneider, W. F.; Kuno, M., Rationalizing the light-induced phase separation of mixed halide organic–inorganic perovskites. *Nat. Commun.* **2017,** *8* (1), 200.

36. Zhang, W.; Burlakov, V. M.; Graham, D. J.; Leijtens, T.; Osherov, A.; Bulović, V.; Snaith, H. J.; Ginger, D. S.; Stranks, S. D., Photo-induced halide redistribution in organic–inorganic perovskite films. *Nat. Commun.* **2016,** *7*, 11683.

Chapter 5. Improving phase stability by metal doping

5.1 Introduction

Perovskite solar cells (PSCs) have been attracting tremendous attentions and have experienced high-speed development in performance recently.[1-2] The organic molecules, including MA and FA, are very favorable in forming high-quality perovskite films with high PCEs.[3] While the MA^+ and FA^+ are volatile at the temperature of 80 and 100 ^oC,[4-5] respectively, which cause the perovskites thermal unstable and consequently reduce the lifetime of the PSCs. Incorporating Cs^+ or completely replacing MA^+ and FA^+ with Cs^+ is regarded as a promising approach to solve the thermal stability issue because Cs based perovskite materials are extremely stable at high temperatures.[6] However, the Cs based perovskites possess an inevitable disadvantage where the photo-active black α-phase is unstable at room-temperature and very easily transforms to photo-non-active yellow δ-phase.[7-8] Therefore, it is an important topic to stabilize the photoactive phase in ambient conditions. Apart from reducing the crystal size and increasing the crystal strain etc.,[9-10] there are two main strategies to stabilize the black phase.

One approach is to incorporating Br^- into the perovskite structure because Br^- has a smaller ionic radius of 1.96 Å than I^- of 2.20 Å.[11] When Br^- is used as X ion in ABX_3 perovskite, the size of $[BX_6]^{4-}$ octahedral and the formed cubooctahedral voids for the Cs cation will be reduced, which promises larger Goldschmidt tolerance factor (τ) and more stable cubic perovskite phase.[12] However, Br^- incorporation will simultaneously enlarge the band gap of the perovskite, which is undesirable for light absorption. For balancing the photovoltaic performance and the structure stability, $CsPbI_2Br$ is a fine choice due to its proper band gap (1.90 eV) and higher phase stability than that of $CsPbI_3$.[13]

The other way is to substituting (doping and alloying) Pb^{2+} ions with other metal ions owing to the reduction of $[BX_6]$ size will ensure the Cs^+ matches well with the cubooctahedral voids, forming stable perovskite structure. Up to now, various kinds of metals have been introduced into the perovskite materials, such as divalent ions Ca^{2+}, Mn^{2+}, Sn^{2+}, Sr^{2+}, Zn^{2+} and trivalent ions Sb^{3+}, Bi^{3+}, $Eu^{3+,}$ and some other lanthanide ions.[12-14] These foreign ions have been proved to be efficient in increasing the stability of the black α-phase and enhancing/maintaining the performance of the resultant devices. While the possibility of incorporating metals ions with higher valences into the

perovskite is still unknown. Niobium (Nb) is a widely used element for doping conventional perovskite oxides ($BaTiO_3$, $BiFeO_3$ etc.) in modifying the microstructure, ferroelectric and piezoelectric properties, in which the Nb^{5+} ions will partly replace the B site atoms of perovskite.[15] While the ferroelectricity of the halide perovskite is regarded as one of the main origins for hysteresis phenomenon of PSCs.[16] Therefore, it is worth trying to incorporate Nb into the inorganic halide lead perovskite and to study its effect on the perovskite phase stability and the device performance.

In this paper, we incorporated Nb^{5+} into the $CsPbI_2Br$ perovskite and investigated its effect on the perovskite phase stability and photovoltaic performances. Results indicate that the introduction of Nb^{5+} can effectively stabilize the black α-phase of the $CsPbI_2Br$ perovskite at room-temperature in ambient condition, and higher Nb^{5+} concentration leads to a longer lifetime of black α-phase. Moreover, the Nb^{5+} doping enhances the performance and reduces the hysteresis of the all-inorganic PSCs. The theoretical calculation was also adopted to realize the impact of Nb doping on the electronic properties of the perovskite. We believe that this first work on pentavalent ion doping into the all-inorganic perovskite will bring deeper understanding of the mechanism of foreign metal ion incorporation in perovskite and unlock more opportunities for perovskite modification.

5.2 Experimental Section

5.2.1 Device Fabrication

The washing of ITO glass and the preparation of passivated SnO2 film is the same with that in Chapter 3 and Chapter, respectively. 1.0 M $CsPbI_2Br$ perovskite precursor was formed by dissolving the CsBr and PbI_2 (mole ratio of 1/1) in DMSO/DMF (v/v=9/1), then stirred at room temperature until the clear solution was obtained. The 0.2 M $NbCl_5$ stock solution was prepared by dissolving $NbCl_5$ into DMSO/DMF mixed solvent (v/v=9/1). A certain amount of $NbCl_5$ solution was added into the $CsPbI_2Br$ perovskite precursor and stirred for several hours, forming precursors with different amount of Nb^{5+} (from 0.5 to 4 mol% versus Pb). In the nitrogen-filled glove box, the perovskite precursor solution was spin-coated at 1000 rpm for 10s and then 3000 rpm for 30 s. Then the film was annealed at 40 ºC for 4 min and then 160 ºC for 10 min. The carbon electrode was deposited on the top of the $CsPbI_2Br$ film by doctor-blading technology using

scotch tape to control the electrode thickness. Then the cells were heated treated at 100 °C for 10 min to promote evaporation of residual solvents.

5.2.2 DFT Calculations

We performed DFT calculations using the Quantum ESPRESSO software package based on the planewave/pseudopotential method. The generalized gradient approximation (GGA) was chosed to form the exchange-correlation functional. The energy cutoff 40 Ry for the plane wave basis was set. The Brillouin zone integrals were performed using a 4×4×4 Monkhorst-Pack *k*-mesh grid. Calculations were done with the 2×2×2 supercell of $CsPbI_2Br$, and one Pb substituted by Nb yields the $CsPb_{0.875}Nb_{0.125}I_2Br$.

5.2.3 Characterizations

The characterization methods including XRD, SEM, UV-Vis spectra, EIS and J-V curve were introduced in Chapter 2. EDX was conducted by the Hitachi S-3400N. Photoelectron yield spectroscopy (PYS) was measured using a Bunkoukeiki KV205-HK with a applied voltage of -5.0 V under vacuum of 10^{-4} Pa.

5.3 Results and discussion

Different amount of Nb^{5+} (0.25 to 4 mol%) were introduced into the $CsPbI_2Br$ by adding a certain amount of 0.2 M $NbCl_5$ stock solution into 1.0 M CsBr and PbI_2 solution (check specific details in the supporting information). The obtained solutions after mixing for several hours are shown in Figure 1. It is interesting that the color of the perovskite precursors turns into darker brown with increasing the amount of $NbCl_5$, though the $NbCl_5$ and $CsPbI_2Br$ solution are transparent and yellow in color, respectively. The color change is hypothesized to be attributed to the interaction between Nb^{5+} and the perovskite precursor, rather than the Cl^- from $NbCl_5$.[9, 17] Moreover, there was no precipitate formed for Nb^{5+} containing solutions even stored for longer than one month, indicating homogeneous and stable properties.

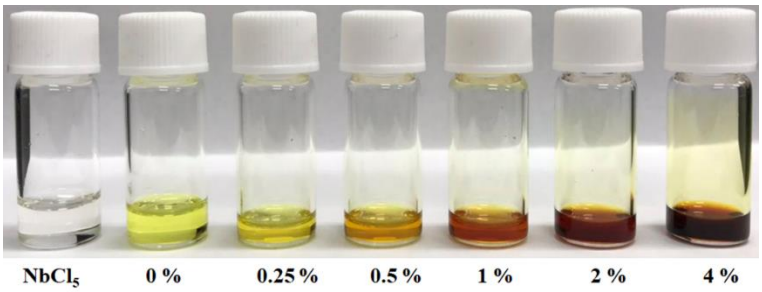

Figure 1 Photographs of perovskite precursors with different amount of Nb adding.

The precursor was spin-coated on the passivated SnO_2 film,[18] followed by a two-step annealing process. Specifically, the film was annealed at 40 ºC for several minutes to make the film vary from transparent to light brown and then 160 ºC to get the dark brown film. The first low-temperature annealing is for the mild solvent evaporation and the phase transition (from amorphous to main black α-phase).[19-20] In our experiments, for the control $CsPbI_2Br$ film, the optimized annealing time at 40 ºC is 4 min since longer time will form blurry film and shorter annealing time will result in a low coverage film due to inefficient mass transfer. In addition, it should be noted that the optimal 40 ºC annealing time for the Nb incorporated films decreases with higher Nb incorporation. For example, the proper annealing time at 40 ºC for the perovskite film with 0.5 mol% Nb^{5+} is 3 min. This might because the solutions with Nb have lower viscosity, and the Nb ions promote the nucleation and the phase transition process.[21]

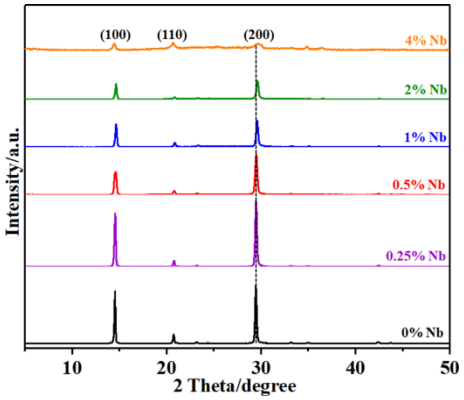

Figure 2 XRD patterns of $CsPbI_2Br$ films with different amount of Nb.

The XRD patterns of the samples after 160 ºC annealing for 10 min are shown in Figure 2. The XRD peaks at 14.6°, 20.8°, and 29.5° are assigned to (100), (110), and (200) face of $CsPbI_2Br$, respectively, which indicate that all the as-prepared samples are pure $CsPbI_2Br$ black perovskite phase without any impurity.[22]

Table 1 Parameters derived from the XRD patterns of $CsPbI_2Br$ films with different amount of Nb^{5+}.

Nb content (%)	Main peak position (°)	FWHM (main peak)	d-spacing (nm)	Lattice constant (nm)	Lattice strain (%)
0	29.44	0.164	0.3031	0.6062	0.080
0.25	29.48	0.214	0.3028	0.6056	0.085
0.5	29.49	0.247	0.3027	0.6054	0.098
1	29.55	0.253	0.3021	0.6041	0.140
2	29.61	0.266	0.3014	0.6029	0.210
4	29.70	0.643	0.3006	0.6012	0.287

While there are some differences between the samples. Firstly, the main peak at around 29.5° shifts to higher angle with increasing the amount of Nb^{5+}. The peak positions and the d spacing values are summarized in Table 1. Clearly, the d spacing reduces when the amount of Nb^{5+} increases. Secondly, the peak intensities reduce and the FWHM values enlarge with the Nb^{5+} adding amount increasing, meaning lower crystallinity. Therefore, the foreign Nb ions have a great effect on the crystallization process of the perovskite film.

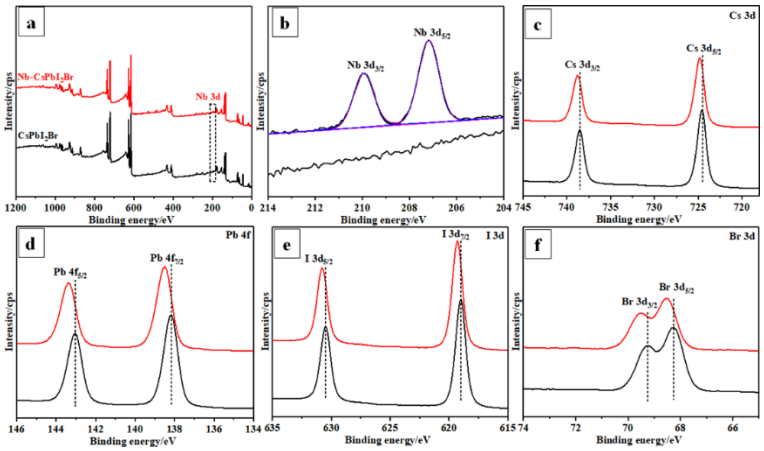

Figure 3 XPS spectra of pure (black line) and 4% incorporated (red line) $CsPbI_2Br$ films: (a) survey spectra; (b) Nb 3d; (c) Cs 3d; (d) Pb 4f (e) I 3d; (f) Br 3d.

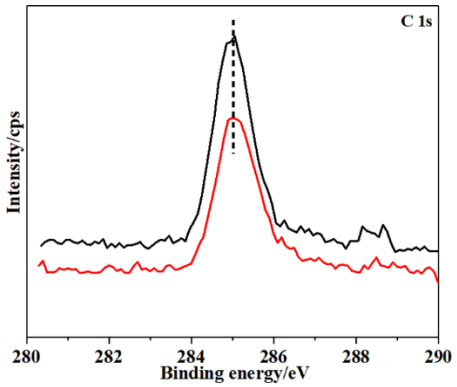

Figure 4 XPS spectrum of C1s for pure and 4% Nb incorporated $CsPbI_2Br$ film.

Figure 3 shows the XPS spectra of the pure $CsPbI_2Br$ and 4% Nb incorporated $CsPbI_2Br$ films. The presence of Nb^{5+} is evidenced through the explication of two binding energy peaks at around 200 eV, attributing to the Nb 3d core levels, which are not found in the pure sample (Figure 3a). Specifically, the two binding energy peaks at 209.9 and 207.2 eV (Figure 3b) are corresponding to Nb $3d_{3/2}$ and Nb $3d_{5/2}$, respectively.[23] Thus we can confirm that the Nb^{5+} was introduced into the perovskite film. Figure 3c-f show the XPS spectra of the Cs, Pb, I and Br elements, respectively. Notably, all the peaks of the Nb incorporated $CsPbI_2Br$ shift obviously compared with the pure film without Nb. The C1s peaks of the two samples (Figure 4) are at almost the same positions, indicative of the same measurement conditions. So the shift of the elements should be attributed to the effect of Nb^{5+} introduction rather than test error. The Nb should be located within the perovskite lattice because simple physical mixing of the elements could not lead to any remarkable chemical state change and shift of the XPS peaks.[21, 24-25] The theoretical study predicted that niobium trend to occupy the B site of the halide perovskite.[26] If so, partial replacing Pb^{2+} (1.19 Å) with the smaller Nb^{5+} (0.64 Å) will lead to the contraction of $[BX_6]$ and the changes in chemical bonding properties, which is reflected by the shift of XPS peaks for all the elements.[24] Moreover, the EDX elemental maps in Figure 5 indicate that Nb is uniformly distributed in the sample.

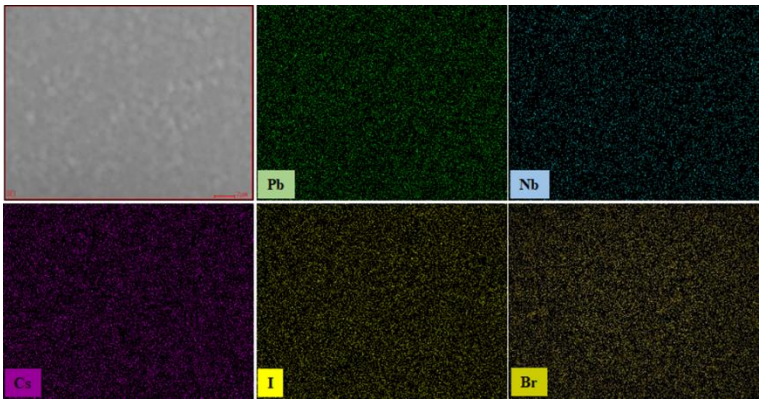

Figure 5 EDX element mapping of 1% Nb-doped $CsPbI_2Br$ film.

The lattice constants obtained from the XRD patterns are shown in Table 1. We can find that the lattice constant decreases with increasing Nb amount. Previous publications reported that the lattice increases if the foreign ions exist at the interstitial positions,[21] which is different from that of ours. Therefore, based on the variations including the reduction in lattice constants, shifts of XPS and XRD peaks and uniform Nb element dispersion, we can confirm that the Nb ions occupy the Pb positions.

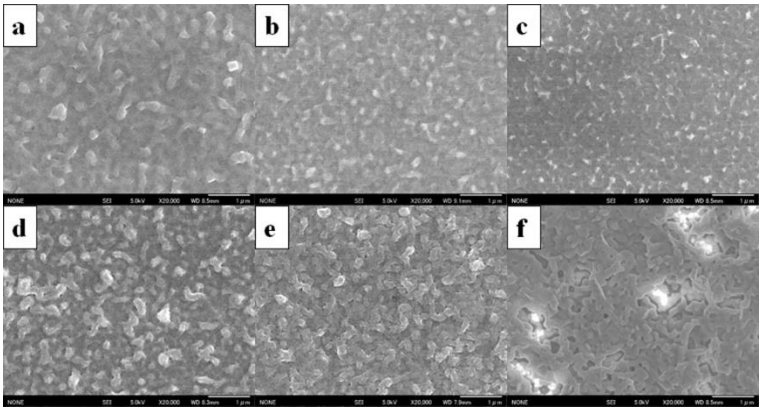

Figure 6 SEM images of $CsPbI_2Br$ films with different amount of Nb doping: (a) 0%; (b) 0.25%; (c) 0.5%; (d) 1%; (e) 2%; (f) 4%.

The SEM images of the samples with different amount of Nb are shown in Figure 6. The control perovskite film obtained by the two-step annealing process has a dense morphology without pinholes, which is promising for suppressing recombination of charges. The grain boundaries are not very clear because the anti-solvent was not used in our film preparation process, consistent with the other reports.[27-28] There are several branches on the film surface, meaning a non-uniform morphology, similar with that of the previous report.[24] When 0.25% amount Nb was

introduced into the perovskite, there are no obvious changes except that the branches disappeared. With 0.5% amount Nb incorporation, the film grew smoother and the crystal size became smaller and more uniform than that of the film without Nb. This might be attributed to the lower viscosity of the solution with Nb for better mass transfer and the role of Nb in promoting the nucleation process. The smaller crystal size means low crystallinity, in accordance with the XRD peak intensity reduction and FWHM enlargement.

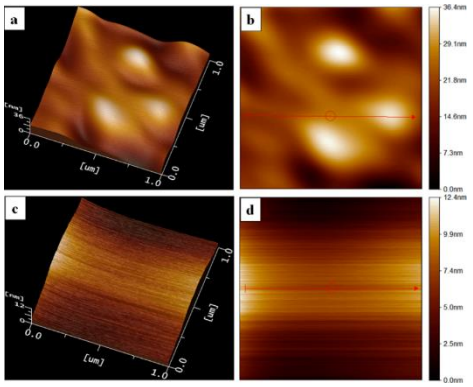

Figure 7 AFM images of (a) (b) 0 % and (c) (d) 0.5% Nb-doped $CsPbI_2Br$ film.

We further investigated the morphological surface of the pure and 0.5% Nb incorporated samples using atomic force microscope (AFM), as shown in Figure 7. Consistent with the SEM images, the film with 0.5% Nb doping exhibited a much smoother surface than that of the control film, with dramatically decreased root-square-roughness (Rq) from 4.54 nm to 0.89 nm. The smoother surface is beneficial for the contact between the perovskite and the carbon electrode.[29] While further increasing the amount of Nb doping makes the films rougher and non-uniform. For example, the film of 2% Nb has a rough surface with pinholes. The film with 4% Nb shows some independent white particles, which could be the segregation of excess $NbCl_5$ out of the perovskite grains.[9] To some extent, these segregated particles hinder the perovskite crystal growth and result in low-crystallinity films. Therefore, the film with 4% Nb has the lowest crystallinity and the lowest XRD peaks.

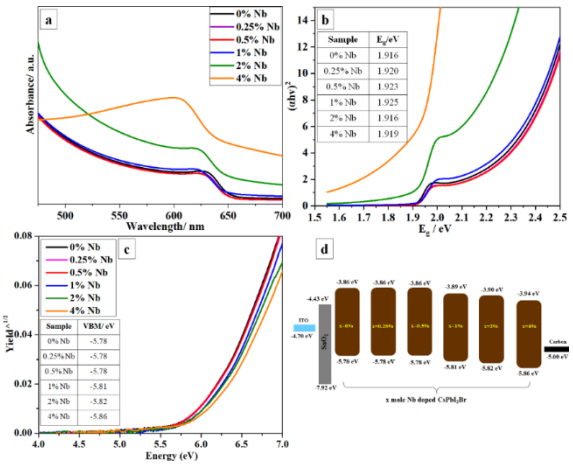

Figure 8 (a) UV-vis spectra, (b) tauc plots and (c) PYS spectra and (d) the resultant energy band structure of $CsPbI_2Br$ films with different amount of Nb doping, and the energy alignment for the components of the device.

It is accepted that the light absorption properties of the film are highly dependent on the film feature. From the UV-vis spectra (Figure 8a), we can find that the samples with low doping amount (less than 1%) have almost the same light absorption ability with that of the control sample, except a slight blue-shifting on the absorption edge. Obvious differences are observed when the doping amount is further improved to 2% and 4%: where the absorbance intensities become stronger and the absorption edges shift to longer wavelength. The band gaps of the materials were calculated by the tauc plots transformed from the UV-vis absorption spectra (Figure 8b). The corresponding values were summarized in the Table inserted in Figure 8b, where we can see that with Nb doping, the band gaps of the films become a little larger than that of the pure perovskite film. In addition, the band structure of the samples was investigated through the photoelectron yield spectroscopy (PYS), as shown in Figure 8c. The valence band maximum (VBM) from the PYS results and the corresponding conduction band minimum (CBM) calculated by combining the VBM and the band gaps are shown in Figure 8d. We can find that the minute amount of Nb doping has no effect on the band structure, while the VBM and CBM plunge when more than 1% amount of Nb is incorporated. The 4% Nb doping results the most obvious change with the lowest VBM and CBM positions. Thus, the band structure changes more obviously with increasing Nb concentration.

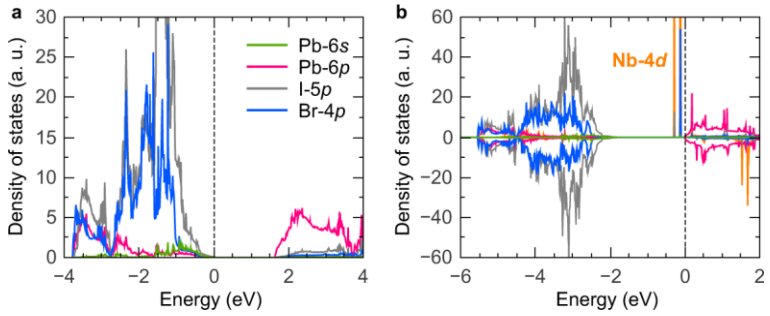

Figure 9 Partial density of states for (a) $CsPbI_2Br$ and (b) $CsPb_{0.875}Nb_{0.125}I_2Br$ calculated by GGA method. The Fermi energy level was set to zero.

To investigate the electronic properties of Nb-doped $CsPbI_2Br$, we calculated the partial density of states, which is shown in Figure 9. For the case of $CsPbI_2Br$, the valence bands maximum (VBM) is composed of I and Br *p*-orbitals with a small contribution from Pb 6*s*-orbitals, and the conduction bands minimum (CBM) mainly consists of the Pb 6*p*-orbitals. For the $CsPb_{0.875}Nb_{0.125}I_2Br$, the VBM exhibit similar electronic properties with $CsPbI_2Br$. After Nb substitution, the Nb 4*d*-orbitals split in different energy ranges respectively. Partial 4*d*-electrons of Nb localized on conduction bands at about 1.5 eV above the Fermi level in the spin-down channel. While in the spin-up channel, the interaction between Nb 4*d* with I and Br *p*-orbitals forms intermediate bands slightly below the Fermi energy level. Due to the Nb 4*d* electrons, the Fermi level shifts up to the CBM, resulting in the n-type semiconductor feature of $CsPb_{0.875}Nb_{0.125}I_2Br$, which is similar to the Sb for n-type doping.[30]

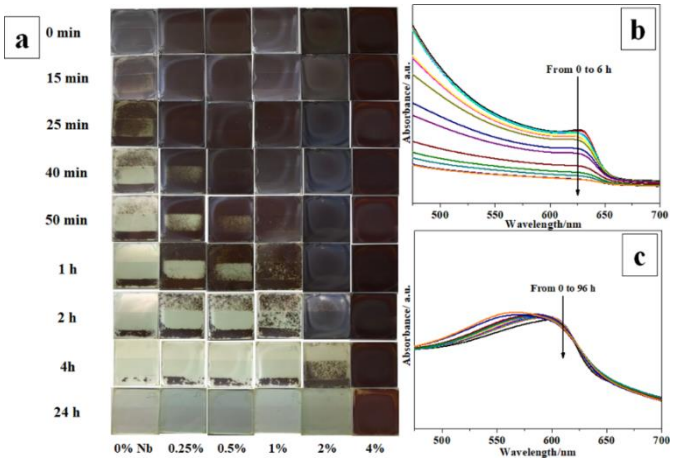

Figure 10 (a) Color variations of $CsPbI_2Br$ films with different amount of Nb doping. (test condition: ambient, 23 °C, RH=55%), and UV-vis spectra variation of (b) pure and (c) 4% Nb-doped $CsPbI_2Br$ film. (test condition: ambient, 21 °C, RH=30%).

Figure 10a shows the photographs of $CsPbI_2Br$ films stored in ambient at the temperature of 23 ºC and relative humidity (RH) of 55%. As observed, the color of the control sample faded in the first 15 min and the black α-phase wholly changed to yellow δ-phase in the first one hour, as depicted by the XRD variations in Figure 11.

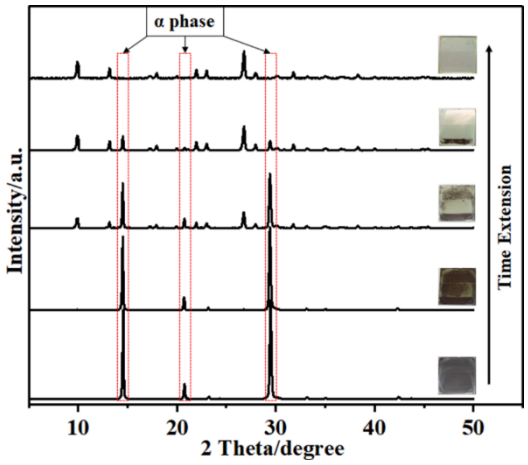

Figure 11 Time-dependent phase transition of pure $CsPbI_2Br$ film from black phase to the yellow phase.

When the Nb was doped into the perovskite, the black α-phase lasted for a longer time than that of the control one. For example, the film color of the 4% Nb-doped perovskite remains the same even after 24 hours. We recorded the variations of the control and the 4% Nb incorporated film by UV-vis spectra, as shown in Figure 10b and c. When the films were stored in ambient at 21 ºC with the RH of 30%, the characteristic absorption edge of the α-$CsPbI_2Br$ film completely disappeared after 6 h, while the 4% Nb-doped film has no changes even after 96 h. As a result, we concluded that the Nb can stabilize the α-$CsPbI_2Br$ at room-temperature and the lifetime prolongs with increasing Nb amount.

When Nb occupies the B site of the $CsPbI_2Br$ crystal structure, its smaller size and more electron charge will decrease the $[BX_6]$ size and shrink the lattice, which makes the Cs match well with the cubooctahedral voids, thus stabilize the perovskite structure. This can be verified by the variation in Goldschmidt's tolerance factor (τ) as Equation (1):[31]

$$\tau = \frac{R_A + R_X}{\sqrt{2}(R_B + R_X)} \tag{5-1}$$

The R_A, R_B, and R_X represent the ionic radius of A-site cation, B-site cation, and X-site anion, respectively. The perovskite will form an orthorhombic structure when $\tau < 0.8$, cubic structure when $0.8 < \tau < 1$, and hexagonal structure when $\tau > 1$. Therefore, the bromine-based perovskite with smaller [BX_6] octahedral size and larger tolerance factor, possesses better phase stability than the iodide perovskites (τ=0.807 for $CsPbI_3$ and 0.815 for $CsPbBr_3$). As for the mixed A-site, B-site, and mixed halide perovskite, the τ is calculated using effective ion size. For example, the effective halide size of $CsPbI_xBr_{3-x}$ can be calculated by Equation (2):[31]

$$R_{effective} = \frac{x}{3}R_{I^-} + \frac{3-x}{3}R_{Br^-} \quad (5\text{-}2)$$

As a result, the effective size of halide in $CsPbI_2Br$ is 2.12 Å and the τ is 0.810. Similarly, the effective size of B-site ion in Nb-doped $CsNb_xPb_{1-x}I_2Br$ can be calculated by Equation (3):

$$R_{effective} = xR_{Nb^{5+}} + (1-x)R_{Pb^{2+}} \quad (5\text{-}3)$$

Table 2 Tolerance factor of $CsPbI_2Br$ materials with different amount of Nb^{5+} doping.

Nb content (%)	$R_{Pb/Nb}$ (Å)	Tolerance factor (τ)
0	1.190	0.8098
0.25	1.189	0.8101
0.5	1.187	0.8104
1	1.185	0.8111
2	1.179	0.8125
4	1.168	0.8152

According to the above equations, we calculated and listed the τ of different amount Nb-doped perovskite materials in Table 2. When 4% Nb was incorporated into the perovskite, the effective cation size of mixed Nb and Pb is 1.168 Å, resulting in a τ value of 0.815. Therefore, the perovskite with 4% Nb doping possesses the highest stability. In addition, the lattice strain promotes the phase stability by causing distortion of cubic structure.[9, 17] We analyzed the lattice strain by refining the XRD patterns and the results are shown in Table 1. We found that the lattice strain increases with increasing the amount of Nb, which agrees with the stability gradient.

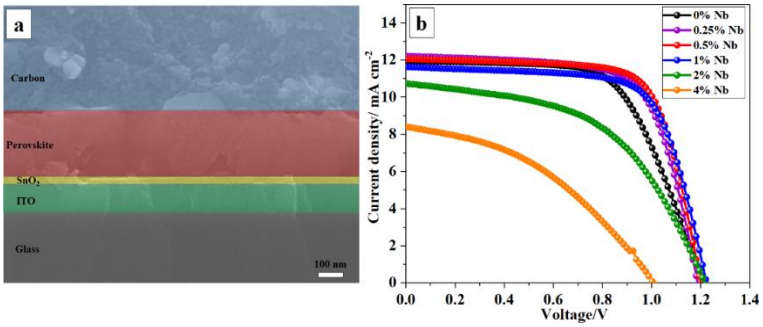

Figure 12 (a) Cross-sectional SEM image of carbon electrode based $CsPbI_2Br$ perovskite device and (b) J-V curves of the devices with different amount of Nb doping.

Table 3 Photovoltaic parameters of $CsPbI_2Br$ perovskite solar cells with different amount of Nb^{5+} doping.

Sample	V_{oc}/V	J_{sc}/mA cm^{-2}	FF	PCE/%
0% Nb	1.21	11.95	0.63	9.05
0.25% Nb	1.18	12.22	0.69	9.94
0.5% Nb	1.20	12.06	0.72	10.42
1% Nb	1.22	11.63	0.69	9.84
2% Nb	1.21	10.73	0.52	6.69
4% Nb	1.00	8.42	0.40	3.41

Using Nb doped perovskite as absorber, we fabricated a carbon electrode based HTM-free device, as depicted by the cross-sectional SEM image of the solar cells (Figure 12a). Figure 12b shows the champion *J-V* curves of the devices based on $CsPbI_2Br$ with different Nb doping concentration and parameters are listed in Table 3. The device based on $CsPbI_2Br$ without dopant achieved a PCE of 9.05%, which is much higher than that of the literature (4.75%) with the same fabrication process, components and device structure.[27] For the Nb-doped PSCs, the device gave the highest PCE of 10.42% when 0.5% Nb was added, high than ever-reported carbon-based all-inorganic $CsPbI_2Br$ PSCs.[13] The J_{sc} value matches well with the calculated value from the IPCE spectra (Figure 13a). The stability of output (SOP) of the reference and 0.5% Nb-based device is shown in Figure 13b and c. We observed that both the devices maintain high performances under continuous measurements for 120 s. The low J_{sc} of the devices with 2% and 4% amount Nb should be attributed to their lower film qualities. The obvious increasing in FF was achieved with less than 2% Nb doping, which is the main reason for the device performance enhancement.

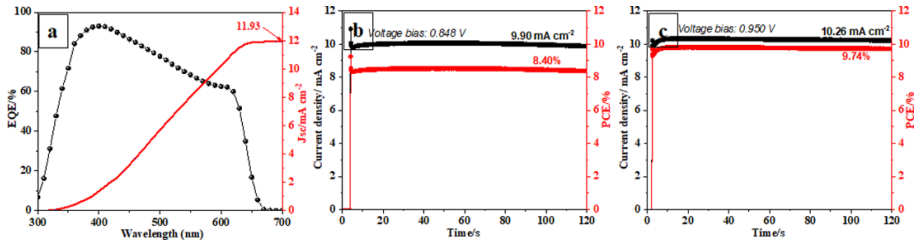

Figure 13 (a) IPCE for 0.5% Nb-doped $CsPbI_2Br$ based device, stability of output (SOP) of (b) pure and (c) 0.5% Nb-doped $CsPbI_2Br$ based device.

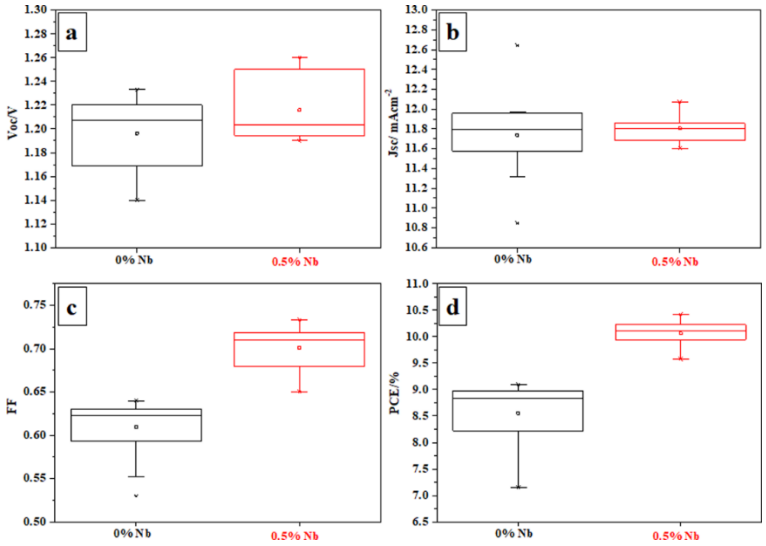

Figure 14 Photovoltaic statistics for 0 % and 0.5% Nb-doped $CsPbI_2Br$ solar cells with carbon electrode (18 cells for either type): (a) V_{oc}; (b) J_{sc}; (c) FF; (d) PCE.

Table 4 Photovoltaic statistics parameters for 0 % and 0.5% Nb doped $CsPbI_2Br$ solar cells with carbon electrode.

Device	V_{oc} /V	Jsc/mA cm^{-2}	FF	PCE/%
0% Nb	1.20±0.03	11.74±0.37	0.60±0.03	8.56±0.57
0.5 % Nb	1.22±0.03	11.81±0.15	0.70±0.03	10.06±0.23

In order to verify the reproducibility of the device performances, we fabricated 18 cells for the reference and 0.5% Nb-based PSCs and the detailed statistics of the photovoltaic parameters for the devices are presented in Figure 14 and summarized in Table 4. Results indicate that the J_{sc} values are very similar owing to their same optical properties. The average FF was enhanced from

0.60 to 0.70, which could be attributed to the uniform morphology and smooth surface that provides better contact with the carbon electrode,[32-33] as shown in the AFM results (Figure 7).

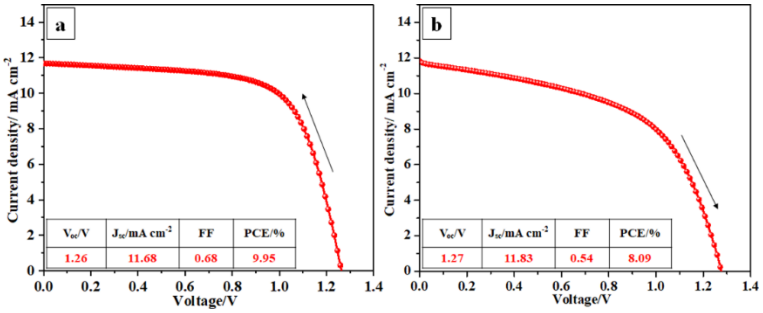

Figure 15 J-V curves of 0.5% Nb-doped $CsPbI_2Br$ based devices with champion V_{oc} obtained by scanning from different directions: (a) reverse scanning (RS); (b) forward scanning (FS).

The V_{oc} was enhanced from an average of 1.20 to 1.22 V, where the champion V_{oc} of 1.26 V was achieved for the reverse scan (RS) and 1.27 V for the forward scan (FS) when 0.5% Nb was doped into the $CsPbI_2Br$ perovskite (Figure 15), which are higher than most of the $CsPbI_2Br$ based PSCs regardless of carbon or noble metal electrode. Finally, the average PCE was increased from 8.56% to 10.06% with 0.5% Nb doping.

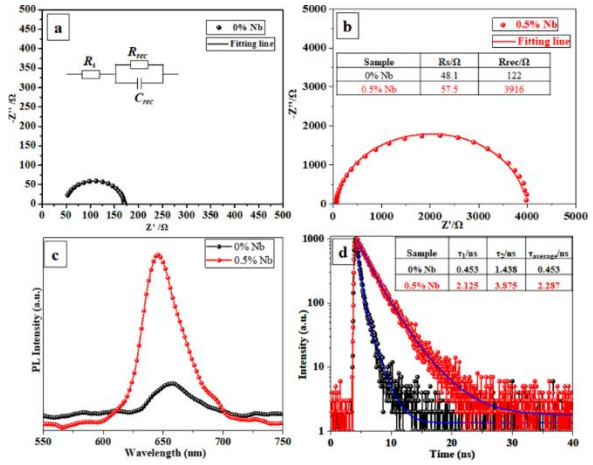

Figure 16 Nyquist plots of (a) 0 % and (b) 0.5% Nb-doped $CsPbI_2Br$ based device, (c) PL and (d) TRPL spectra of 0 % and 0.5% Nb-doped $CsPbI_2Br$ film.

The EIS measurements were made to investigate the charge transfer properties of the PSCs. The measurement was conducted at an applied bias of 0.6 V in dark condition and the results for the reference and 0.5% Nb-based PSCs are shown in Figure 16a and b. The equivalent circuit and the fitting results are inserted in the Figure. . Generally, the high-frequency arc is related to the

charge transporting and the arc at the low-frequency region represents the recombination resistance at perovskite/SnO_2 and perovskite/carbon interface.[34-35] The two samples have very similar R_s due to the same device structure. While the 0.5% Nb-doped $CsPbI_2Br$ based device has much higher R_{rec} (3916 Ω) than that of the reference device (122 Ω), which implies that the recombination process in the former device is highly suppressed.[36] The highly increased recombination resistance is account for the high V_{oc} of 1.27 V.

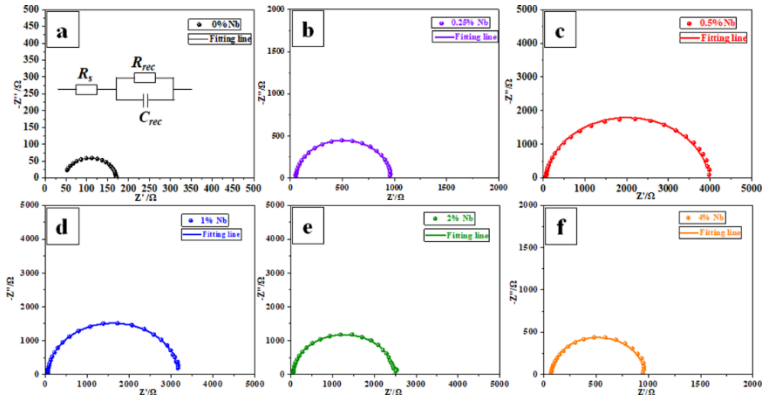

Figure 17 Nyquist plots of different amount Nb-doped $CsPbI_2Br$ based device.

Table 5 Resistance summary of different amount of Nb-doped $CsPbI_2Br$ based devices.

Nb content (%)	Rs/Ω	Rrec/Ω
0	48.1	122
0.25	52.3	909
0.5	57.5	3916
1	59.4	3118
2	56.6	2421
4	67.4	885

We also measured the EIS of other devices with different Nb doping amount, as shown in Figure 17 and Table 5. We found that after Nb incorporation, the devices possess larger R_{rec} than that of the control device. Therefore, the Nb doping can effectively suppress the charge recombination in PSCs.

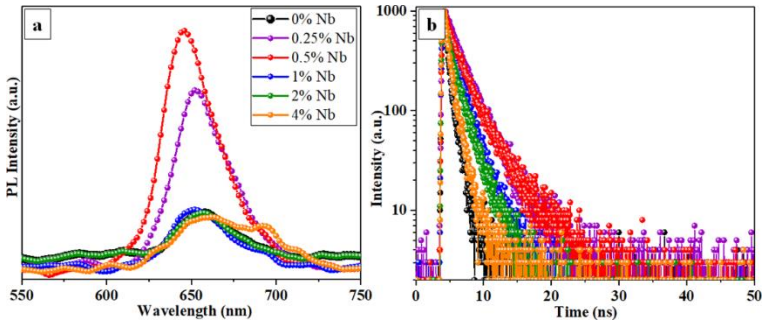

Figure 18 PL (a) and TRPL (b) of different amount Nb-doped $CsPbI_2Br$ film.

To better understand the effect of Nb doping on the electron extraction and transport process, the PL and TRPL measurements for the perovskite films were carried out. The results for the reference and 0.5% Nb-doped film are shown in Figure 16c and d. It is obvious that the PL intensity sharply increases after 0.5% Nb incorporation. The higher PL intensity is associated with the fewer traps and defects in the perovskite layer.[37] Thus 0.5% Nb doping can significantly reduce the traps and defects in the perovskite film, meaning better film quality and promising for better performance.[38-39] Moreover, a blue shift in the PL spectra is observed with the maxima at 658 and 646 nm for 0% and 0.5% Nb, respectively. This is attributed to the reduction in crystallinity and grain size after 0.5% Nb incorporation.[10, 39] In contrast, the larger amount of Nb-doped into the perovskite film induces lower film qualities with increased traps and defects, thus the blue shifts are not striking (Figure 18a). Figure 16d shows the TRPL spectra of the samples and the decay time (τ) is calculated via the double-exponential fits of Equation (4):

$$y = A1 * \exp\left(-\frac{x}{\tau 1}\right) + A2 * \exp\left(-\frac{x}{\tau 2}\right) + y0 \quad (5\text{-}4)$$

The former (τ_1) is resulted from the surface recombination process while the latter (τ_2) is related to the charge recombination in the grains.[40] The fitted parameters are listed in the Table inserted in Figure 16d. For the reference $CsPbI_2Br$ film, the PL lifetimes are 0.453 and 1.438 ns for τ_1 and τ_2, respectively. While the PL lifetime was prolonged to 2.125 and 3.875 ns for τ_1 and τ_2, respectively. As observed from Figure 18b, all the films with Nb doping (less than 2%) exhibited longer lifetime than the control film, indicative of the suppressed recombination process in the perovskite film,[41-42] which is consistent with the performances of the devices.

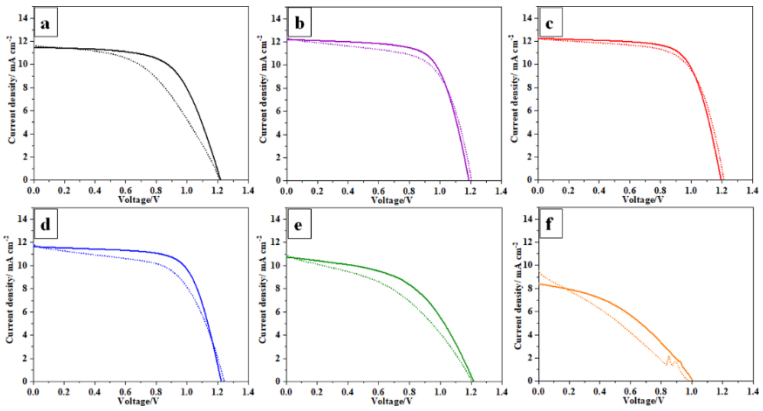

Figure 19 J-V curves of carbon-based $CsPbI_2Br$ PSCs with different amount of Nb doping under reverse scanning (full line) and forward scanning (dotted line) direction: (a) 0%; (b) 0.25%; (c) 0.5%; (d) 1%; (e) 2%; (f) 4%.

Table 6 Photovoltaic parameters of carbon-based $CsPbI_2Br$ PSCs with different amount of Nb doping under reverse scanning (RS) and forward scanning (FS) directions.

Sample	Scan direction	V_{oc}/V	Jsc/mA cm^{-2}	FF	PCE/%	Hysteresis Index/%
0% Nb	RS	1.21	11.46	0.63	8.74	18.99
	FS	1.21	11.69	0.50	7.08	
0.25% Nb	RS	1.18	12.22	0.69	9.94	5.94
	FS	1.19	12.45	0.63	9.35	
0.5% Nb	RS	1.18	12.24	0.70	10.14	3.55
	FS	1.21	12.41	0.65	9.78	
1% Nb	RS	1.22	11.63	0.69	9.84	12.60
	FS	1.23	11.91	0.59	8.60	
2% Nb	RS	1.21	10.73	0.52	6.69	16.89
	FS	1.21	11.00	0.42	5.56	
4% Nb	RS	1.00	8.42	0.40	3.41	22.58
	FS	0.98	9.53	0.28	2.64	

Hysteresis is commonly coming along with the photovoltaic performance measurements of PSCs, especially for the planar PSCs. There are several reasons account for the hysteresis, such as the ferroelectricity, electronic trap states, and the interfacial charge extraction velocity.[43] Figure 19 compares the hysteresis properties of the PSCs with different amount of Nb doping by measuring the device in both reverse and forward scanning directions. The hysteresis index (HI) is defined as Equation (5):[44]

$$Hysteresis\ index = \frac{PCE_{reverse} - PCE_{forward}}{PCE_{reverse}} \quad (5\text{-}5)$$

The HI of the devices are summarized in Table 6. The results illustrate that the reference device without Nb has obvious hysteresis with the HI value of 18.99%. When a certain amount of Nb (less than 2%) is incorporated into the film, the hysteresis is effectively suppressed. Among the devices, the 0.5% Nb-doped device has the smallest and negligible HI of 3.55%, owing to the reduced traps states by the proper amount of Nb doping,[45] as mentioned above. In contrast, the 4% Nb-doped film based solar cells exhibited a severe hysteresis phenomenon with the HI of 22.58% due to its large amount of traps states in the film.

5.4 Conclusions

In summary, we reported an all-inorganic Nb incorporated $CsPbI_2Br$ perovskite for the first time. Results indicate that the Nb is incorporated into the perovskite lattice with a slight substitution of Pb, which increases the perovskite tolerance factor and significantly stabilizes the α-$CsPbI_2Br$ phase. With 0.5% Nb incorporation, a record-high PCE of 10.42% was achieved for a carbon-based PSCs. The Nb incorporation has effectively reduced the charge recombination in the perovskite, resulting in high V_{oc} of 1.27 V and nearly hysteresis-free device. This work explicates the potential of the high-valence ions to serve as foreign ions to modify the properties of all-inorganic perovskite materials.

References

1. Kojima, A.; Teshima, K.; Shirai, Y.; Miyasaka, T., Organometal halide perovskites as visible-light sensitizers for photovoltaic cells. *J. Am. Chem. Soc.* **2009,** *131* (17), 6050-6051.

2. https://www.nrel.gov/pv/assets/pdfs/pv-efficiency-chart.20190103.pdf.

3. Zhou, Y.; Yang, M.; Pang, S.; Zhu, K.; Padture, N. P., Exceptional morphology-preserving evolution of formamidinium lead triiodide perovskite thin films via organic-cation displacement. *J. Am. Chem. Soc.* **2016,** *138* (17), 5535-5538.

4. Kim, N.-K.; Min, Y. H.; Noh, S.; Cho, E.; Jeong, G.; Joo, M.; Ahn, S.-W.; Lee, J. S.; Kim, S.; Ihm, K., Investigation of Thermally Induced Degradation in $CH_3NH_3PbI_3$ Perovskite Solar Cells Using In-Situ Synchrotron Radiation Analysis. *Sci. Rep.* **2017,** *7* (1), 4645.

5. Zhou, G.; Wu, J.; Zhao, Y.; Li, Y.; Shi, J.; Li, Y.; Wu, H.; Li, D.; Luo, Y.; Meng, Q., Application of Cesium on the Restriction of Precursor Crystallization for Highly Reproducible Perovskite Solar Cells Exceeding 20% Efficiency. *ACS Appl. Mater. Inter.* **2018,** *10* (11), 9503-9513.

6. Park, N.-G.; Grätzel, M.; Miyasaka, T.; Zhu, K.; Emery, K., Towards stable and commercially available perovskite solar cells. *Nat. Energy* **2016,** *1* (11), 16152.

7. Nam, J. K.; Chun, D. H.; Rhee, R. J. K.; Lee, J. H.; Park, J. H., Methodologies toward Efficient and Stable Cesium Lead Halide Perovskite-Based Solar Cells. *Adv. Sci.* **2018**, 1800509.

8. Lin, J.; Lai, M.; Dou, L.; Kley, C. S.; Chen, H.; Peng, F.; Sun, J.; Lu, D.; Hawks, S. A.; Xie, C., Thermochromic halide perovskite solar cells. *Nat. Mater.* **2018,** *17* (3), 261.

9. Jena, A. K.; Kulkarni, A.; Sanehira, Y.; Ikegami, M.; Miyasaka, T., Stabilization of α-$CsPbI_3$ in Ambient Room Temperature Conditions by Incorporating Eu into $CsPbI_3$. *Chem. Mater.* **2018,** *30* (19), 6668-6674.

10. Xiang, W.; Wang, Z.; Kubicki, D. J.; Tress, W.; Luo, J.; Prochowicz, D.; Akin, S.; Emsley, L.; Zhou, J.; Dietler, G., Europium-Doped $CsPbI_2Br$ for Stable and Highly Efficient Inorganic Perovskite Solar Cells. *Joule* **2018,** *3*, 1-10.

11. Sutton, R. J.; Eperon, G. E.; Miranda, L.; Parrott, E. S.; Kamino, B. A.; Patel, J. B.; Hörantner, M. T.; Johnston, M. B.; Haghighirad, A. A.; Moore, D. T., Bandgap-tunable cesium lead halide perovskites with high thermal stability for efficient solar cells. *Adv. Energy Mater.* **2016,** *6* (8), 1502458.

12. Swarnkar, A.; Mir, W. J.; Nag, A., Can B-site doping or alloying improve thermal-and phase-stability of all-inorganic $CsPbX_3$ (X=Cl, Br, I) perovskites? *ACS Energy Lett.* **2018,** *3* (2), 286-289.

13. Zeng, Q.; Zhang, X.; Liu, C.; Feng, T.; Chen, Z.; Zhang, W.; Zheng, W.; Zhang, H.; Yang, B., Inorganic $CsPbI_2Br$ Perovskite Solar Cells: The Progress and Perspective. *Sol. RRL* **2018**, 1800239.

14. Zhou, Y.; Chen, J.; Bakr, O. M.; Sun, H.-T., Metal-Doped Lead Halide Perovskites: Synthesis, Properties, and Optoelectronic Applications. *Chem. Mater.* **2018,** *30* (19), 6589-6613.

15. Wu, X.; Luo, L.; Jiang, N.; Wu, X.; Zheng, Q., Effects of Nb doping on the microstructure, ferroelectric and piezoelectric properties of $0.7BiFeO_3$–$0.3BaTiO_3$ lead-free ceramics. *Bull. Mater. Sci.* **2016,** *39* (3), 737-742.

16. Wei, J.; Zhao, Y.; Li, H.; Li, G.; Pan, J.; Xu, D.; Zhao, Q.; Yu, D., Hysteresis analysis based on the ferroelectric effect in hybrid perovskite solar cells. *J. Phys. Chem. Lett.* **2014,** *5* (21), 3937-3945.

17. Hu, Y.; Bai, F.; Liu, X.; Ji, Q.; Miao, X.; Qiu, T.; Zhang, S., Bismuth incorporation stabilized α-$CsPbI_3$ for fully inorganic perovskite solar cells. *ACS Energy Lett.* **2017,** *2* (10), 2219-2227.

18. Guo, Z.; Teo, S.; Xu, Z.; Zhang, C.; Kamata, Y.; Hayase, S.; Ma, T., Achievable high Voc of carbon-based all-inorganic $CsPbIBr_2$ perovskite solar cells through interface engineering. *J. Mater. Chem. A* **2019,** *7*, 1227-1232.

19. Liu, C.; Li, W.; Zhang, C.; Ma, Y.; Fan, J.; Mai, Y., All-inorganic $CsPbI_2Br$ perovskite solar cells with high efficiency exceeding 13%. *J. Am. Chem. Soc.* **2018,** *140* (11), 3825-3828.

20. Wang, P.; Zhang, X.; Zhou, Y.; Jiang, Q.; Ye, Q.; Chu, Z.; Li, X.; Yang, X.; Yin, Z.; You, J., Solvent-controlled growth of inorganic perovskite films in dry environment for efficient and stable solar cells. *Nat. Commun.* **2018,** *9* (1), 2225.

21. Bai, D.; Zhang, J.; Jin, Z.; Bian, H.; Wang, K.; Wang, H.; Liang, L.; Wang, Q.; Liu, S. F., Interstitial Mn^{2+}-driven high-aspect-ratio grain growth for low-trap-density microcrystalline films for record efficiency $CsPbI_2Br$ solar cells. *ACS Energy Lett.* **2018,** *3* (4), 970-978.

22. Christodoulou, S.; Di Stasio, F.; Pradhan, S.; Stavrinadis, A.; Konstantatos, G., High-Open-Circuit-Voltage Solar Cells Based on Bright Mixed-Halide $CsPbBrI_2$ Perovskite Nanocrystals Synthesized under Ambient Air Conditions. *J. Phys. Chem. C* **2018,** *122* (14), 7621-7626.

23. Yin, G.; Ma, J.; Jiang, H.; Li, J.; Yang, D.; Gao, F.; Zeng, J.; Liu, Z.; Liu, S. F., Enhancing efficiency and stability of perovskite solar cells through Nb-doping of TiO_2 at low temperature. *ACS Appl. Mater. Inter.* **2017,** *9* (12), 10752-10758.

24. Liang, J.; Liu, Z.; Qiu, L.; Hawash, Z.; Meng, L.; Wu, Z.; Jiang, Y.; Ono, L. K.; Qi, Y., Enhancing Optical, Electronic, Crystalline, and Morphological Properties of Cesium Lead Halide by Mn Substitution for High-Stability All-Inorganic Perovskite Solar Cells with Carbon Electrodes. *Adv. Energy Mater.* **2018**, 1800504.

25. Nam, J. K.; Chai, S. U.; Cha, W.; Choi, Y. J.; Kim, W.; Jung, M. S.; Kwon, J.; Kim, D.; Park, J. H., Potassium incorporation for enhanced performance and stability of fully inorganic cesium lead halide perovskite solar cells. *Nano Lett.* **2017,** *17* (3), 2028-2033.

26. Petrović, M.; Chellappan, V.; Ramakrishna, S., Perovskites: solar cells & engineering applications–materials and device developments. *Sol. Energy* **2015,** *122*, 678-699.

27. Dong, C.; Han, X.; Zhao, Y.; Li, J.; Chang, L.; Zhao, W., A Green Anti-Solvent Process for High Performance Carbon-Based $CsPbI_2Br$ All-Inorganic Perovskite Solar Cell. *Sol. RRL* **2018,** *2* (9), 1800139.

28. Liu, C.; Li, W.; Li, H.; Wang, H.; Zhang, C.; Yang, Y.; Gao, X.; Xue, Q.; Yip, H. L.; Fan, J., Structurally Reconstructed $CsPbI_2Br$ Perovskite for Highly Stable and Square-Centimeter All-Inorganic Perovskite Solar Cells. *Adv. Energy Mater.* **2018**, 1803572.

29. You, P.; Liu, Z.; Tai, Q.; Liu, S.; Yan, F., Efficient semitransparent perovskite solar cells with graphene electrodes. *Adv. Mater.* **2015,** *27* (24), 3632-3638.

30. Zhang, J.; Shang, M.-h.; Wang, P.; Huang, X.; Xu, J.; Hu, Z.; Zhu, Y.; Han, L., n-Type Doping and Energy States Tuning in $CH_3NH_3Pb_{1-x}Sb_{2x/3}I_3$ Perovskite Solar Cells. *ACS Energy Lett.* **2016,** *1* (3), 535-541.

31. Li, Z.; Yang, M.; Park, J.-S.; Wei, S.-H.; Berry, J. J.; Zhu, K., Stabilizing perovskite structures by tuning tolerance factor: formation of formamidinium and cesium lead iodide solid-state alloys. *Chem. Mater.* **2015,** *28* (1), 284-292.

32. Guo, Z.; Gao, L.; Xu, Z.; Teo, S.; Zhang, C.; Kamata, Y.; Hayase, S.; Ma, T., High Electrical Conductivity 2D MXene Serves as Additive of Perovskite for Efficient Solar Cells. *Small* **2018,** *14* (47), 1802738.

33. Zuo, C.; Ding, L., An 80.11% FF record achieved for perovskite solar cells by using the NH_4Cl additive. *Nanoscale* **2014,** *6* (17), 9935-9938.

34. Ma, J.; Yang, G.; Qin, M.; Zheng, X.; Lei, H.; Chen, C.; Chen, Z.; Guo, Y.; Han, H.; Zhao, X., MgO Nanoparticle Modified Anode for Highly Efficient SnO_2-Based Planar Perovskite Solar Cells. *Adv. Sci.* **2017,** *4* (9), 1700031.

35. Hou, Y.; Chen, X.; Yang, S.; Li, C.; Zhao, H.; Yang, H. G., A Band-Edge Potential Gradient Heterostructure to Enhance Electron Extraction Efficiency of the Electron Transport Layer in High-Performance Perovskite Solar Cells. *Adv. Funct. Mater.* **2017,** *27* (27), 1700878.

36. Yang, F.; Hirotani, D.; Kapil, G.; Kamarudin, M. A.; Ng, C. H.; Zhang, Y.; Shen, Q.; Hayase, S., All-Inorganic $CsPb_{1-x}Ge_xI_2Br$ Perovskite with Enhanced Phase Stability and Photovoltaic Performance. *Angew. Chem. Int. Ed.* **2018,** *57* (39), 12745-12749.

37. Zhao, W.; Yao, Z.; Yu, F.; Yang, D.; Liu, S., Alkali Metal Doping for Improved $CH_3NH_3PbI_3$ Perovskite Solar Cells. *Adv. Sci.* **2018,** *5* (2), 1700131.

38. Zhao, W.; Yang, D.; Yang, Z.; Liu, S. F., Zn-doping for reduced hysteresis and improved performance of methylammonium lead iodide perovskite hybrid solar cells. *Mater. Today Energy* **2017,** *5*, 205-213.

39. Xiang, S.; Li, W.; Wei, Y.; Liu, J.; Liu, H.; Zhu, L.; Chen, H., The synergistic effect of non-stoichiometry and Sb-doping on air-stable α-$CsPbI_3$ for efficient carbon-based perovskite solar cells. *Nanoscale* **2018,** *10*, 9996-10004

40. Chen, Q.; Chen, L.; Ye, F.; Zhao, T.; Tang, F.; Rajagopal, A.; Jiang, Z.; Jiang, S.; Jen, A. K.-Y.; Xie, Y., Ag-incorporated organic–inorganic perovskite films and planar heterojunction solar cells. *Nano Lett.* **2017,** *17*, 3231-3237.

41. Dong, Q.; Wang, Z.; Zhang, K.; Yu, H.; Huang, P.; Liu, X.; Zhou, Y.; Chen, N.; Song, B., Easily accessible polymer additives for tuning the crystal-growth of perovskite thin-films for highly efficient solar cells. *Nanoscale* **2016,** *8*, 5552-5558.

42. Hadadian, M.; Correa-Baena, J. P.; Goharshadi, E. K.; Ummadisingu, A.; Seo, J. Y.; Luo, J.; Gholipour, S.; Zakeeruddin, S. M.; Saliba, M.; Abate, A., Enhancing Efficiency of Perovskite Solar Cells via N-doped Graphene: Crystal Modification and Surface Passivation. *Adv. Mater.* **2016,** *28*, 8681-8686.

43. Chen, B.; Yang, M.; Priya, S.; Zhu, K., Origin of J–V hysteresis in perovskite solar cells. *J. Phys. Chem. Lett.* **2016,** *7* (5), 905-917.

44. Li, W.; Rothmann, M. U.; Liu, A.; Wang, Z.; Zhang, Y.; Pascoe, A. R.; Lu, J.; Jiang, L.; Chen, Y.; Huang, F., Phase segregation enhanced ion movement in efficient inorganic $CsPbIBr_2$ solar cells. *Adv. Energy Mater.* **2017,** *7* (20), 1700946.

45. Lee, J.-W.; Kim, S.-G.; Bae, S.-H.; Lee, D.-K.; Lin, O.; Yang, Y.; Park, N.-G., The interplay between trap density and hysteresis in planar heterojunction perovskite solar cells. *Nano Lett.* **2017,** *17* (7), 4270-4276.

6. General conclusions and future prospects

In this thesis, we focused on the perovskite light absorption materials modification and the interface passivation for achieving highly efficient and stable perovskite solar cells. We added the high-conductivity MXene ($Ti_3T_2T_x$) into the perovskite film for improving the device performance. We proposed a mechanism of controlling the perovskite crystal growth by $Ti_3T_2T_x$. We developed a simple interface passivation method with $SnCl_2$ solution for reducing the energy loss at the interface. The suppressed recombination process at the interface lead obviously improved V_{oc} of the $CsPbIBr_2$ solar cells. The Nb^{5+} ion was introduced into the all-inorganic perovskite film for stabilizing the photoactive black phase. The Nb ions slight substituted the Pb ions in the perovskite and improved the tolerance factor of the materials. The black phase of $CsPbI_2Br$ was effectively stabilized and the performance was improved.

1. We have demonstrated a strategy of introducing a 2D layered $Ti_3C_2T_x$ MXene into the perovskite film to improve the film quality. The additive is able to retard the nucleation process of the perovskite crystals, resulting in larger grain size. In addition, the high conductivity of $Ti_3C_2T_x$ is highly beneficial to accelerate the electron transfer through the grain boundary. After optimizing the solvents and the adding amount, we found 0.03 wt % is the most proper amount and the DMF is the most suitable solvent for MXene additive. Accordingly, the champion PCE is improved from 15.54% to 17.41% and the average PCE is increased from 15.18% to 16.80%.

2. We have developed an efficient interface engineering using $SnCl_2$ for SnO_2 film passivation. This passivation method is able to suppress the recombination process at the interface between the $CsPbIBr_2$ perovskite layer and the SnO_2 and accelerates the electron extraction efficiency from the perovskite film. After passivation with 0.1 M $SnCl_2$, a high V_{oc} of 1.31 V with minimum energy loss of 0.74 eV was achieved. The thermal stability of the passivated SnO_2 based devices is also higher than that of the bare SnO_2 based solar cells.

3. The Nb ions were introduced into the perovskite film for stabilizing the photoactive phase of $CsPbI_2Br$. Results indicate that the Nb^{5+} can substitute the Pb^{2+}, which increases the perovskite tolerance factor and significantly stabilizes the α-$CsPbI_2Br$ phase. With 0.5% Nb^{5+} incorporation, a champion PCE of 10.42% was achieved for a carbon-based PSCs. The Nb^{5+} doping can also

reduce the charge recombination in the perovskite film, resulting in a champion V_{oc} of 1.27 V and negligible hysteresis-free device.

The performance of the perovskite solar cells is determined by the quality of perovskite film and the interface of the device. We believe that the performance can be further enhanced by controlling the perovskite film growth for obtaining large crystals because the charge recombination at the grain boundaries is one of the main reasons for the unsatisfied device performance. Therefore, the additive should retard the crystal nuclei process for generating large crystals, through which the amount of grain boundaries can be reduced. Moreover, the additive should have high conductivity because the additive must be beneficial to accelerate the charge transfer through the grain boundaries.

Optimizing the interface for perfect contact between the components is also promising for enhancing the performance of the device. This because the charge recombination at the interface is another important reason for unsatisfied performance, especially large energy loss (low V_{oc}). When the interface is passivated with a thin layer, the charge extraction will be accelerated and the recombination will be suppressed due to reduced trap state and defects. As for the passivation materials, the organic molecules might be suitable because they are soluble in solvents and easy to interact with the under layer and the up layer. Moreover, the conductivity and the mobility might also be helpful to accelerate the charge transfer through the interface.

The stability for the photoactive α phase of all-inorganic perovskites is a fundamental issue for these materials. It is essential to search for simple and effective methods for stabilizing the α phase in ambient conditions. The first one is to constructing a protection layer for the perovskite film to prevent the humidity. The protection layer must be hydrophobic, which is common in organic molecules. Moreover, the materials of the protection layer should interact with the perovskite layer because not perfect contact will decrease the performances of the device. Another method is to doping the perovskite materials with smaller metal ions. This because replacing the Pb with smaller ions will effectively increase the tolerance factor of the materials, which will lead to higher crystal structure stability.

The commercialization of perovskite solar cells is being widely studied. We believe after solving the above issues including performance and the stability, the commercialization of this photovoltaic technology will be very promising. Moreover, it is a good choice to use perovskite

solar cells as a part of tandem solar cells with silicon or organic solar cells in practical applications. In a word, this photovoltaic technology has the potential to change the world energy market and the daily life of human beings.

Achievements

Publications

1. Zhanglin Guo, Liguo Gao, Chu Zhang, Zhenhua Xu, Tingli Ma*, Low-temperature processed non-TiO_2 electron selective layers for perovskite solar cells, *Journal of Materials Chemistry A*, 2018, 6(11), 4572-4589.

2. Zhanglin Guo, Liguo Gao, Zhenhua Xu, Siowhwa Teo, Chu Zhang, Yusuke Kamata, Shuzi Hayase, Tingli Ma*, High Electrical Conductivity 2D MXene Serves as Additive of Perovskite for Efficient Solar Cells, *Small*, 2018, 14(47): 1802738.

3. Zhanglin Guo, Siowhwa Teo, Zhenhua Xu, Chu Zhang, Yusuke Kamata, Shuzi Hayase and Tingli Ma*, Achievable high V_{oc} of carbon based all-inorganic $CsPbIBr_2$ perovskite solar cells through interface engineering, *Journal of Materials Chemistry A*, 2019, 7, 1227-1232.

4. Zhanglin Guo, Shuai Zhao, Anmin Liu, Yusuke Kamata, Siowhwa Teo, Shuzhang Yang, Zhenhua Xu, Shuzi Hayase, Tingli Ma*, Niobium doped $CsPbI_2Br$ for efficient and stable all-inorganic perovskite solar cells, *ACS Applied Materials & Interfaces*, 2019, 11(22), 19994-20003.

5. Shuzhang Yang#, **Zhanglin Guo#(co-first author),** Liguo Gao, Fengyang Yu, Chu Zhang, Meiqiang Fan, Guoying Wei, Tingli Ma*, Bifunctional Dye Molecule in All-inorganic $CsPbIBr_2$ Perovskite Solar Cells with Efficiency Exceeding 10%, *Solar RRL,* doi.org/10.1002/solr.201900212.

6. Siowhwa Teo, **Zhanglin Guo**, Zhenhua Xu, Chu Zhang, Yusuke Kamata, Shuzi Hayase, Tingli Ma*, The Role of Lanthanum in a Nickel Oxide‐Based Inverted Perovskite Solar Cell for Efficiency and Stability Improvement, *ChemSusChem*, 2019, 12(2): 518-526.

7. Nannan Wang, Yanqiang Li, **Zhanglin Guo**, Huan Li, Shuzi Hayase, Tingli Ma*, Minute quantities of hexagonal nanoplates PtFe alloy with facile operating conditions enhanced electrocatalytic activity and durability for oxygen reduction reaction, *Journal of Alloys and Compounds*, 2018, 752: 23-31.

8. Nannan Wang, Yanqiang Li, **Zhanglin Guo**, Huan Li, Shuzi Hayase, Tingli Ma*, Synthesis of Fe, Co Incorporated in P-Doped Porous Carbon Using a Metal-Organic Framework (MOF)

Precursor as Stable Catalysts for Oxygen Reduction Reaction, *Journal of The Electrochemical Society*, 2018, 165(12): G3080-G3086.

9. Chu Zhang, Siowhwa Teo, **Zhanglin Guo**, Liguo Gao, Yusuke Kamata, Zhenhua Xu, Tingli Ma*, Development of a Mixed Halide-chalcogenide Bismuth-based Perovskite $MABiI_2S$ with Small Bandgap and Wide Absorption Range, *Chemistry Letters*, 2018, 48.

10. Chu Zhang, Liguo Gao, Siowhwa Teo, **Zhanglin Guo**, Zhenhua Xu, Shuai Zhao, Tingli Ma*, Design of a novel and highly stable lead-free Cs_2NaBiI_6 double perovskite for photovoltaic application, *Sustainable Energy & Fuels*, 2018, 2(11): 2419-2428.

11. Huan Li, Anmin Liu, Shuai Zhao, **Zhanglin Guo**, Nannan Wang, Tingli Ma*, In Situ Growth of a Feather-like MnO_2 Nanostructure on Carbon Paper for High-Performance Rechargeable Sodium-Ion Batteries, *ChemElectroChem*, 2018, 5(21): 3266-3272.

Conferences

1. Zhanglin Guo, Chu Zhang, Tingli Ma*, "Electron Selective Layer with High Conductivity for Perovskite Solar Cells", The Japan-China Workshop on materials and their Application in New Energy Devices, 4-8th, Oct. 2017, Kitakyushu, Japan.

2. Zhanglin Guo, Chu Zhang, Liguo Gao, Tingli Ma*, "Design and fabrication of two-dimensional materials based perovskite solar cells", International Conference Asia-Pacific Hybrid and Organic Photovoltaics (AP-HOPV18), 28-30th, Jan. 2018, Kitakyushu, Japan.

3. Zhanglin Guo, Zhenhua Xu, Siowhwa Teo, Chu Zhang, Tingli Ma*, "Surface passivation: an efficient method to reduce the energy loss of all-inorganic $CsPbIBr_2$ perovskite solar cells", International Conference on Perovskite and Organic Photovoltaics and Optoelectronics (IPEROP-19), 27-29th, Jan. 2019, Kyoto, Japan.

4. Chu Zhang, **Zhanglin Guo**, Shuai Zhao, Liguo Gao, Tingli Ma. "Design and Synthesis of a New All Inorganic Double Perovskite Cs_2NaBiI_6 with 3D Shuttle-like Structure", Japan-China Workshop on "Nanomaterials and their applications in new energy devices", 4-8th, Oct. 2017, Kitakyushu, Japan.

5. Chu Zhang, **Zhanglin Guo**, Shuai Zhao, Liguo Gao, Tingli Ma. "Design and Synthesis of a New All Inorganic Double Perovskite Cs_2NaBiI_6 with 3D Shuttle-like Structure", International

Conference Asia-Pacific Hybrid and Organic Photovoltaics (AP-HOPV18), 28-30th, Jan. 2018, Kitakyushu, Japan.

6. Huan Li, Chu Zhang, **Zhanglin Guo**, Tingli Ma, "In-situ growth of feather-like MnO_2 on carbon paper for high performance sodium-ion battery", 5th International Conference on Nanomechanics and Nanocomposites (ICNN5), 22nd-25th, Aug. 2018, Fukuoka, Japan.

7. Chu Zhang, Siowhwa Teo, **Zhanglin Guo**, Zhenhua Xu, Tingli Ma. "Designation of a Novel and Highly Stable Lead-Free Cs_2NaBiI_6 Double Perovskite for Photovoltaic Application", 35th European Photovoltaic Solar Energy (EU PVSEC), 24th-28th, Sep. 2018, Brussels, Belgium.

8. Tingli Ma, Liguo Gao, **Zhanglin Guo**, "Current Progress in Low-Temperature Processed Non-TiO_2 Electron Selective Layers for Perovskite Solar Cells", 2018 MRS SPRING MEETING & EXHIBIT, 2nd-6th, April, 2018, Phoenix, USA.

Acknowledgements

Firstly, I would like to express my deepest thanks to my supervisor, Prof. Tingli Ma. During my doctoral course study, Prof. Ma has always been able to lead me to the correct direction in my research, and she always gives me encourage when I am down in spirits. It is her instruction and help that makes me finish my doctoral program smoothly.

I would greatly thank Prof. Shuzi Hayase for offering me help and the access to characterization equipment, which are essential for finishing this thesis. I would also thank Dr. Shyam S. Pandey, who helped me a lot in the past three years. Meanwhile, I would like to thank all the members in Ma lab, Hayase-Pandey lab, for they have provided valuable and assistant in the research and my daily life.

I would express my thanks and love to my parents, who have supported my study and life in Japan without double. I would like to give thanks to my dear wife for the past 10 years' accompany, encouragement and guidance. I could not imagine the life without her and I could not finish my doctoral study without her help.